Online monitoring of laser-based powder bed fusion by acoustic emission

-Dean-Paul Riethmüller Kouprianoff-

Thesis submitted in fulfilment of the requirements for the degree

DOCTOR OF ENGINEERING IN MECHANICAL ENGINEERING

in the Department of Mechanical and Mechatronics Engineering

Faculty of Engineering, Built Environment and Information Technology

at Central University of Technology, Free State

Promoter: Prof. Ihar Yadroitsau, D. Eng.

Co-promoters: Dr. Ina Yadroitsava, Ph.D.

Dr. Nicolaas Luwes, D. Eng.

September 2021

"Look deep into nature, and then you will understand everything better."

Albert Einstein

"Truth is so obscure in these times, and falsehood so established, that, unless we love the truth, we cannot know it."

Blaise Pascal

DECLARATION WITH REGARD TO INDEPENDENT WORK

I, *Dean-Paul Riethmüller Kouprianoff*, identity number and student number , do hereby declare that this research project submitted to Central University of Technology, Free State (CUT, FS) for the degree, Doctor of Engineering in Mechanical Engineering, is my own independent work; and complies with the code of academic integrity, as well as other relevant policies, procedures, rules and regulations of Central University of Technology, Free State; and has not been submitted previously to any institution by myself or any other person in fulfilment of the requirements for the attainment of any qualification.

Signature of student 

Date: 7 September 2021

ACKNOWLEDGEMENTS

I have learnt so much about the scientific environment from this study and have come to realize that it is truly a privilege to measure scientific phenomena. My whole life I have wanted to contribute in some manner and it always felt impossible. A great turning point has come in realizing that we need only look at Nature. I am sure that for some this thought might be trivial or insignificant, but it never occurred to me or I have not listened. Nature, as God has created it, is very inspiring and it stirs my soul. God said "*let there be light*" and in His great wisdom He first created radiation. Radiation in its various forms sets everything into motion, providing the foundation of life. The flickering light of the stars was to be a compass for the early sea explorers and light feeding the flower gently turns its stem. Radiation accomplishes these mighty things and for the past 60 years we have used it to produce tremendous technological advancements, one of which is Laser Powder Bed Fusion. And yet, radiation makes simple things possible such as reading this document. And so, God calls all to enjoy His radiant light:

> *"This is the message we have heard from him and declare to you: God is light; in him there is no darkness at all. If we claim to have fellowship with him and yet walk in the darkness, we lie and do not live out the truth. But if we walk in the light, as he is in the light, we have fellowship with one another, and the blood of Jesus, his Son, purifies us from all sin. If we claim to be without sin, we deceive ourselves and the truth is not in us. If we confess our sins, he is faithful and just and will forgive us our sins and purify us from all unrighteousness."- 1 John 1:5-9*

I would like to acknowledge my wife Zanél. She has been such a blessing to me, and in turn, to this study. I wish I could go on to write about her beauty, strength, merry presence, dignity, charm, loving care…but our love, although glowing, is not for all to see. If it be God's will, I will confine my thoughts to our personal relationship until my lamp light burns no more.

I would like to thank my supervisors, Prof. Ihar Yadroitsau (Igor Yadroitsev), and Dr. Ina Yadroitsava, for their guidance and concern that goes far beyond what is required and extends to a personal relationship from which I have gained much. I would also like to thank Dr. Nicolaas Luwes, my co-supervisor, from the Department of Electrical, Electronic and Computer Engineering at CUT, for his contribution and especially for introducing digital signal processing to me.

A special thanks to the following funding sources without which this research would not have been possible: The South African Research Chairs Initiative of the Department of Science and Innovation and National Research Foundation of South Africa (Grant №97994) and the Collaborative Program in Additive Manufacturing (Contract № CSIR-NLC-CPAM-15-MOA-CUT-01).

ABSTRACT

Metal additive manufacturing (AM) has seen great advances in capabilities and the technology has matured to the point where industries, such as aerospace, are readily implementing it for production. The main concern remains qualification and quality control. Laser powder bed fusion (LPBF) is one of the more popular AM technologies which, as the name suggests, uses a laser to melt and solidify a powder in such a way as to create a three-dimensional part. The part is built in a layer-wise fashion, stacking each layer on top of the previous layer.

The quality of the part being built is dependent on the quality of the previous layer as it forms the foundation. The advantage of the layer-wise process is that it also makes online monitoring of the building process a viable option. Monitoring the process can allow for very tight control and thus improve the quality or notify the operator that the component has defects and, therefore, is not fit for service.

Current commercial online monitoring systems are mostly in the form of some sort of imaging or temperature monitoring system. These have the ability to monitor any defects in the powder delivery and laser scanning (melt pool). The size and shape of single tracks ultimately determine the quality of the parts, as it is the building block of the LPBF process. All the different process parameters interplay with each other and operate within a process window. The powder layer should be carefully controlled because the input energy from the laser is set and any change in material volume/powder thickness will change the resulting track's shape.

This study investigates whether gas-borne acoustic emission (AE) signal can be used for online monitoring during LPBF. The amazing amount of information that can be interpreted through listening has been proved for manufacturing processes such as laser welding and monitoring of components in service, such as electrical generators.

The experiments were carried out on a commercial machine, EOS M 280, with Ti6Al4V ELI alloy. The influence of the machine noise, microphone and scanning position is investigated, and the signal filtered accordingly. Defects due to changes in process parameters are shown, and more specifically, laser power, scanning speed and powder layer thickness. The AE is correlated to the resulting single track shape. Each combination of sets of process parameters produces a specific sound. The sound pressure level and frequency of AE signal are clearly correlated to defects in single tracks that are supported by physical cross-sectioning.

The information about the characteristics of LPBF and its AE is used to develop two possible methods which can detect a defective layer thickness. The algorithm compares the test signal

to signals from optimal parameters and parameters which produce defects. The signals are run through a series of processing steps and the results are then correlated to each other. It is shown that the proposed algorithm can detect a defective layer with high accuracy.

Table of Contents

LIST OF FIGURES

LIST OF TABLES

GLOSSARY

AE	Acoustic emission
AM	Additive manufacturing
CAD	Computer aided design
CT	Computed tomography
DFT	Discrete Fourier transform
DMLS	Direct metal laser sintering
EBM	Electron beam melting
EDM	Electric discharge machining
ELI	Extra-low interstitial
ET	Eddy current testing
FFT	Fast Fourier transform
HIP	Hot isostatic pressing
HT	Heat treatment
LENS	Laser-engineered net shaping
LPBF	Laser powder bed fusion
NDT	Non-destructive testing
RT	Radiographic testing
SLM	Selective laser melting
SNR	Signal-to-noise ratio
SPL	Sound Pressure Level
STFT	Short Time Fourier Transform
STL	Standard triangle language
UT	Ultrasonic testing
VT	Visual testing
XRD	X-ray diffractometer

Chapter 1: INTRODUCTION

1.1 Background

Additive Manufacturing (AM) is defined by ASTM as “a process of joining materials to make objects from 3D model data, usually layer upon layer, as opposed to subtractive manufacturing methodologies” (ASTM F2792-12a). AM creates 3D objects from a 3D model designed by CAD software. The software creates virtual cuts to the model (cross-sections), generating a sequence of layers. These layers represent the material that would be added by stacking them on to each other, layer by layer, which in turn forms the model. The machine superimposes the layers onto each other until the entire part has been formed.

AM has grown considerably during the last four decades. AM is used for prototyping, modelling, tooling and production of end-use components. Customized medical implants, functional parts with great complexity and tooling inserts with conformal cooling are good examples of the range of applications (Design for Additive Manufacturing, 2020; DebRoy et al., 2018; du Plessis et al., 2019; Kruth et al., 2010). AM allows engineers and designers more design freedom compared to that of conventional manufacturing methods: unique products can be manufactured at low volumes in an economical way (DebRoy et al., 2019). A significant uses the industry started to implement this technology. In 2018, GE Aviation announced mass production of 3D printed engine parts (Lopez et al., 2021). Other real AM application is in automotive industry: Betatype produces LED headlight component; Bugatti manufactures one of the largest topology optimized titanium parts – brake calliper by LPBF. Mass production of medical devices and implants by LPBF also is being introduced: for example, Bego (USA) manufactures LPBF dental implants; DePuy Synthes Spine (USA) is printing cellular bone-mimicking implants (Lopez et al., 2021). The doughnut chart in Figure 1 shows how AM is applied in the different industries. The annual Wohlers Report showed that for 2012 the largest use in the AM market was for consumer products/electronics, occupying 21.8%. In 2014, industrial/business machines took first place, adding up to 17.5%. Although in 2019 it seems that the markets have not changed too much since 2012, it should be kept in mind that the AM market has grown considerably. For the last five years metal AM has seen more than 40% growth for each year. As a practical example, automotive companies not only continue to use AM for design and prototyping but also are increasing production parts via AM. One example is the new BMW i8 roadster that has a 3D-printed window rail guide. To date, BMW has incorporated more than one million AM parts in production vehicles (Wohlers, 2019).

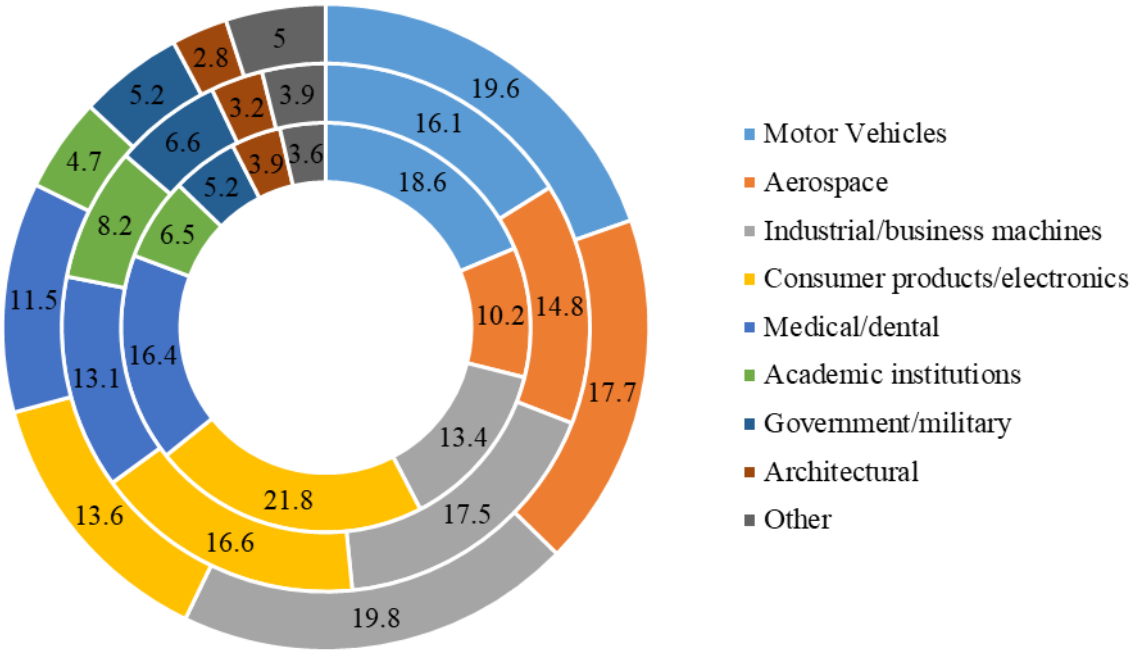

Figure 1: Application market for AM: in 2012 (inner), 2014 (middle) and 2019 (outer) (data from Wohlers, 2014, 2015 and 2019)

A number of metal powder systems are available with different heat sources, i.e. laser (LPBF) or electron beam (E-PBF), which makes it is hard to keep track of the differences in technologies in the growing metal AM industry. Most important aspects to consider when selecting a metal AM machine are: range of materials, speed, size of the component needed, part quality and its cost (Nickels, 2016; Bikas *et al.*, 2016). LPBF is a multi-disciplinary technology based on metallurgy, optics, laser physics, electronics, fluid flow, mechanics of solids and heat transfer, etc. (Fogannolo *et al.*, 2012). Basic LPBF machine components are shown in Figure 3.

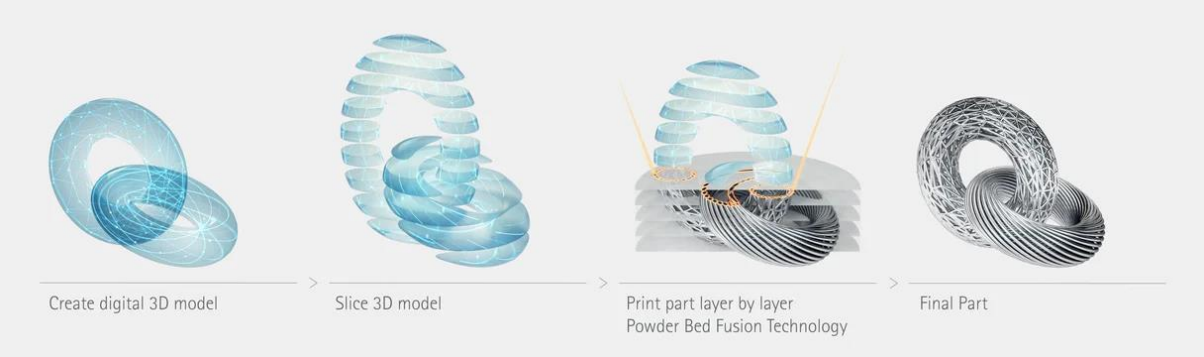

Figure 2: LPBF principle (EOS GMBH, 2020)

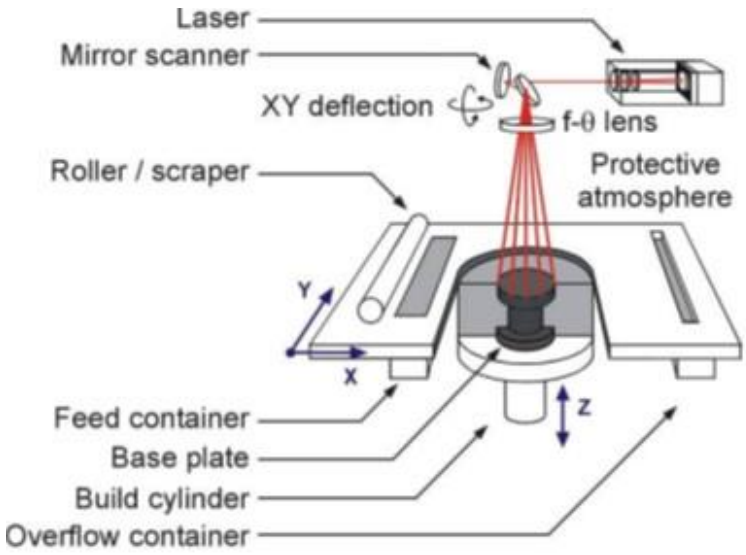

Figure 3: Components of a basic LPBF machine (Kruth et al., 2010)

LPBF process involves many variables, all of which can result in reduced part quality and these changes cannot always be easily detected. This is further complicated by the fast- growing field with different types of systems and the general lack of standards (Seifi *et al.*, 2017, 2016). For products used in safety critical applications such as aerospace, part quality and the documentation thereof are important (Krauss *et al.*, 2014). A paper trail can be generated in different ways such as producing accompanying tensile samples or non-destructive testing using computer tomography (CT). Quality control remains a huge hurdle for AM to be used on a broader scale. For example, in aerospace there are various factors that make implementation difficult; not only does the company need AM technical know-how and skills, but the customer must accept the use of such technology. The regulating bodies need to set standards to regulate control of quality which in turn will lead to acceptance in industry (Dordlofva *et al.*, 2019). LPBF is very sensitive to process parameters of different machine manufacturers and these technologies produce products with different material properties (Agius *et al.*, 2018). Therefore, quality control is all the more important. The AM community started their own standards subcommittee in 2009 with the establishment of the ATSM F42. Thereafter, in 2011, a cooperation agreement was established between the International Organization for Standardization (ISO), ISO/TC 261, and ASTM F42 to develop joint standards such as ISO/ASTM52900-15: Standard Terminology for Additive Manufacturing (ISO, 2020; ASTM, 2020). In order to reliably reproduce these excellent properties, online monitoring is required. There is a high demand for this in AM generally and especially in LPBF as evidenced by a

series of reviews on the topic in recent years (Everton *et al.*, 2016; Grasso and Colosimo, 2017; Lu and Wong, 2018; Spears and Gold, 2016; Tapia and Elwany, 2014).

To develop a system that can evaluate the quality of the part online requires a thorough understanding of the physics involved. It is important to understand what defects are present and how they formed. It is also essential to have a thorough understanding of the process and the nature a characteristics of the part being examined with the aid of non-destructive testing (NDT). To be able to select and implement a suitable testing technique, the entire process chain needs to be considered along with possible defects that might occur. Knowledge of how defects are generated within a component will give the operator sufficient know-how as to the orientation, size, and other defect characteristics that will be crucial for defect detection (Hellier, 2012).

Key process parameters in LPBF are laser and scanning parameters, powder material properties, powder bed properties, recoating parameters and build environment parameters (see Appendix). Slight variations in the process could lead to porosity. Residual stress causes deformations which could disturb the process. Process signatures emanating from the melt pools in LPBF are: molten/solidified pool, plasma emission/absorption, radiation, reflected/scattered light, etc. These phenomena are the basis to control stability and repeatability of the LPBF process. In-process sensing and control is one of the main steps for ensuring repeatability and consistency of LPBF manufacturing. Commercial online monitoring systems are available from leading LPBF machine manufacturers such as EOS, SLM, and 3D Systems, offering EOSTATE, ADDITIVE.QUALITY and DMP Inspection, respectively. These systems use some form of photodiode for melt pool monitoring, the CMOS camera for powder bed imaging system, IR and UV photosensors and pyrometers for build atmosphere monitoring (EOS, 2020; SLM, 2020; 3D Systems, 2020). These types of monitoring equipment are expensive, some of which produce vast amounts of data. AE is a type of monitoring method that measures the waves that arise from various energy sources, these sources induce vibration or pressure waves which are monitored by a sensor and correlated to specific events. Although AE has successfully been used for online monitoring during industrial applications such as laser welding, the use of AE in LPBF is lacking. Gas-borne AE, in contrast to the above-mentioned commercial LPBF systems is relatively easy to implement, inexpensive, has high temporal resolution and able to give information with a small amount of data compared to imaging systems.

1.2 Problem statement, aim and objectives

In laser processes, such as laser fusion, welding, ablation, cutting and surface treatment, various phenomena are observed: vaporization, melting and solidification, interaction of materials with protective atmosphere, shrinkage and solid-state phase transformations, plastic deformations and cracking. These phenomena are related to unique acoustic signals. It was shown that the acoustic energy and spectrum for laser-material interactions show a strong correlation with laser power, speed and laser spot size (Bordatchev and Nikumb, 2006; Kacaras *et al.*, 2019; Wu *et al.*, 2020; Yusof *et al.*, 2017). Different AE patterns were found to distinguish the behaviour of optimal and faulty laser welding (Wasmer *et al.*, 2019).

This work sets out to detect whether gas-borne AE could be used to identify failure in the LPBF process, for example, in the processing of Ti6Al4V alloy. Most research is focused on qualifying Ti6Al4V, not only because it is widely established using conventional manufacturing methods and much-needed for the medical and aerospace industry, but also because there is an extensive database available.

Single track formation is used to optimize process parameters for a particular powder material and LPBF system. A stable single track is a primary necessity to produce a fully dense 3D part: smooth and even tracks alongside one another result in smooth and even layers, followed by the next layer above this with sufficient penetration into the previous layer. When forming uneven tracks, for example, in the case of the humping or balling, the tracks are irregular, which causes the adjacent tracks and successive layers to not melt sufficiently and, as a result, the formation of lack-of-fusion porosity. The correlation between the shape and size of melt pool/single tracks and porosity in 3D parts was proven in many investigations (Yadroitsev, 2009; Kuo *et al.*, 2020; Tran and Lo, 2019). The occurrence of defects during the LPBF process was described in detail in Kyogoku and Ikeshoji, 2020 and Oliveira *et al.*, 2020.

Correlating AE signals with process instability, which lead to defects during LPBF, is studied. The combination of AE with visual inspection of artificial defects in single tracks and layers can potentially be very useful to create algorithms for online monitoring. It is shown that AE is a valuable tool in online monitoring systems. The aim of the study is to show that gas-borne AE online monitoring can identify a difference between varying modes of LPBF during processing.

The objectives are:

- To find correlation between characteristics of single track and gas-borne AE at different process parameters.
- To find AE signature for a stable LPBF process at optimal parameters for Ti6Al4V ELI powder.
- To develop an AE signal-processing algorithm to identify delivery defects in the powder layer.

1.3 The scope of the project

The South African Additive Manufacturing Strategy has identified qualifying AM parts from Ti alloys for medical and aerospace as one of the focus areas (de Beer *et al.*, 2016). At the Centre for Rapid Prototyping and Manufacturing (CRPM), which received international certification (ISO 13485) to manufacture Ti6Al4V medical devices using AM (CRPM, 2020), the current focus is on manufacturing high-quality implants with proper tracking of the process, from powder control to final component shipment. In the present work, the focus of the study is to create an online monitoring algorithm for LPBF using gas-borne AE. The algorithm should be able to detect undesirable modes such as balling and keyhole.

1.4 Research methodology

The thesis was divided in phases (Figure 4):

- State of the art in the research fields: metal LBPF, peculiarities of LBPF process, current quality control methods, AE, gas-borne AE, signal processing.
- Manufacturing Ti6Al4V LPBF components with and without artificial defects. Data collection and analysis.
- Recording AE signals during LPBF for Ti6Al4V at different process parameters. Analyzing modes of the LPBF process and the corresponding defects in single tracks and layers.
- Implementing signal processing: develop a way of extracting data using signal processing from the recorded signal which would be attributed to certain defect-causing phenomena.

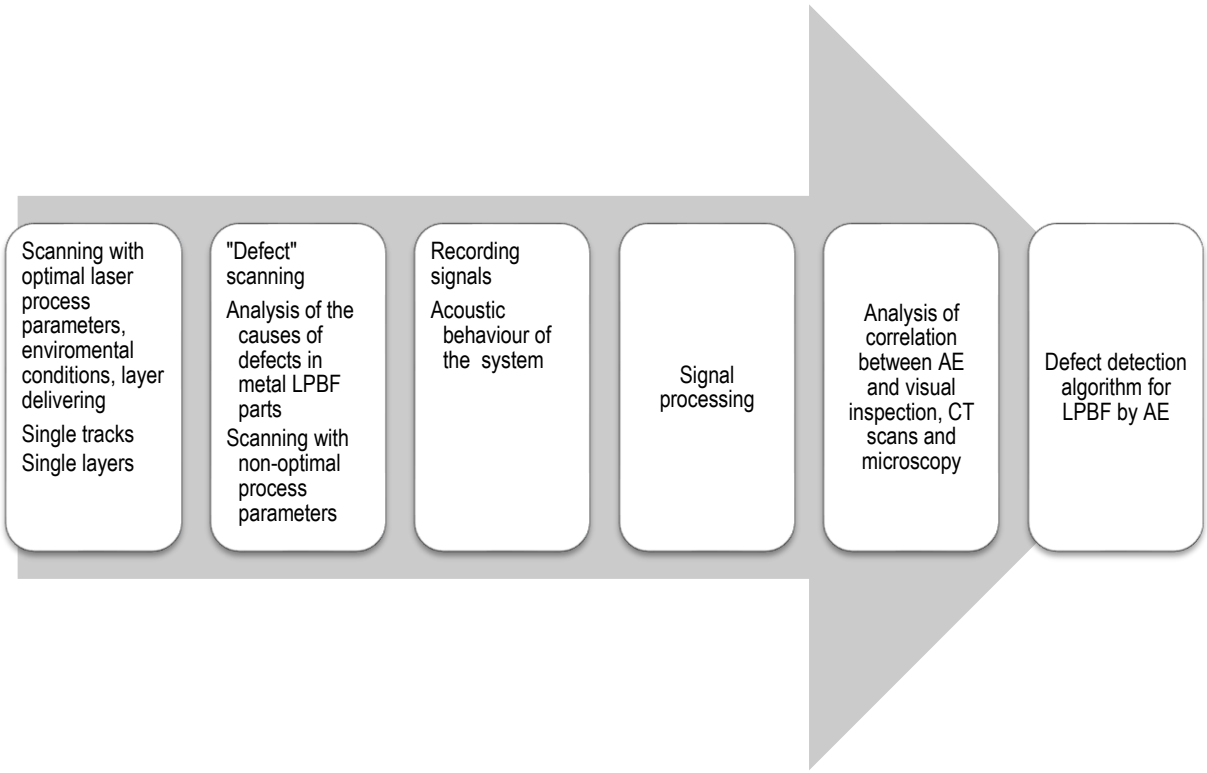

Figure 4: Flowchart of the project

1.5 An overview of the thesis

The following outline defines the structure of the thesis:

- Chapter 1 – Introduction: An introduction and background to the study. In this chapter the aim, the statement and the methodology of the study are described.
- Chapter 2 – Literature review: AM technology principles and state-of-the-art manufacturing methods are investigated. An in-depth study of the LPBF process and the nature of defect formation are presented. Online monitoring and component testing methods and the principle of operation are discussed. AE principles relevant to this study are described.
- Chapter 3 – Materials and methods: Equipment selected for the research and the scientific approach to produce LPBF parts are presented. The AE method and equipment are described.
- Chapter 4 – Results and discussion: Development of defects due to process parameters, such as lack of fusion porosity, is demonstrated. Correlation between shape of single tracks and AE is shown.
- Chapter 5 – Conclusion: Conclusions drawn from the study are defined.

1.6 Expected contribution

The detrimental effect of porosity on the mechanical properties of Ti6Al4V (ELI) alloy limits the effectiveness in the application and qualification of LPBF implants. This study validates an algorithm based on detailed analysis of AE signals for LPBF of single tracks and layers to develop an online monitoring tool using airborne AE for defect identification in the production process.

1.7 Publications and presentations to date

Gas-borne AE monitoring

1. D. Kouprianoff, A. du Plessis, I. Yadroitsava, I. Yadroitsev. Non-destructive testing of the parts manufactured by Direct Metal Laser Sintering. In Proc. RAPDASA 17th International Conference. "Building on the foundations – Consolidating impact into products to enhance quality of life for all South Africans", Vaal University of Technology, November 2–4, 2016.
2. D. Kouprianoff, A. du Plessis, I. Yadroitsava, I. Yadroitsev. Destructive and non-destructive testing on small and intricate DMLS components. In Proc. RAPDASA 18th International Conference, Durban, Inkosi Albert Luthuli International Convention Centre, November 8–10, 2017.
3. D. Kouprianoff, N. Luwes, I. Yadroitsava, I. Yadroitsev, E. Newby. On-line monitoring of laser powder bed fusion by acoustic emission. In Proc. PRASA-RobMech International Conference incorporating the 28th Annual Symposium of the Pattern Recognition Association of South Africa and the 10th Robotics and Mechatronics Conference of South Africa, Bloemfontein, Central University of Technology, 29 November–1 December, 2017.
4. D. Kouprianoff, N. Luwes, I. Yadroitsava, I. Yadroitsev. Validation of microphone placement for acoustic emission for online detection of porosity forming phenomena during metal laser powder bed fusion. In Proc. RAPDASA 19th International Conference, Johannesburg, Protea Parktonian, November 7–9, 2018.
5. D. Kouprianoff, N. Luwes, I. Yadroitsava, I. Yadroitsev. Acoustic emission technique for online detection of fusion defects for single tracks during metal laser powder bed fusion. SSF 2018 – The 29th Annual International Solid Freeform Fabrication Symposium – An Additive Manufacturing Conference, Austin, Texas, August 13–15, 2018, p. 2087–2096.

6. D. Kouprianoff, I. Yadroitsava, I. Yadroitsev. Gas-borne acoustic emission response for LPBF of optimal laser parameters for Ti6Al4V during non-optimal layer thicknesses. In Proc. RAPDASA 20th International Conference "Creating the Future of Manufacturing – Layer by Layer", Central University of Technology, November 6–8, 2019.
7. I. Yadroitsev, D. Kouprianoff, N. Luwes, I. Yadroitsava. Analysis of acoustic emission signal for on-line monitoring during laser powder bed fusion. The First International Conference on Research Advances in Additive Manufacturing (RAAM), March 3–5, 2019, Nanjing, China (*presentation*).
8. D. Kouprianoff, I. Yadroitsava, A. du Plessis, N. Luwes, I. Yadroitsev. Monitoring of laser powder bed fusion by acoustic emission: investigation of single tracks and layers, 2021. Frontiers in Mechanical Engineering, https://doi.org/10.3389/fmech.2021.678076
9. D. Kouprianoff. Evolution of acoustic emission signal during L-PBF at different operating modes. Submitted to 21st International Conference "Additive Manufacturing for our rapidly changing world", Central University of Technology, November 4–6, 2020.

LPBF process

1. A.M. Vilardell, I. Yadroitsev, I. Yadroitsava, M. Albu, N. Takata, M. Kobashi, P. Krakhmalev, D. Kouprianoff, G. Kothleitner, A. du Plessis. Manufacturing and characterization of in-situ alloyed Ti6Al4V (ELI) - 3 at .% Cu by laser powder bed fusion, 2020. Additive Manufacturing, https://doi.org/10.1016/j.addma.2020.101436
2. A. du Plessis, D. Kouprianoff, I. Yadroitsava, I. Yadroitsev. Mechanical properties and in-situ deformation imaging of microlattices manufactured by laser based powder bed fusion. Materials 2018, 11, 1663.
3. I. Yadroitsava, I. Yadroitsev, I. van Zyl, D. Kouprianoff, W.B. du Preez. Laser-based powder bed fusion of pure platinum. COMA '19, 7th International Conference on Competitive Manufacturing, 30 January–1 February 2019, Stellenbosch, South Africa, pp. 188–193. ISBN 978-0-7972-1779-9.
4. A. du Plessis, I. Yadroitsava, D. Kouprianoff, I. Yadroitsev. Numerical and experimental study of the effect of artificial porosity in a lattice structure, SSF 2018–

The 29th Annual International Solid Freeform Fabrication Symposium – An Additive Manufacturing Conference, Austin, Texas, August 12–14, 2018, pp. 808–820.

5. E.B. Newby, D. Kouprianoff, I. Yadroitsava. In-situ Alloying of Ti6Al4V-x%Cu Structures by Direct Metal Laser Sintering, 18th RAPDASA Annual International Conference, International Convention Centre, Durban, 8–10 November 2017, RAPDASA 2017 Conference Proceedings, pp. 180–188.
6. I. Yadroitsev, I. Yadroitsava, P. Krakhmalev, A. Du Plessis, E. Newby, D. Kouprianoff. Optimisation of process parameters for in-situ alloyed titanium by selective laser melting. Holistic innovation in additive manufacturing, June 26–27, 2019, Vancouver, BC, Canada (*presentation*).

Chapter 2: LITERATURE REVIEW

2.1 Laser powder bed fusion process

2.1.1 Single track formation

The interaction of the laser and powder can be split into three stages: preheating, melting with shrinkage and re-solidification. This interaction is dependent on numerous physical variables such as laser power density, wavelength, interaction time, the thermodynamic and chemical properties of the material, etc. Such interactions can typically be used for online monitoring as the amount of energy absorbed etc. would change the process and thus give information that can be used to control or evaluate the process quality.

A powder bed has a relatively high laser absorptivity: the powder surface creates conditions for high laser absorption because multiple reflections within the powder layer causing higher absorption than a bare substrate. The particle size and morphology determines the scatter regimes and the sensitivity to incident energy. The laser absorption of powder layer does not only depend on the amount of energy absorbed through the physiochemical properties, but also on the powder shape and apparent density. Because of the above-mentioned, the absorption can differ greatly from bulk to powder materials, e.g., $A_{Fe\ bulk} = 0.36$ and $A_{Fe\ powder} = 0.7$ at 1.06 μm wavelength (Yadroitsev *et al.*, 2010; Yadroitsev, 2009).

Due to surface tension, the molten material forms a cylinder-like track (Figure 5). Penetration into the substrate or previous layer has an additional stabilizing effect for continuous track formation. Each alloy has its own set of process parameters that yields stable or unstable tracks.

The shape of the single track is to a great extent dependent on the amount of material involved (Figure 5). Laser power density gives an indication of how much power is put in per unit area and determines the geometry of the track, while the height of the track is determined largely by the powder layer thickness. If the layer thickness is too high, optimal adhesion to the substrate or previous layers will not occur because of inadequate melting depth. A semi-spherical shape in the cross-section of a track forms in conduction mode; the aspect ratio of depth to width of the melt pool does not exceed 1:2. At high power density, deep penetration occurs due to vapour recoil pressure which pushes back on the melt pool and forms a depression in the surface of the melt pool (keyhole mode). During keyhole mode, laser reflection within the cavity increases energy absorption. In the transition mode, a higher penetration in comparison with a conduction mode appears and the shape of melt pool changes (Figure 5b).

The powder adjacent to the laser spot is also melted due to scattering and conduction through the solid material, neighbouring particles and capillary phenomena. The denudation zone is the adjacent area on both sides of the track that is left without powder (Figure 5a). The denudation zone influences the morphology of the tracks and layers. Variation in the powder layer thickness causes fluctuations of the melt pool volume and the resulting track height (Manfredi *et al.*, 2014; Yadroitsev *et al.*, 2015; Yadroitsev and Yadroitsava, 2015).

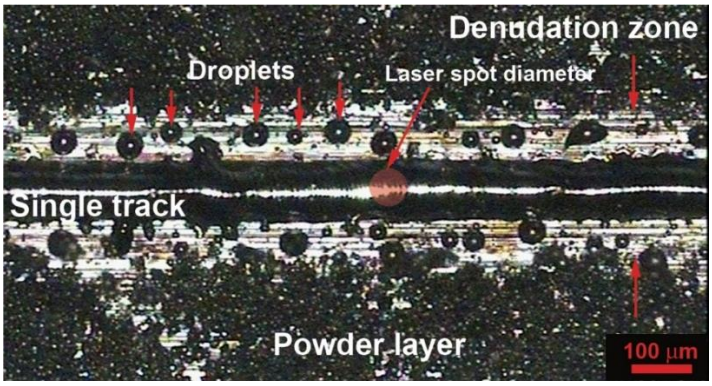

(a)

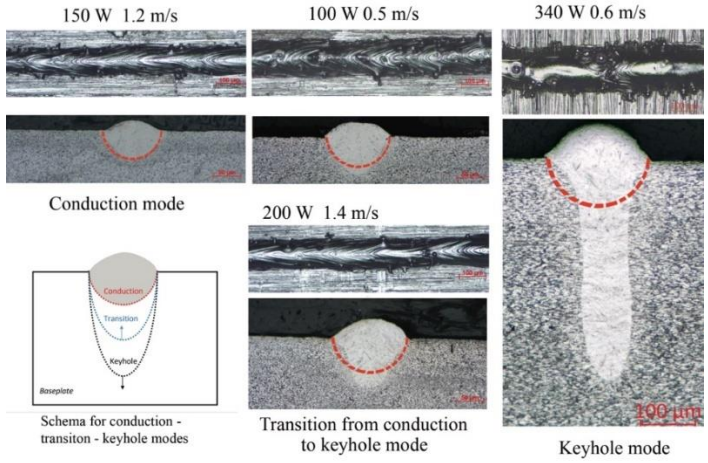

(b)

Figure 5: A single track on a substrate with powder showing denudation zone, droplets, and powder entrainment zone (a) and top view and cross-sections of single tracks in different modes of LPBF Ti6Al4V alloy with powder layer thickness ~60 µm. The red semicircular line shows the melt pool in conduction mode (Yadroitsev and Yadroitsava, 2021).

Yadroitsev *et al.* (2010) state that at low scanning speed and instability of the molten pool is caused by an increase in melt volume and decrease in melt viscosity. Reducing laser power at low speeds influences the penetration and thus reduces the stabilizing effect that penetration gives to the molten pool. Instabilities, such as distortions and irregularities of the track, occur at low scanning speeds whilst at high scanning speeds it gives rise to a balling effect. If the energy is sufficient to maintain boiling and evaporation of the melt pool, the vapour recoil

pressure causes distortion of the tracks. If the laser power is insufficient, the track could form a sequence of drops.

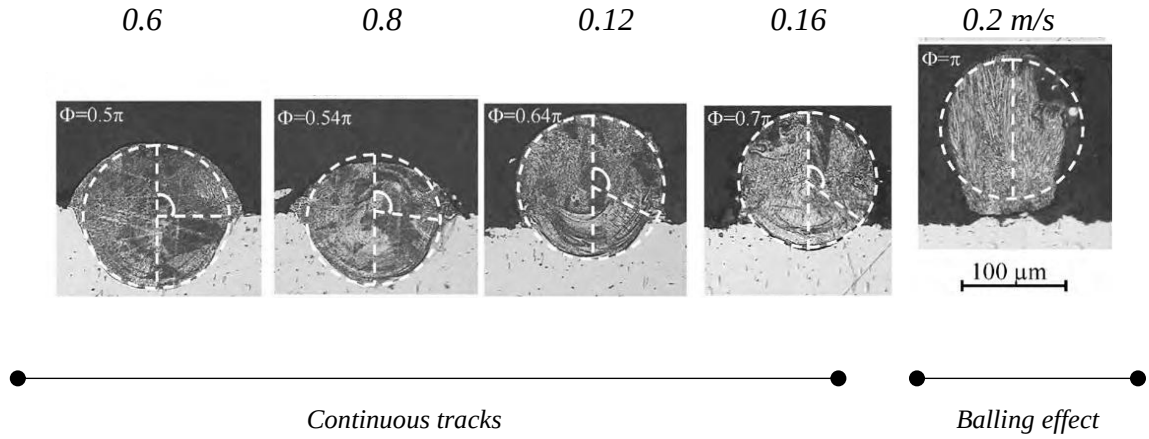

Figure 6: Cross-sections of 904L steel single tracks. Scanning speed indicated above each cross-section (adapted from Yadroitsev et al., 2010)

Balling is a disadvantageous phenomenon in LPBF (Figure 6). It occurs when the molten material does not wet the underlying substrate, due to surface tension, which tends to spheroidize the liquid. Balling leads to rough surfaces, obstructing smooth layer deposition and decreasing the density of the part. Since liquid metals do not wet oxide films in the absence of chemical reactions, it is important to avoid oxidation and have sufficient re-melting of previous layers to break down oxide films and provide a solid-liquid interface (Kruth *et al.*, 2004). Therefore, protective inert gas is used to prevent oxidation.

Yadroitsev *et al.* (2015) state that distortion, irregularities and balling effect (Figure 7) may be associated with the thermophysical properties of the materials: granulomorphometric characteristics of the powder and inhomogeneity in powder layer thickness; energy input parameters including laser power, spot size and scanning speed; melt hydrodynamics, etc.

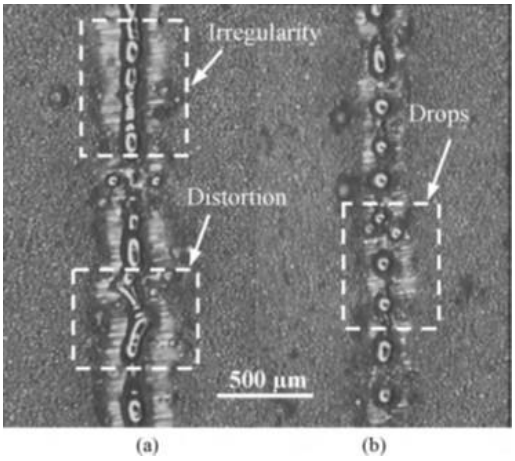

Figure 7: Unstable single tracks produced with 316L stainless steel: (a) P = 25W, (b) P = 12.5 W with powder layer thickness of 50 µm and scanning speed 0.02 m/s (Yadroitsev et al., 2010)

Vaporization occurs once the melt exceeds the melting temperature causing some of the material to evaporate. The evaporated material will expand and cause a recoil pressure on the melt. A low recoil pressure could contribute to flattening of the melt pool, but too high pressure could push molten material out of the pool. Care should be taken when comparing between these findings as the observations were made with laser melting experiments that were under vacuum (10^2 Pa) (Kruth *et al.*, 2004).

At optimal process parameters, LPBF tracks and layers are continuous and have stable geometrical characteristics (Figure 8). Single tracks produced by LPBF can be characterized into continuous tracks with regular geometrical characteristics (Figure 8, track B) and undesired irregular tracks (Figure 8, tracks A and C–D). Process parameters directly influence the formation of the single track. If the scanning speed decreases, it results in excessive energy input. In this case, keyhole mode and satellites occur during melting which leads to formation of porosity inside the 3D sample. At low effective power, the powder experiences lower temperatures; thus, the surface tension coefficient as well as melt viscosity increase leading to drop formation when the pre-balling effect starts (Figure 8, track C). Drop formation (balling effect) occurs where there is insufficient energy input because the surface tension breaks the melting single track into individual droplets (track D).

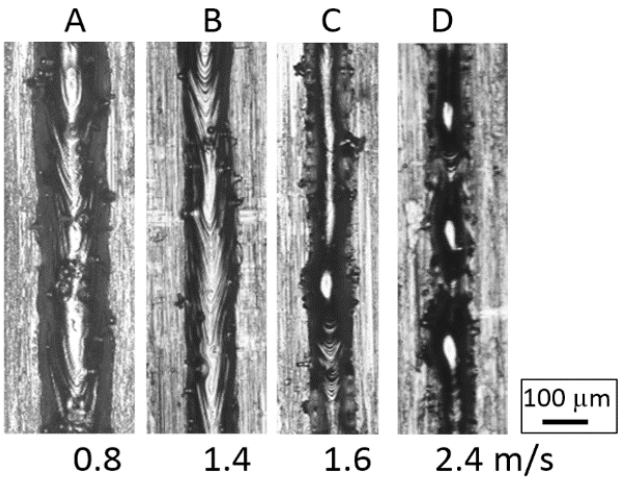

Figure 8: Ti6Al4V tracks produced at 200 W laser power and different scanning speeds (0.8–2.4 m/s) at 50 µm powder layer thickness

At high laser power with low scanning speed, there is an increase in melt volume and a decrease in melt viscosity and irregularities emerge. At lower laser powers with low scanning speeds, insufficient melting and penetration occurs, and if there is sufficient energy to maintain melting, vapour recoil pressures would cause distortion of sintered tracks. With a further reduction of laser power, balling occurs (Yadroitsev *et al.*, 2010).

Short interaction of the heat source and powder caused by the high scanning speed leads to rapid heating, melting and circulation of molten metal driven by surface tension and temperature gradients. During melting, drastic shrinkage occurs – the density increases from about 50% (apparent density) to 100% density once melted. The resulting heat flow will determine the geometry of the melt pool, the cooling rate and the transformation reaction in the melt pool and heat-affected zone (Kruth *et al.*, 2010).

Khairallah *et al.* (2016) uses a laser ray tracing energy source to show fluid flow due to Marangoni flow, recoil pressure and evaporative and surface radiating cooling. Marangoni flow in LPBF is driven by temperature difference in the molten metal which in turn results in a difference in surface tension and hence causes fluid flow. An important finding was the distinction between three the different regions: 1) a depression zone underneath the laser spot, 2) a tail-end region of the melt track located near the end, and 3) a transition region in-between, as shown in Figure 9. The depression has a complex flow and can be seen as the source of fluid. The transition zone has a surface velocity component (*Vx*) in the flow to the rear. At the tail, the backward flow starts to break up.

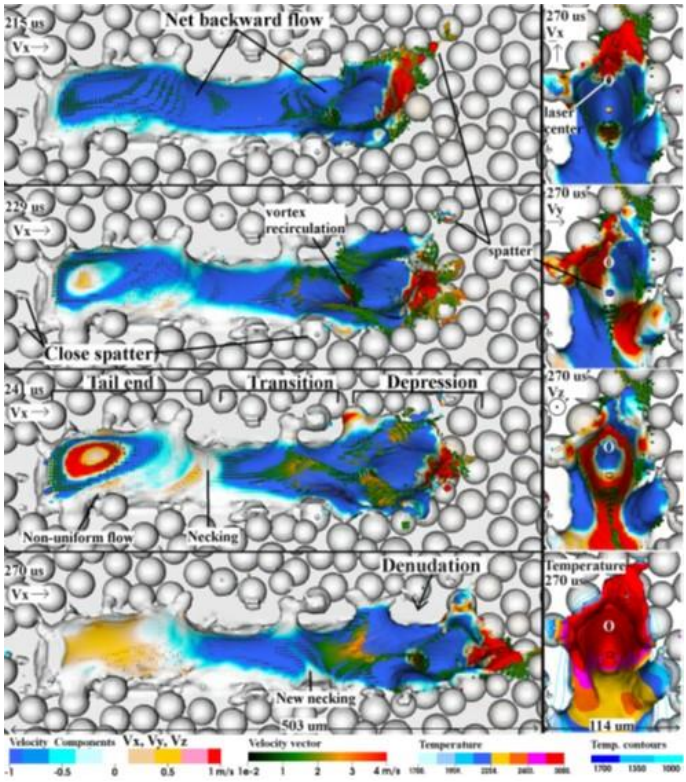

Figure 9: Denudation and spattering at different time stamps. The melt has a large backward flow (blue colour; Vx<0) due to Marangoni effect and recoil, compared to forward flow (Vx> 0; red colour). The backward net flow breaks up later in time at the necking. (Khairallah et al., 2016)

When the temperature and recoil pressure decrease, the surface tension increases causing the depression to close. The melt movement abruptly stops and can trap gas bubbles in the track. Molten metal will build-up in the front of the laser. The melt will run up the front wall of the depression and spill over and onto the particles ahead. If these particles are not drawn into the melt pool, they can form shallow lateral pores within the transition zones. At the end of single tracks, the laser is switched off and the large pool collapses due to sudden heat removal which causes pores. A possible solution is to slowly reduce the laser power at the end of single tracks (Khairallah *et al.*, 2016).

Matthews *et al.* (2016) showed that for metal LPBF, the gas and powder motion are important when analyzing the denudation zone and the incorporation of powder in the track. The process was investigated under vacuum and at atmosphere pressure using high-speed photography. A fibre laser with a spot size of ~50 μm was used inside argon atmosphere. Apart from capillary effect of the molten melt that pulls adjacent particles into the track, the intense heat causes the metal to evaporate which causes metal gas to rise, as seen in Figure 10 below.

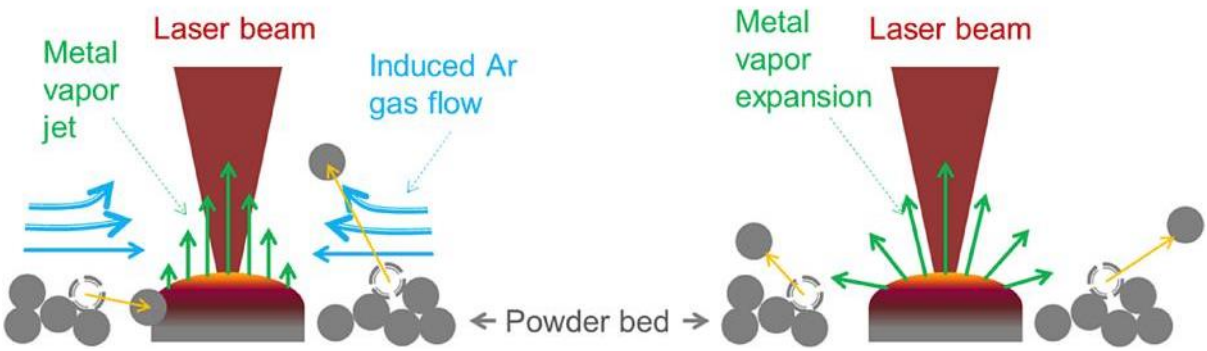

Figure 10: Diagram showing the action of evaporated metal flux on the flow pattern of the surrounding Ar gas and particles in the powder bed. Atmospheric (left) and low pressures right. (Matthews et al., 2016)

It was found that pressure affects the size of the denudation zone. It decreases, as with lower laser power, which is probably due to less evaporation at lower temperatures. It was observed that pressures above 220 Torr did not influence the size of the denudation zone. At 2.2 Torr, the narrowest denudation zone is observed. Below 2.2 Torr, the metal vapour expansion dominates, pushing the particles away from the melt pool. The gas flow and particle displacement affect the height of the track and the overall surface quality. Simulations were also carried out to rationalize the results, which showed that for Ti6Al4V a maximum surface temperature of about 3 000K and maximum vapour velocity of 700 m/s was reached at 225 W and 1.4 m/s (Matthews *et al.*, 2016).

Another study on flow by Bidare *et al.* (2018) stated that the powder bed fusion process is more dynamic than generally appreciated. They were the first to suggest that the effect of the laser plume and convection currents on the process should be considered. In their work they show that the powder particles and agglomerates are moved by metal vapour plume and plasma above the melt pool. They conducted all experiments with 316L powder in an argon atmosphere. It is shown how the particle spatter changes direction when compared to the scanning direction. At 50 W and 0.1 m/s, the particles are ejected forwards, the induced flow of ambient gas draws powder particles towards the melt pool from all directions and the powder is either involved in the melt pool or ejected forwards. At 100 W and 0.5 m/s, the plasma plume is vertically upwards resulting in less momentum and thus less denudation. At 200 W and 1m/s, the plasma plume is ejected backwards at an angle very close to the horizontal plane which causes the powder to be pushed away from the track causing denudation. In Figure 11, the effect of melt pool shape on the ejected particles can be seen (Bidare *et al.*, 2018).

Similar results were found by Zheng *et al.* (2018). They found that when keeping laser power constant, the laser plume tilts backwards increasing in angle as the scanning speed increases. The schlieren imaging done by Bidare *et al.* (2018) shows some of the gas flow present. Convection, FE vapour and eddy currents can be observed in Figure 11.

Bidare et al. (2018) state that flow not only contained a plume of Fe vapour but also contained plasma. High velocities of flow were predicted via simulation: up to 800 m/s from plasma and 10 m/s for radial gas flow. The radial gas flow exerts force on the particles dragging them towards the laser.

Trapp et al. (2017) investigated laser effective absorptivity of LPBF by directly measuring the resulting temperature in the specimen at different scanning velocities and conditions. The influence of laser parameters on the absorptivity was considered with and without powder. It is a known fact that the keyhole regime has a great influence on the amount of laser power being absorbed due to multiple light reflections which interacts with keyhole walls. For a fixed scanning speed of 500 mm/s, varying laser power induced higher absorption (Figure 12) once keyhole started. Absorption reaches a maximum once keyhole depth reaches 300 µm. For 316L stainless steel, a clear distinction was found between the absorption values of a powder layer compared to no powder. For powder layers at low laser power, the absorption is higher, but once keyhole starts, absorption follows the same trend as solid material. The thermal conductivity of metallic powder, such as nickel-based super alloy 625 (IN625) and titanium

alloy (Ti6Al4V), is approximately 3 to 7% compared to their solid thermal conductivity (Zhang *et al.*, 2019).

Hooper (2018) measured temperature fields during LPBF using a two-wavelength imaging setup in a standard Renishaw AM250 machine. He found high temperatures for Ti6Al4V, as high as 4 000 K, which is above the boiling point (3 560 K). At different process parameters the cooling rates were in the range of 1–40 K/µs. Higher average temperatures are found after scanning on powder, as when scanning overhangs, because the thermal conductivity of the powder is less than that of the substrate resulting in a long melt pool tail.

Apart from the thermal conductivity of the powder and solid, surface tension also has an influence on the heat transfer due to fluid flow in the melt pool. Zhao *et al.* (2010) show that for laser welding, an increase in surface active elements, such as oxygen in laser spot welding (stainless steel), different oxygen concentrations (0.1 to 1%) changed the surface tension and impacted the Margoni flow leading to a change in melt pool shape. The oxygen content also leads to an increase in laser absorption (Boley *et al.*, 2016).

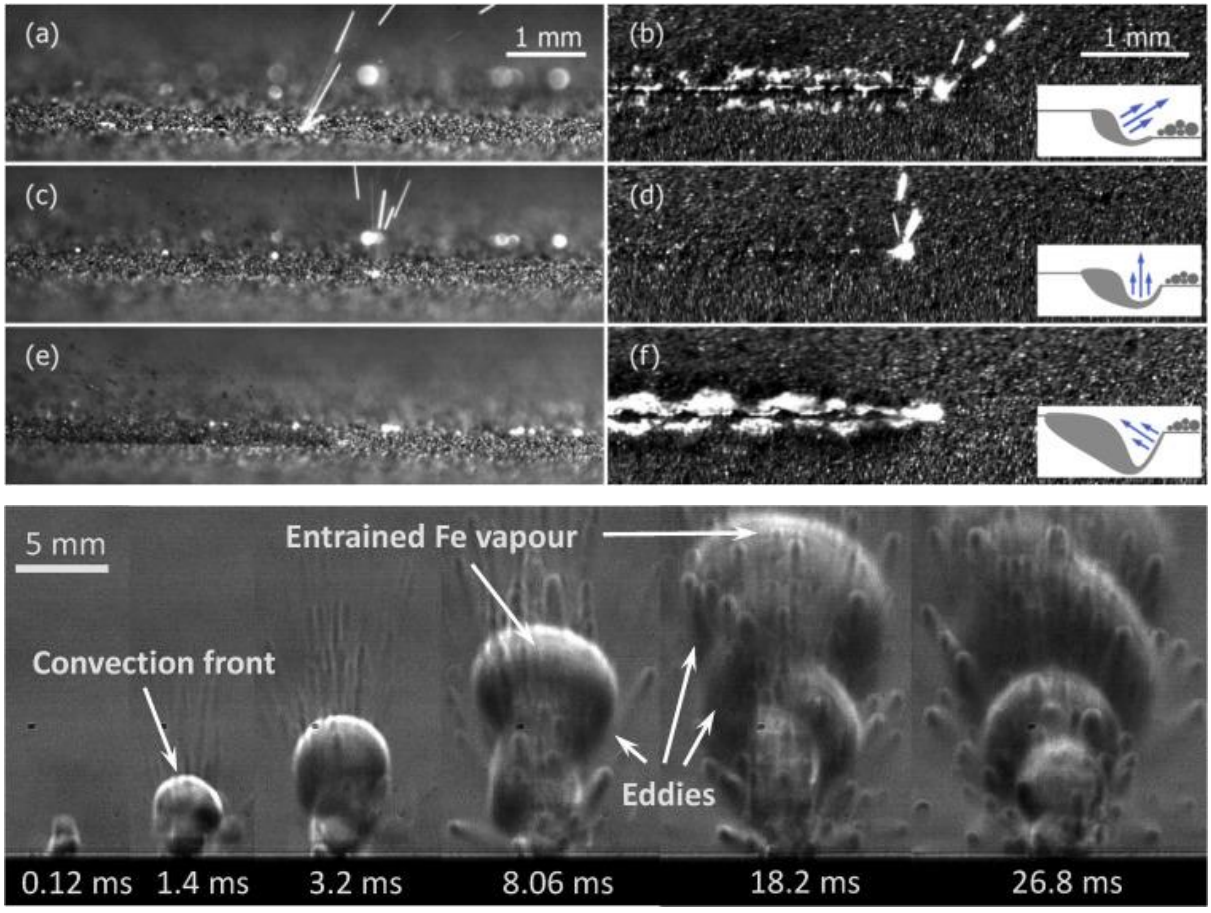

Figure 11: Top and side view of laser scanning (left to right) at different process parameters with schematic of melt pool shape which determines laser plume direction. 50 W and 0.1 m/s (a) and (b); 100 W and 0.5 m/s (c) and (d) and 200 W and 1 m/s (e) and (f) Bottom showing schlieren imaging of scanning towards the camera at 100 W and 0.5 m/s (Bidare et al., 2018)

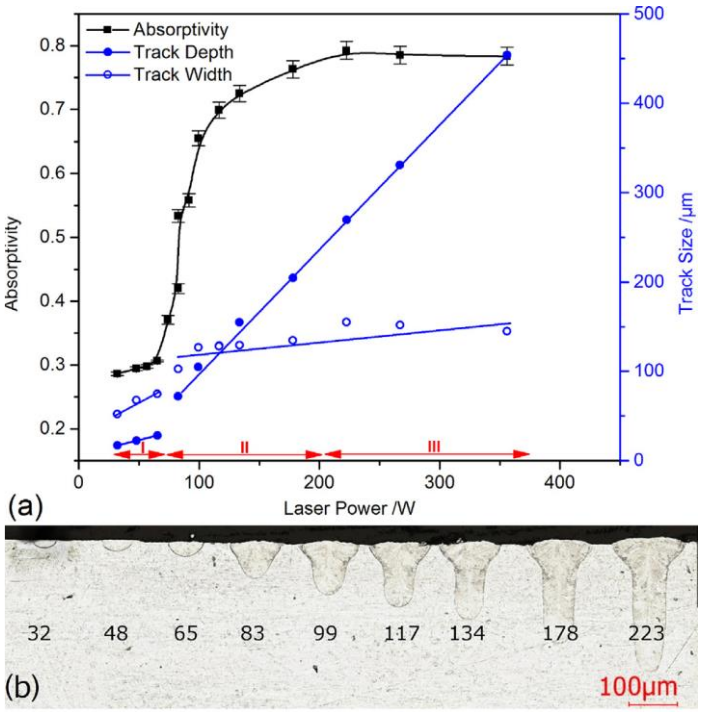

Figure 12: Absorptivity for 316L stainless steel at different laser power at constant scanning speed of 500 mm/s−1. (a) and optical metallograph of cross-section with the laser power corresponding to each track indicated (Trapp *et al.*, 2017)

2.1.2 Single layer formation

A single layer is created from a sequence of single tracks. Because of the denudation zone near the first track, there would be less powder involved in the second track; thus, the melt pool and resulting track would be different from the former track, see Figure 13. Inhomogeneous layer thickness in the next powder layer can result in a defective part (Yadroitsev & Smurov, 2011; Yadroitsev *et al.*, 2015).

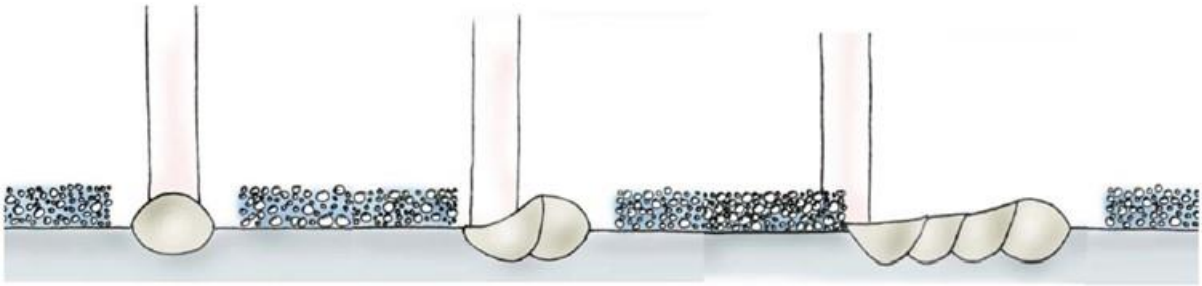

Figure 13: Schematic showing how denudation affects track height (Yadroitsev & Smurov, 2011)

The surface of single layers is dependent on the shape of the single tracks, scanning strategy and hatch distance. The scanning strategy will have a direct influence on density, residual stresses and microstructure formed during LPBF. If the layer thickness is too high, no optimal adhesion to the substrate or previous layers can occur because of the inadequate melting depth. Therefore, a change in sound of the consecutive tracks from the layer would be expected.

2.1.3 Three-dimensional objects

In LPBF, different process parameters are used for different parts of the 3D object. Different parameters are assigned for areas such as overhangs. EOS refers to these areas as down-skin, up-skin and core (Figure 14). These strategies improve surface quality, metallurgical contact, joining among overlapping zones and material properties.

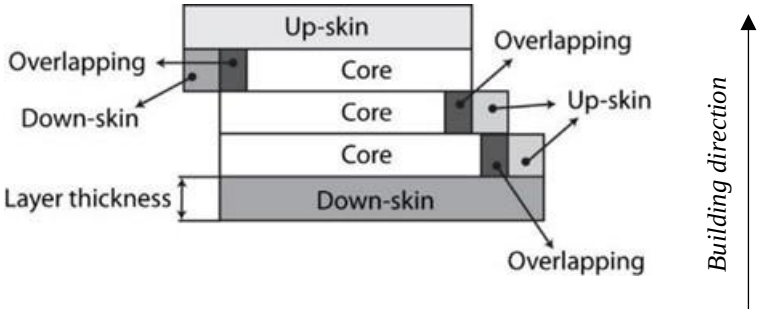

Figure 14: EOS 3D scanning strategy segments (EOS Training Manual, 2012)

Post-processing of LPBF components includes polishing and heat treatment to change material properties and reduce stresses; HIP is used for reducing porosity and also for changing the material properties. To produce a metal product that is dense with good mechanical properties, three main categories with their sub-categories need to be addressed, as shown in Figure 15.

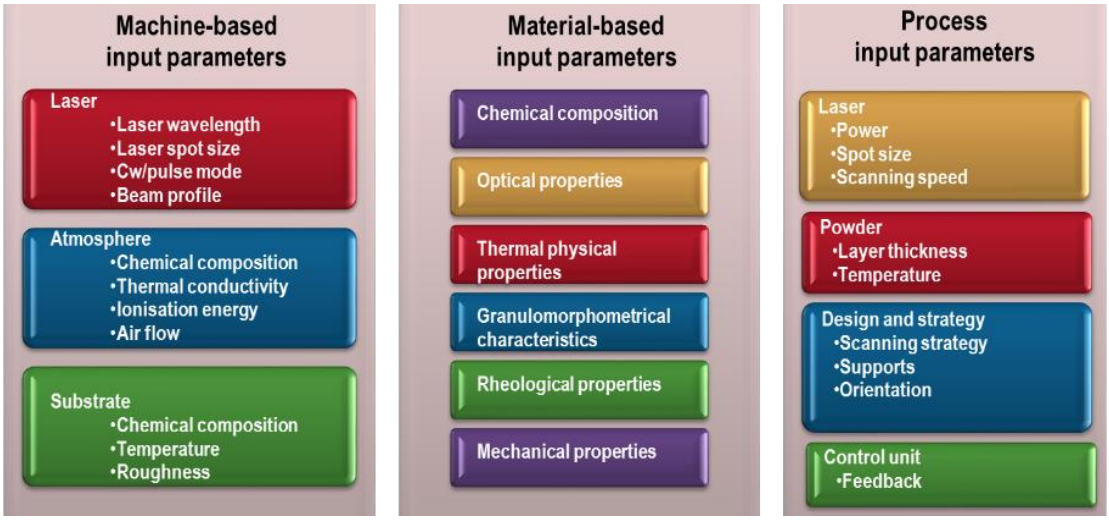

Figure 15: LPBF parameters (Yadroitsev, 2009)

All these properties interplay and determine the resulting part quality. Changing one parameter, like the powder (chemical composition of particle size distribution), can change the laser-powder interaction and result in defects such as porosity.

2.1.4 Summary

The LPBF process is a parameter-sensitive process – a slight change in one parameter could have a great influence on the outcome. The sensitivity of the LPBF process makes testing and quality control all the more necessary. To produce a 3D object, the primary tracks of each layer need to be created at optimum laser power, scanning speed, hatch distance, etc. The quality of the consecutive layers is influenced by the scanning strategy which also determines the temperature gradients, internal stresses and resulting microstructure. This along with the shape of the part determines the optimal heat input to produce defect-free objects. A non-optimal heat input could result in defects such as pores, cracks, delamination, part distortion, etc. AE could record the whole process - from powder delivering to the melting, solidification and cooling of the manufactured part. Acoustic waves originated from all phenomena in the processing chamber, even noise from recoater collision with manufactured parts (if it happens) – can give useful information about the LPBF process.

A laser-matter interaction induces heat flow and stresses inside the LPBF manufactured part and baseplate; it also causes flows in a chamber filled by protection gas. These physical phenomena produce unique acoustic waves that can be registered to give information on the laser-powder interaction process. For single track formation, the gas flow caused by pressure drops inside the evaporated jet entrain powder particles surrounding the melt pool into the LPBF process; the vapour jet changes due to the laser parameters. The direction and amount vapour being ejected from the melt pool can possibly be detected by studying gas borne AE signals. The amount of energy absorption is also dependent on the process parameters (laser parameters, chemical composition, laser mode etc.) which can possibly decrease or increase the AE signal amplitude. A correct filtering and processing of AE signals, as well as their recognition with finding the correlation of acoustic signals with the formation of defects for the manufacturing process is a promising direction for quality control of LPBF parts.

2.2 Main concerns of LPBF

Due to the layer-wise building process of LPBF, porosity is a huge concern, apart from the fact that it directly influences material properties such as fatigue, interlayer pores can be detrimental to the structural integrity of the part especially at thin sections. The density is directly linked to the process parameters and scanning strategy.

2.2.1 Sources of defects

Possible defects in 3D parts are partly due to the high number of process variables, as discussed in more detail in a comprehensive review of in-situ monitoring in Grasso and Colosimo (2017).

If the molten pool exceeds the boiling point of the material during laser scanning, a keyhole regime, and finally a porosity regime, could initiate. To avoid pore formation, process parameters should be adapted to avoid temperatures above the boiling point of the material. Although penetration into the substrate and/or adjacent tracks is necessary for cohesion, too deep penetration leads to keyhole porosity whereas too low penetration and balling effect lead to lack of fusion porosity (Yadroitsev *et al.*, 2015).

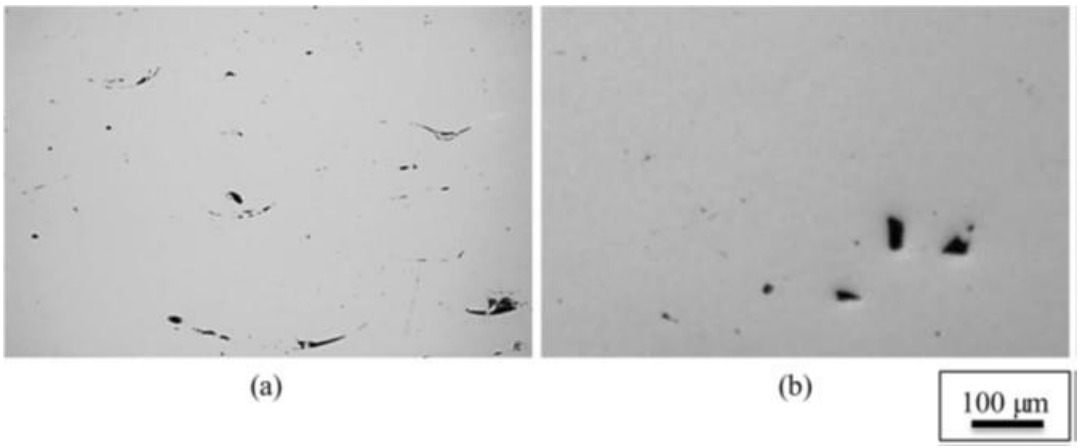

Figure 16: Specimens built using rescanning strategy at laser power of 50 W (a) and 70 W (b) at a scanning speed of 0.12 m/s, powder layer thickness 50 µm and hatch distance 120µm (Yadroitsev et al., 2015)

In Figure 16a, the sample had elongated pores which were formed between the layers, i.e. inter-layers pores. The deposited layer was too thick for the chosen energy input, and porosity resulted from the lack of fusion at the layer boundaries. With the increase in power, inter-layer pores disappeared and the shapes of the residuary pores changed (Figure 16b). An increase in laser power may also result in undesirable effects. Higher energy input can cause high temperatures, overheating, boiling and evaporation of material in the laser interaction zone and irregular track formation (Figure 16).

Non-optimal hatch distance can result in formation of gaps between tracks in a single layer, which cause a chain of pores in the final object (Yadroitsev *et al.*, 2015). Scanning strategy is an important consideration as it directly affects the density of the part. Yusuf *et al.* (2017) found that the pores occurred at the contours of the tracks when the island scanning strategy was used; they wrongly attributed the pores to inclusions. At the end of the track, as the laser is turned

off, the vapour depression rapidly collapses and solidifies causing gas bubbles to be trapped (Martin *et al.*, 2019a).

In-situ studies of LPBF using X-ray have given much insight into the process (Martin *et al.*, 2019a; Martin *et al.*, 2019b; Zhao *et al.*, 2017). Where oscillatory motion was observed, it is thought that the motion was caused by laser reflection from the front wall of the vapour depression zone, which causes the rear side to experience more radiation and change shape. This causes waves that periodically result in instabilities. This is the reason for the occurrence of porosity during steady-state operation (Figure 17) (Martin *et al.*, 2019a).

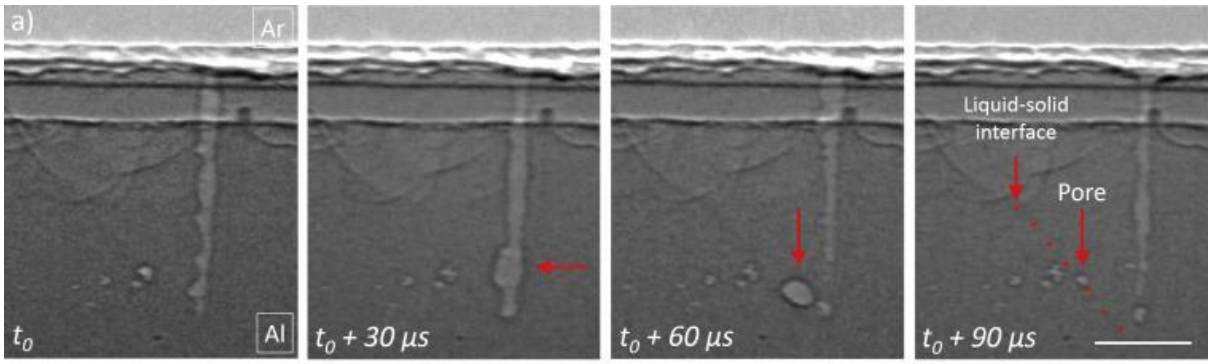

Figure 17: X-ray images showing steady-state pore formation during laser irradiation of Al6061, laser power of 400 W and a scan speed of 800 mm/s (Martin et al., 2019a)

Powder particle size distribution has a direct effect on laser absorptivity and, therefore, can influence the quality of the part (Zhou *et al.*, 2019). Powder recoating forms a large part of the LBPF process and as powder recoating has a direct link with final part quality, recoating a homogeneous layer will ensure that the correct amount of material is involved with each laser interaction. Apart from powder-based properties, density of the powder layer after recoating is influenced by machine parameters such as the recoating blade type and material, recoating speed, powder dosing and the applied pressure (Spears and Gold, 2016). During LPBF, the laser scans a thin pre-deposited powder layer. If powder was agglomerated, an inhomogeneous powder layer leads to porosity in the sample, as shown in Figure 18.

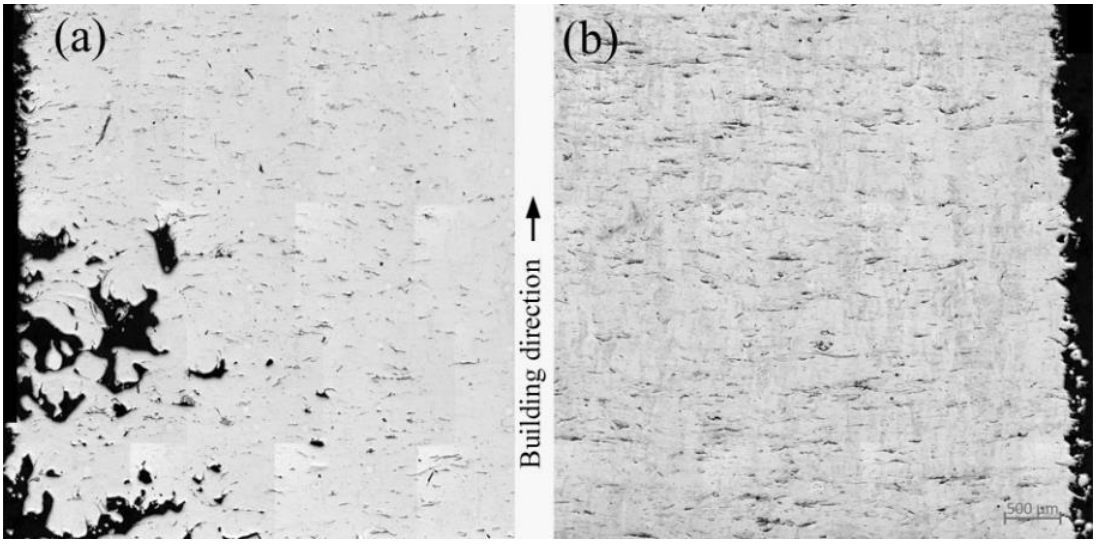

Figure 18: Ti6Al4V-1% Cu samples produced at the same process parameters: a) porosity from powder delivery; b) sample free from defects.

Other sources of defects are changes in laser power, scanning speed, non-optimal hatch distance, etc. The power of the laser beam determines the depth of penetration into the substrate and the layer thickness controls the amount of powder involved in the melting process (Yadroitsev, 2009; Yadroitsev *et al.* 2015). The minimum defect size has to be determined in order to be able to qualify LPBF parts (Hirsch *et al.*, 2017; Lu and Wong, 2018).

In LPBF, a high temperature gradient is present due to the locally concentrated energy input which leads to high residual stresses. When the specimen is exposed to the laser beam, the rapid heating of the upper surface layers accompanied with slow heat conduction causes a steep temperature gradient. This results in compressive strains occurring in the bottom layers, because the surrounding material restricts free expansion of the top layers during heating (Figure 19a). During cooling, the tensile upper layers become shorter than the bottom layers and bend towards the laser. The way in which these stresses are generated causes the consolidated layers to bend towards the laser beam, which in turn could result in distortion and part failure by delamination or cracking. The cooling of layers below the top layers also adds to the tensile stress in the part as the layers shrink while their temperature decreases (Kruth *et al.*, 2004). In LPBF parts, residual stress is a concern because it could cause part distortion, fracture and reduce the strength of the part (Kruth *et al.*, 2010).

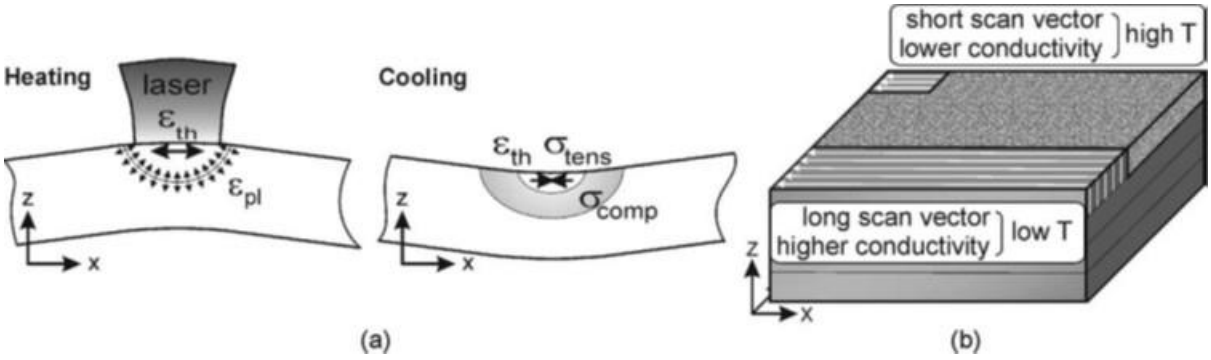

Figure 19: Tensile and compressive stresses during heating and cooling (a), short and long single tracks (b) (Kruth et al., 2004)

These stresses could result in deformation of the part during manufacturing, as shown in Figure 20, and distortion and cracks can occur when removing the component from the substrate on which it was produced (Yadroitsava & Yadroitsev, 2015). It will be shown later that such delamination causes stress waves which in turn can be measured using acoustic emission sensors as part of the online monitoring process.

An important consideration during the design of AM is how the building orientation influences the tensile properties, i.e. anisotropy. The pore shape and size has been shown to be the main cause of pore growth and crack formation during quasi-static tensile testing (Krakhmalev *et al.*, 2016).

(a)

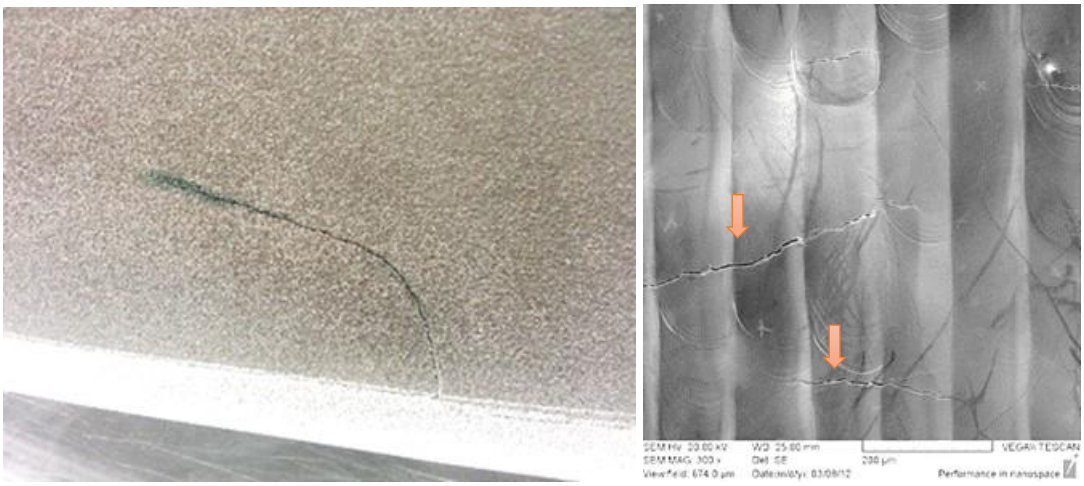

(b) (c)

Figure 20 : Ti6Al4V part delaminating while manufacturing (a), macro-crack of part attached to substrate (b) and SEM image of the top layer of TiAl part with micro-cracks (c) (Yadroitsava and Yadroitsev, 2015)

Heat treatment is seen as the most effective way to reduce residual stresses created during the manufacturing process. Heat treatment should be applied before removing the parts from the substrate. Vrancken *et al.* (2015) showed that pre-heating the substrate during LPBF of Ti6Al4V can reduce residual stress and increase ductility.

Residual stress of as-built Ti6Al4V specimens attached to the substrate is high near the surface (800–900 MPa), with the major component being in the direction of scanning (Van Zyl *et al.*, 2016). During manufacturing, slight distortion is not reason for much concern; however, deformations that disturb the building process are undesirable. If delamination occurs it can vibrate and cause the powder to move in such a fashion as to disturb the process, as shown in Figure 21, or a protruding part can obstruct the recoating mechanism.

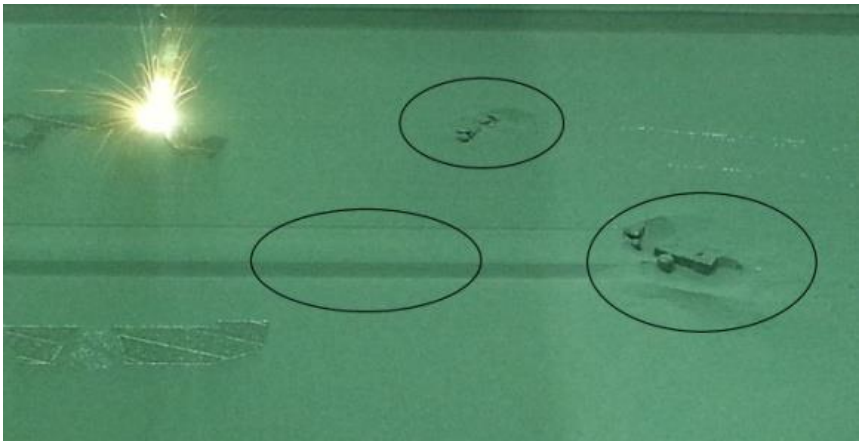

Figure 21: Vibration during LPBF process causing powder to move and form valleys in the powder bed (Van Zyl et al., 2016)

The current state is such that published reports on mechanical and especially fatigue properties of LPBF parts vary widely between different studies (Lewandowski and Seifi, 2016). The causes of these differences are often attributed to porosity (du Plessis *et al.*, 2020), surface roughness (Beretta *et al.*, 2020), microstructure (Gu *et al.*, 2012) or residual stress (Bartlett and Li, 2019). Various post-process methods can be used to reduce porosity, for example, HIP (Cai *et al.*, 2016; du Plessis and Macdonald, 2020), to remove residual stress (heat treatment) and to improve accuracy and surface roughness. For optimized process parameters in a commercial system with a well-controlled build process, including appropriate post-process heat treatment and machining of specimens, mechanical performance can be superior to that of cast or forged metals (Yadroitsev *et al.*, 2018).

2.2.2 Summary

Porosity and residual stress remain a concern for LPBF components, as they are not only important factors in part quality, but also in fabrication. The material properties of LPBF Ti6Al4V compare well with that of wrought and other manufacturing methods. Properties of LPBF components are directly drawn from the process parameters involved during manufacturing. It was shown that one parameter can cause significant changes; one such change is scanning speed, which was shown to directly influence the density of the part. It is seen that the way in which the powder interacts with the laser is very important to ensure that optimal processes are maintained. Any disturbance in the powder layer, such as delamination or warping of the parts, can cause variations in the powder layer leading to defects such as lack of fusion porosity. This is also the reason why powder layer monitoring has received much attention in AM quality monitoring research. It is hypothesised that the use of AE monitoring can recognize lack of fusion porosity and therefore should be investigated.

2.3 Quality control and monitoring in AM

In AM, the variation in part quality and mechanical properties, due to the presence of defects, surface roughness and residual stress, can limit its use in high-value or mission-critical applications. Quality assurance and certification becomes all the more important in the production of safety-related AM components, e.g. the aeronautical, automotive and medical industries. Certification can be obtained by various means including the manufacturing of ancillary test specimens or non-destructive testing (NDT) using computer tomography.

Another option is to monitor the process during building; the layerwise build-up process of AM allows for detailed monitoring (Krauss *et al.*, 2014; Selfi *et al.*, 2016). The National Institute of Standards and Technology (NIST) has developed projects that aim to aid the qualification of AM. Some of the programmes include: *Additive Manufacturing Part Qualification, AM Machine and Process Qualification* and *Real-Time Monitoring and Control of Additive Manufacturing Processes,* the latter having the objective to "*Develop process metrology, in-process sensing methods, and real-time process control approaches to maximize part quality and production throughput in Additive Manufacturing (AM).*" (NIST, 2020).

When considering the use of conventional NDT methods like ultrasonic or X-ray testing which are readily used in industrial applications, some current challenges in AM technology are: rough surface finish, complex geometries, variable and complex grain structure, undefined defect types, sizes and shapes, lack of physical reference standards, lack of effect-of-defect studies, lack of probability of detection information, lack of written inspection procedures for AM processes, lack of mature in-process monitoring techniques.

2.3.1 Destructive testing

Tensile and metallographic testing is often used to accurately quantify the mechanical properties and defects such as porosity of LPBF parts. Although destructive testing is accurate, it only applies to the particular sample being tested, although it is assumed to be a good representative of the material or part being tested.

For AM, tensile testing is often used to verify material properties, for example the ASTM F3001 – 14 (11.4: Mechanical Properties), which specifies that Ti6Al4V tensile samples should be produced in the vertical and horizontal directions and values should be obtained depending on the type of post-processing applied. The tensile properties should be tested according to ASTM E8/E8M (Test Methods for Tension Testing of Metallic Materials) in both the vertical and horizontal directions due to the anisotropic nature of AM. The minimum tensile strength,

yield strength (0.2%) and elongation values for the stress-relieved or annealed condition are 825 MPa, 760 MPa and 8%, respectively, for both the horizontal and vertical directions. As-built LPBF exceeds the strength requirement by far but fails the ductility requirement.

2.3.2. Non-destructive testing

2.3.2.1. Introduction

Non-destructive testing refers to the various techniques used to monitor the health of a material, component, or system in a structure without causing damage. NDT can detect potential failures as well as inform users of the appropriate time to replace their components to increase the safety and performance. NDT is a valuable and critical technique in many industries as it can save both time and money in product evaluation, troubleshooting and research (Chen, 2014). Hellier (2012) remarks that for those who wonder where NDT began, there are some who would answer by referring to the creation of the heavens and earth in Genesis: "*In the beginning, God created the heavens and the earth and He saw that it was good*". This has been identified as the first non-destructive test – a visual test!

Discontinuities can be categorized by the stage wherein they are generated:

- Inherent discontinuities: generated in the original production of an alloy stock material.
- Primary processing discontinuities: occurring in the first forming stages from a primary alloy.
- Secondary processing discontinuities: occurring in subsequent forming and finishing steps.
- Service discontinuities: created during the use of a component (Hellier, 2012).

When considering the applicability of NDT methods to be used on LPBF components, it is of great importance to understand the nature of the parts, formation of defects and NDT equipment. Failure to acquire the necessary background knowledge exposes the engineer to misinterpreting the results obtained (Carino, 2013; Hellier, 2012). Therefore, a thorough study of the LPBF process and the formation of defects are necessary to select a LPBF NDT method.

Some NDT techniques that can be used for quality control in AM are visual, ultrasonic, Eddy current, radiographic, magnetic methods, liquid penetrant test, shearography, acoustic and thermography (Sharrat, 2015; Yusof *et al.*, 2017).

2.3.2.2 X-ray computed tomography

Presently, X-ray computed tomography (CT) remains the most trusted method of ensuring that an AM component is free of defects before enlisting it to service. Since the introduction of

dimensional CT metrology, intricate components produced by AM can be inspected for geometrical and tolerance quality control, which is not possible in any other way, as there are no methods to measure internal geometries. CT is a very useful tool for accuracy measurements, especially for control of the inner walls and complex inner structures, their size and locations. CT combined with AM technology is often used in reverse engineering with applications in the medical, industrial, archaeological and historical fields (du Plessis *et al.*, 2016; Kruth *et al.*, 2011; Kim *et al.*, 2016; Maskery *et al.*, 2016).

X-ray CT is used by various authors to study different AM phenomena such as pores and defects (Aloisi and Carmignato., 2016; de Chiffre *et al.*, 2014; du Plessis *et al.*, 2014; Karme *et al.*, 2015; Ziółkowski *et al.*, 2014), volumetric density, dimensional accuracy (Kim *et al.*, 2016), surface roughness/topography (Townsend *et al.*, 2016) and powder analysis (Du Plessis *et al.*, 2018). With reference to CT-scans, it is important to note that image quality and the amount of detail that can be seen varies significantly between different scans and systems (du Plessis *et al.*, 2016b).

2.3.2.3 Acoustic testing

Acoustic emission testing (AE) is based on the principle that elastic stress waves (i.e. sound) are generated by the rapid release of energy in the material due to relaxation of the stress and strain fields. AE generally refers to waves that arise from various energy sources which induce vibration or pressure waves, which are in turn monitored by a sensor and correlated to specific events. AE can be used in different stages; during manufacturing, after manufacturing, and whilst in service. When AE is applied during manufacturing, it serves as a health/quality monitoring tool and when it is applied post-manufacturing or post-service, AE determines the condition of the part. AE is used in online health monitoring of pipes and pressure vessels, leak detection, rotating equipment, production line components and structures subject to stress and loading. Table 1 shows the advantages and limitations of AE.

Table 1: The advantages and limitations of AE (Hellier, 2012; Raj *et al.*, 2007)

Advantages	Limitations
Large components (pipes, etc.) can be monitored, less sensitive to geometry	Sensors often need contact with surface
Can possibly predict failure	Multiple sensors needed for flaw detection
Continuous monitoring (online)	Signal interpretation required

The terms used to describe testing methods are often used interchangeably and incorrectly for different testing methods. These terms are especially confusing because variations of these methods can be applied either while producing the component, during service or after production. For AE, a common misinterpretation arises with the term “AE” as it is commonly accepted to mean the use of an ultrasonic transducer attached to an object to monitor the health of the component, such as a machine during operation, i.e. online monitoring.

Another AE method measures the resonant frequency of a component. The resonant frequency varies with the material properties, density and dimensions. If the resonant frequency of the component being tested moves away from the frequency of a known good part it indicates that the part is faulty. An example would be a crack that reduces the stiffness of the part causing the resonant frequency to fall (Stultz *et al.*, *2005;* Bono *et al.*, 2010; IMCE, 2020; The Modal Shop, 2020).

The fact that energy can induce vibrations which in turn can induce sound should be kept in mind for online monitoring of LPBF. Components from the machine can vibrate due to the normal operation and/or the induced vibrations due to processing. In some instances, the part being manufactured might present certain vibration.

2.3.3 Monitoring of LPBF process

Online monitoring, or in-situ monitoring, commonly refers to data collection of a system or process; for different industries and applications it can be to monitor the health of a structure during service or monitoring the production cycle to verify that no deviation in parameters occurred. A simple example would be the use of a workload thermocouple that is attached to a metal part during heat treatment. The temperature profile can be monitored and used during the process to adjust the process and afterwards form part of a quality assurance document. For AM, online monitoring is preferred as CT scanning is often difficult and time-consuming and adds to the cost. Table 2 shows a summary of online monitoring systems that are commercially available for LPBF and laser processing.

Table 2: Summary of LPBF and laser weld process monitoring systems (Adapted from Spears and Gold, 2016)

Company	Module Name	Method
B6Sigma	PrintRite3D®	Sensor suite (SENSORPAK™) still under development (in 2016), but includes optical, thermal, and spectral "off-the-shelf" sensors. INSPECT™ software links process data to quality metrics
Concept Laser	QM modules (QMmeltpool, QMlaser, QMpowder, QM atmosphere)	Lagrangian camera and photodiode monitoring of melt pool with 3D visualization; laser power monitor; powder bed imaging system; and build atmosphere monitoring
EOS GmbH/ plasmo Industrietechnik GmbH	EOSTATE Meltpool and EOSTATE PowderBed	Lagrangian and Eulerian photodiode melt pool monitoring; powder bed imaging system
Precitec	Laser Welding Monitor	Temperature, back reflection, plasma, and CMOS camera monitors, for laser welding
Prometec	Welding Monitor PD 2000 and Plasma Monitor PM 7000	CMOS camera for melt pool imaging; IR and UV photosensor for monitoring melt pool emission
SLM Solutions	Quality Assurance System modules	Lagrangian two-colour pyrometer for melt pool monitoring; laser power and powder bed monitors
Stratonics	Surface ThermaVis®	Two-wavelength imaging pyrometer

Only a few commercial in-situ monitoring systems are available at present, as outlined in Everton *et al.*, 2016; Spears and Gold, 2016; Yadav *et al.*, 2020, mainly in the form of imaging devices and pyrometers. Cameras monitor the homogeneity of the selectively melted layer and/or the powder layer deposited by the delivering system. Thermal cameras are used to monitor the melt pool size and shape, temperature, and aim to measure the stability of the melt pool. Variations in the characteristics of the melt pool are indicative of potential defect formation or an unstable process which can lead to porosity formation. Thermal cameras are also used to check local temperature hotspot generation, such as in sharp corners of parts, as high temperatures lead to an irregular process with higher likelihood of porosity formation or surface roughness. Despite the efforts in this domain and the availability of commercial tools, the approach is still not optimized and limited success has been achieved. Some of the drawbacks are the large data sets and the challenges in handling this data at high processing speed. Yadav *et al.* (2020), in a review of online monitoring of AM concludes that online monitoring for AM is still in its infancy. The conclusion is backed up when looking at the growth of commercially available systems in 2016 (Table 2) compared to 2020 (Table 3).

Table 3: Commercial LPBF monitoring systems (Adapted from Yadav *et al.*, 2020)

Module Name	Developer	Monitored Quantity	In-situ Sensing
QM meltpool 3D	Concept Laser	Melt pool (area and intensity)	Co-axial photodiodes (co-axial camera also available in research version)
EOSTATE MeltPool	EOS	Melt pool	Co-axial and off-axial sensors
EOSTATE & Exposure OT	EOS	Thermal map over the entire powder bed	Off-axis camera
Melt Pool Monitoring (MPM) system	SLM Solutions	Melt pool	Co-axial pyrometer
Layer Control System (LCS)	SLM Solutions	Powder bed	Off-axial camera
InfiAM	Renishaw	Melt pool	Co-axial photodiodes
Truprint Monitoring	Trumpf	Melt pool	Co-axial photodiodes (beta version)
Truprint Monitoring	Trumpf	Powder bed and part geometry	Off-axial camera
	SISMA	Powder bed	Off-axial camera
PrintRite3D	B6 Sigma, Inc.	Different monitoring equipment	Set of co-axial and off-axial sensors available

Craeghs *et al.* (2011) showed how closed-loop control can be implemented during online monitoring of LPBF using two different methods: engineering process control (EPC) algorithms to control the scanning parameters in real-time, and/or using methods from statistical process control (SPC) to detect 'abnormal' variations in the melt pool output, which are caused by a disturbance, as shown in Figure 22.

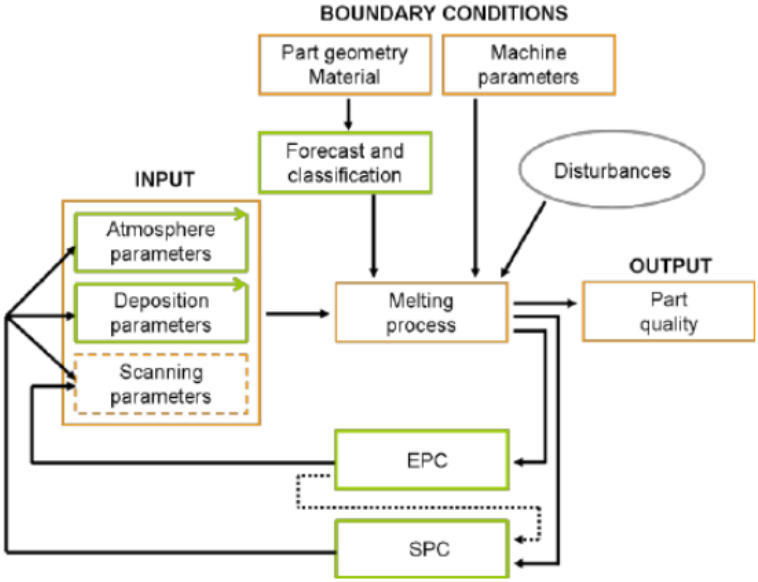

Figure 22: Proposed method for online monitoring of LPBF by Craeghs et al., (2011)

During LPBF, the melt pool glows and emits light corresponding to the temperature of the melt. The emitted light follows the law of Planck. These different light intensities can then be detected by a camera resulting in an image with different grey values which correspond to a particular temperature. This high-speed imaging setup can result in large amounts of data, of up to 75.1 GB of images every second. In contrast, recording with a 24bit microphone at 100 000 samples per second would result in 0.3MB/s. Berumen *et al.* (2010) proposes that the solution is to use the measure the temperature directly through the scan head, as shown in Figure 23. A semi-transparent mirror is used to measure the transmitted light from the laser interaction zone with a camera and diode.

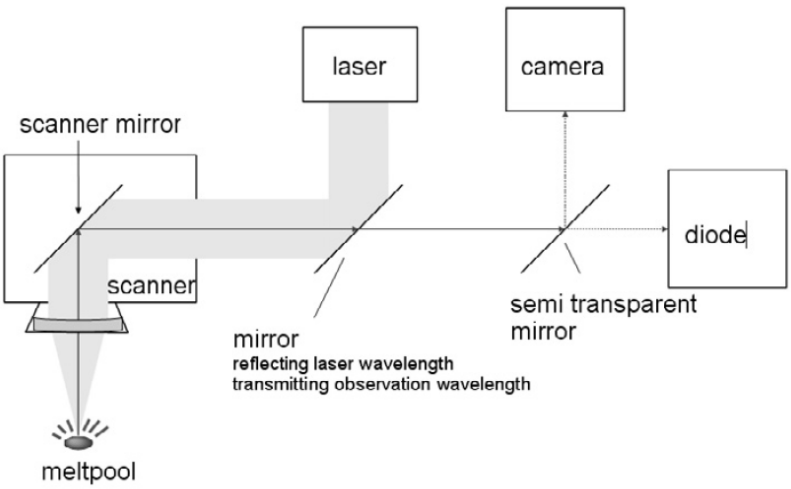

Figure 23: Schematic of online melt pool monitoring (Berumen et al., 2010)

This setup reduces the size of the images. The diode is used to measure intensity while the camera looks at the melt pool dimensions. This method is patented by Concept Laser along with Katholieke Universiteit Leuven. They found that this reduced the data size to 636 MB per second. When the powder layer is thick, conductivity is lower resulting in higher melt pool temperatures. These higher temperatures are then measured by the photo diode, as shown in Figure 24, where a part was built with increasing the thickness of the consecutive layers.

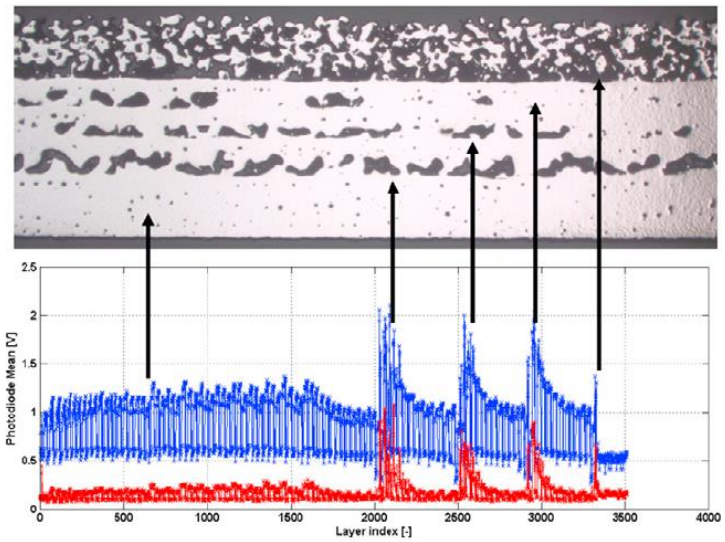

Figure 24:Cross-sectional view (top) and photo diode signal blue with standard deviation in red (bottom) (Berumen et al., 2010)

Spatter can also give information about the LPBF process (Repossini *et al.*, 2017; Ye *et al.*, 2019; Zhang *et al.*, 2019a). Repossini *et al.* (2017) used an optical monitoring system to obtain information from the spatter to characterize quality in LPBF. The experiment was done using a Renishaw AM250 and 18Ni (300) maraging steel They showed that doubling the optimal

scanning speed generates the same amount of spatter with comparable spread and smaller average area, whereas decreasing scanning speed by 33% led to more spatter with greater spread but with a smaller average area. It is reported that the bright area beyond the melt pool indicates a hot spot or laser-heated zone (LHZ). This is shown in black in Figure 25. This area increases with energy density. It is interesting to note that this approach can be coupled with other methods and is useful for additional process information.

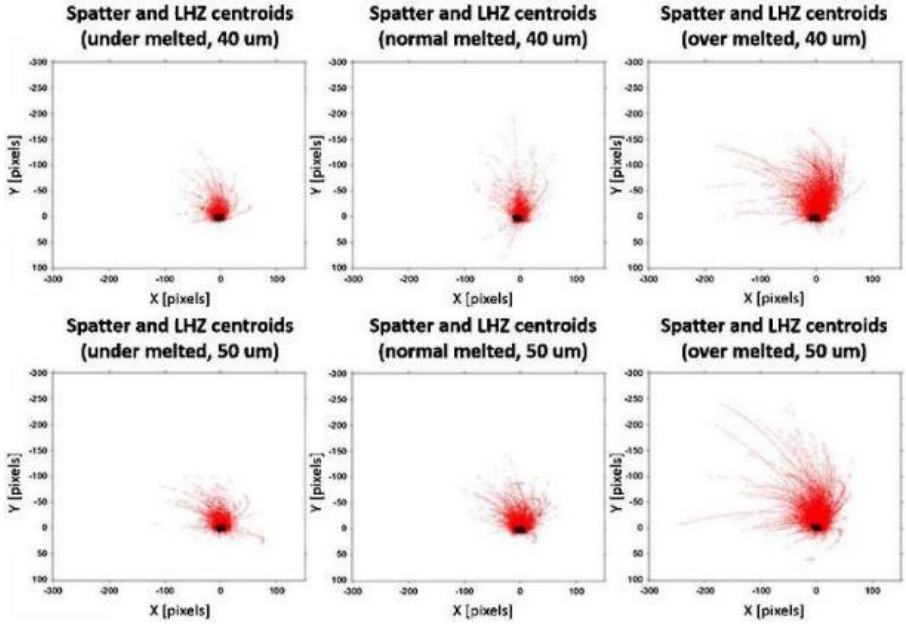

Figure 25: Superimposition of the centroid of every connected component classified as spatter (red) or laser-heated zone (black) (Repossini et al.,2017)

2.3.4. Summary

For LPBF, the development of different technologies for quality controls and standards are underway. The spatial and temporal resolution of in-process monitoring with feedback depends on scanning parameters. LPBF is a rapid process that makes online monitoring and feedback control extremely difficult. Not all forms of irregularities or instabilities are necessarily detectable by cameras which provides a motivation for additional (possibly complimentary) in-situ monitoring tools, such as AE.

2.4 Acoustic methods in non-destructive testing and monitoring

2.4.1. Introduction

Sound is a physical phenomenon which we can observe and study. Sound is a vibrating wave that travels through a transmission medium (solid, liquid or gas). Four of the common sources

of sound are: vibrating bodies, changing airflow, time-dependent heat sources and supersonic flow. Noise is referred to as unwanted sound and depending on the situation. In general it can come from various sources like the weather or more specific in this case machine components (Rossing *et al.*, 2001). To understand the application to this study, three main areas are identified: sound physics, data acquisition and signal analysis. The physics of the sound, as the name implies, entails the physical nature of sound. To acquire accurate data, equipment and signal sampling need to be implemented correctly. Lastly, the signal would be analyzed using mathematical operation, which is known as signal processing.

2.4.2 Theory of sound

Psychoacoustical terms such as “loudness perception” and “volume” should not be confused with the actual physical amplitude of a sound wave. Apart from the psychoacoustical terms, in literature there are often misconceptions about some of the terms used for sound measurement, and it is also to be expected when looking at the different fields in which sound measurements are used. Literature on sound measurement varies from do-it-yourself car audio books to music recording to in-depth physics of sound particle motion. Sound measurement can be divided into two quantities; sound energy - and sound field quantity. These can be seen as the cause and effect. Sound pressure and sound power – effect and cause.

Each person will interprete sound differently. The human hearing varies in sensitivity to levels of loudness at different frequencies, as shown in Figure 26. The apparent loudness level perceived by the average human is defined by the phon. It can be seen that at a frequency of 1 kHz, the apparent loudness perceived is equal to the actual sound pressure level (SPL = Phon). A great benefit of human hearing is that two ears greatly enhance 3D localization (stereo). For physical measurements, sound pressure level (SPL) and intensity are of importance (Errede, 2017; Rossing *et al.*, 2001; Sengpielaudio, 2019). These quantities are summarized in Table 4. The sound pressure is a measure of the actual pressure in pascal (Pa) and sound intensity is a measure of power (W/m^2). The units of measuring sound are calculated in (dB), a bel is simply a logarithmic ratio and the deci indicates that the unit is one tenth of one bel. The sound level is always calculated with a ratio of the root mean square value to a reference value (Sengpielaudio, 2019).

Table 4: Sound quantities and relationship

	Sound field quantities		Sound energy quantities	
	Sound pressure(p)	Pa	Acoustic intensity(I)	W/m^2
	Particle velocity(v)	m/s	Acoustic power	W
	Particle displacement	m	Sound energy (W)	J
			Sound energy density (E)	J/m^3
Relationship	$I \approx p^2$			
Level	$SPL = 10Log_{10}\left(\frac{{p_{RMS}}^2}{{p_{ref}}^2}\right)dB$		$SIL = 10Log_{10}\left(\frac{I_{RMS}}{I_0}\right)dB$	
Reference value (0 dB)	2×10^{-5} Pa		10^{-12} W/m^2	
Inverse distance law	1/r		$1/r^2$	

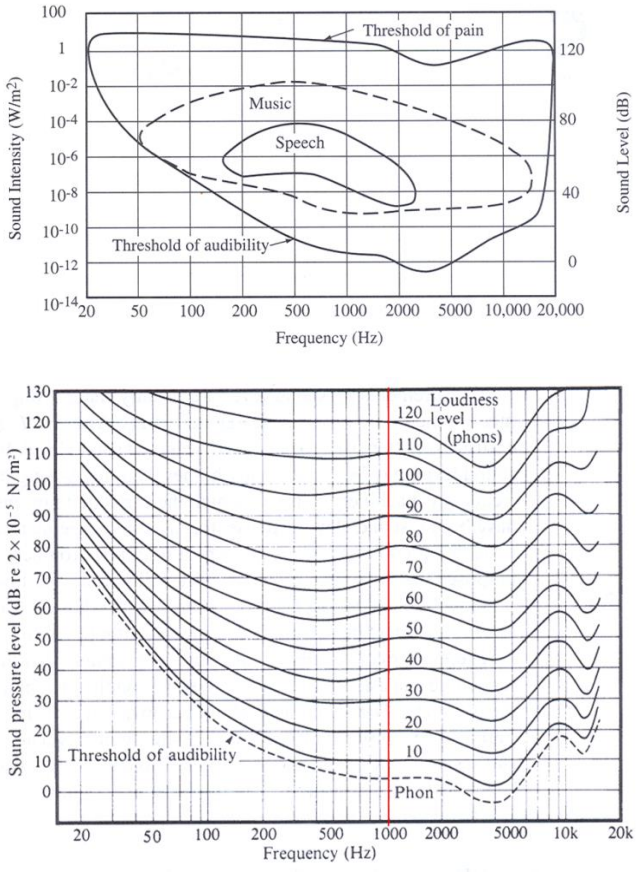

Figure 26: Band of human hearing (top) and apparent loudness for human hearing (bottom) (Rossing et al., 2001)

In a substance, particles oscillate without migrating, transferring energy to the adjacent particles and so the wave travels through a material. Sound waves are generally transmitted via longitudinal waves. The particles are only displaced in a local area, moving back and forth as

they experience high and low pressure (compression and rarefaction) (Alton and Everest, 2009; Hellier, 2012; NDT Resource Centre, 2020; Russell, 2019).

For an ideal gas, the speed of sound can be calculated by:

$$v_g = \sqrt{\gamma RT}$$

where: v_g is velocity of sound in gas; γ is the heat capacity ratio; R is the gas constant; T is the absolute temperature.

It can be seen that for an ideal gas the speed of sound is independent of atmospheric pressure. Velocity of sound is a measure of how fast energy can move through a material. Particle velocity increases with the pressure of the sound. This makes sense because the rate of change of a sine wave at a set frequency will increase with amplitude. (Alton and Everest, 2009; Rossing *et al.*, 2001).

Loss of sound energy can be due to absorption, beam spread, scatter, diffraction and interference. The combined effect of scatter and absorption is known as attenuation. The amplitude change of a decaying plane wave could be calculated by

$$A = A_0 e^{-\alpha z}$$

Where A_0 is an amplitude at a location; A is an amplitude of the wave at a distance Z away from A_0; α is an attenuation coefficient of the material.

It is very difficult to visualize how sound waves move in three dimensions. At best, one can imagine one sound wave travelling from a single source emitting hemispherical waves, but as soon as other sources and frequencies are present, complex interaction due superposition occurs. Single sound sources, such as shown in Figure 27, can generate interesting directivity patterns. The inverse square law and constructive/destructive interference of sound from different sources can alter the recorded data (Alton and Everest, 2009; Rossing *et al.*, 2001).

The shift in frequency and wavelength due to the Doppler effect given by:

$$f_p = f_s \frac{v_g}{v_g - v_s}$$

Where: f_p is a perceived frequency, f_s is a frequency of source, v_g is a velocity of sound in gas, v_s is a velocity of source.

The Doppler effect causes an increase in pitch when the source is moving towards the observer and decreases when the source is moving away.

When a sound wave travelling in medium encounters a boundary, the energy will be reflected and some energy transmitted. The amount of each depends on the material properties and more specifically the acoustic impedance (Z).

The acoustic impedance is dependent on the material density and velocity of sound, as shown below:

$$Z = \rho \times V$$

The ratio of the percentage reflected energy can be calculated by

$$Reflected\ energy = \left(\frac{Z_1 - Z_2}{Z_1 + Z_2}\right)^2$$

Where: Z_1 is an acoustic impedance in medium 1; Z_2 is an acoustic impedance in medium 2. The energy reflected between a steel-to-air interface is at ~100%, while a steel-to-water interface is ~88% (Hellier, 2012).

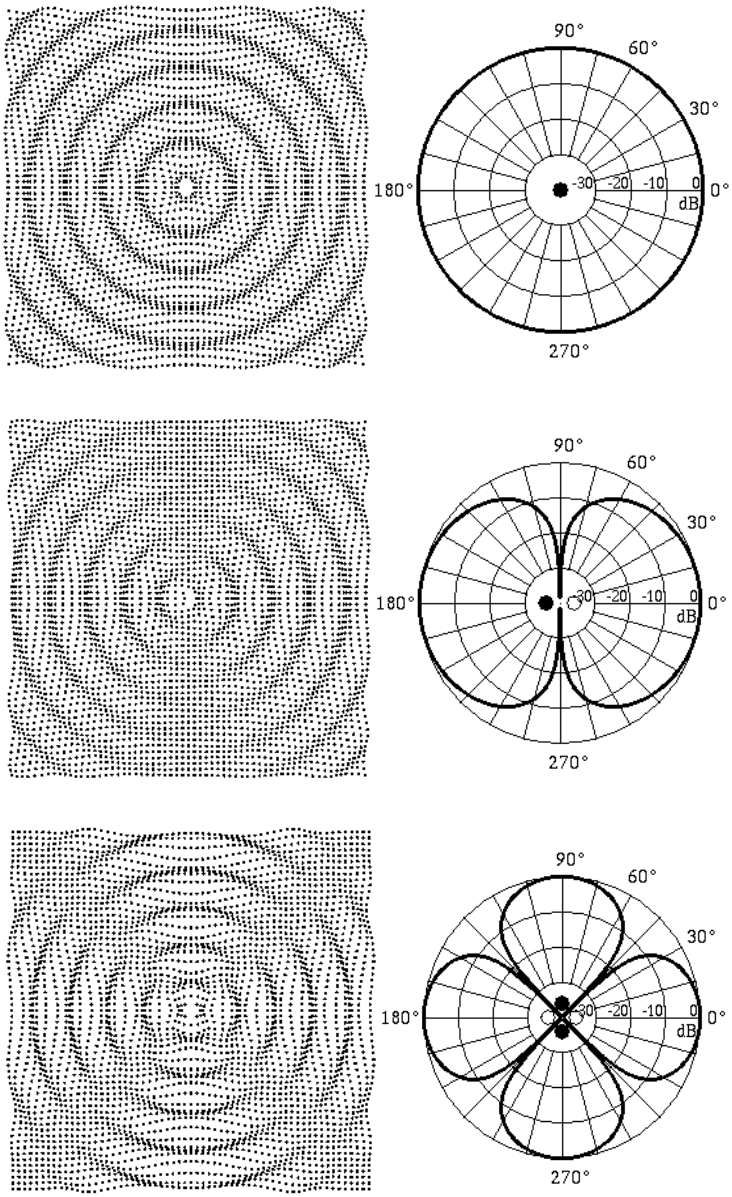

Figure 27: Sound fields of simple sources. Radiation from a monopole, e.g. boxed loudspeaker (top), Radiation from a dipole, e.g. loudspeaker (middle), Radiation from a lateral quadrupole, two identical dipoles a distance apart with opposite phase (bottom) (Russell, 2019)

Sound reflection can also be focused with curved surfaces. When a point source radiates sound against a rigid surface, the reflections returning can be represented as an imaginary source coming from beyond the surface. This imaginary source is referred to as an image, as shown in Figure 28.

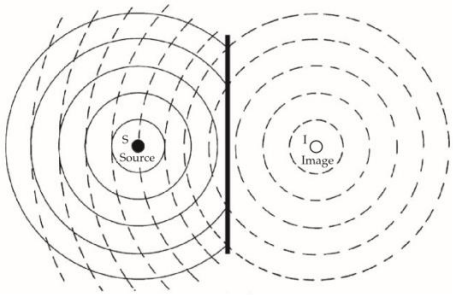

Figure 28: Sound radiated from a point source and reflected by a rigid surface (Alton and Everest, 2009)

If there is more than one wall from which the sound can reflect, multiple reflections would be created. For example, consider a source between parallel walls as shown in Figure 29: the reflection from the left will reflect off the right wall creating a new image from the right-hand side and continue to reflect on each side. The wall can be ignored and by using the images as virtual source one can model the effects.

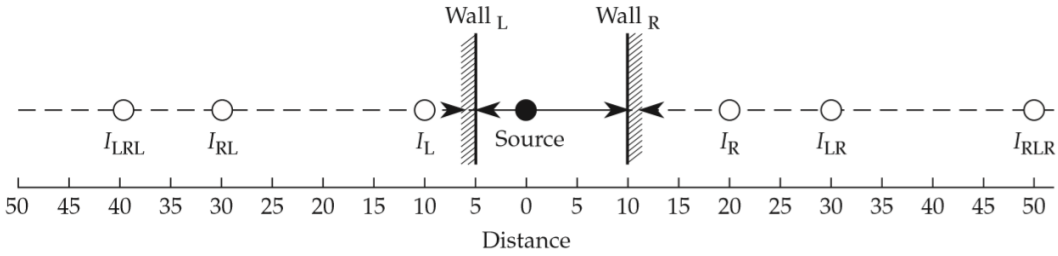

Figure 29: Reflection between parallel walls creating multiple imaginary sources (Alton and Everest, 2009)

In a rectangular room, complex sound fields would exist due to the six reflection surfaces. Surfaces can reflect sound in various ways. Plane sound waves will be dispersed through a wide angle if they strike a convex surface. Similarly, plane sound waves can be focused using a concave surface. A room will reflect at the corners, the sound will propagate back in the direction of the source, as shown in Figure 30. This is known as a corner reflector. Therefore, in most rooms the inverse square law no longer applies due to reflections and the location of the measurement.

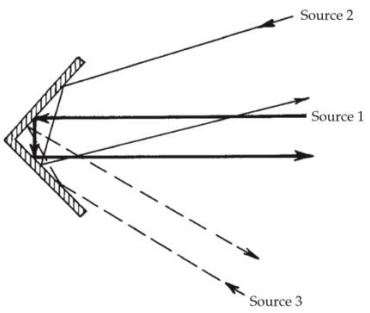

Figure 30: Sound reflecting to the source from a corner reflector (Alton and Everest, 2009)

A sound wave will bend/diffract when it meets an obstacle; like light it will bend around the obstacle (Figure 31). The amount of bending is dependent on the wavelength.

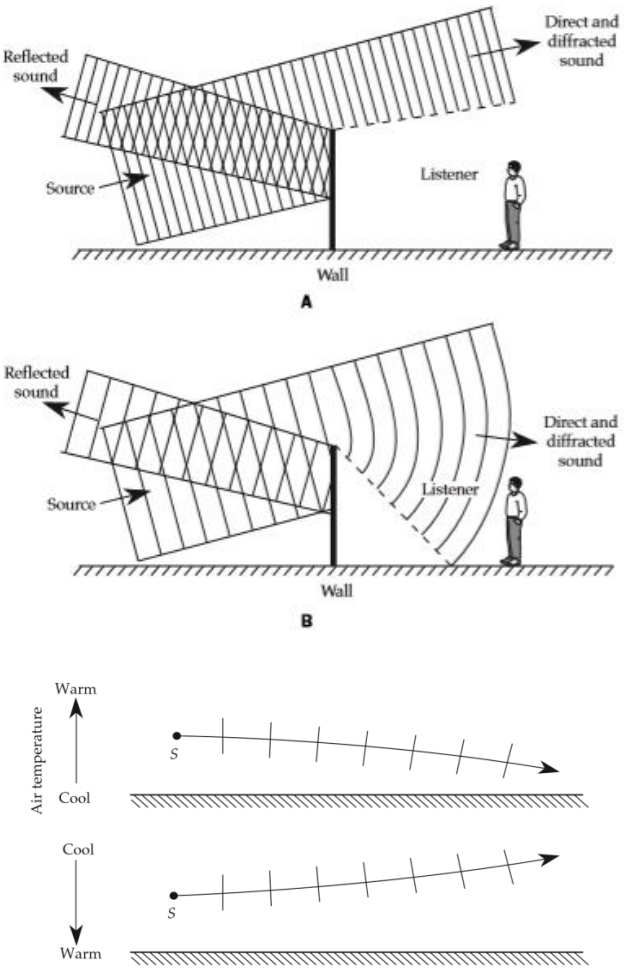

Figure 31: Diffraction (top) and refraction of sound waves (bottom). A traffic barrier (high frequencies with limited diffraction (A) and low frequencies being observed by the listener due to the high angle of refraction of lower frequencies). The change in direction of sound is due to the speed of sound that changes with hot and cool air. (Alton and Everest, 2009)

The average distance the sound travels between reflections; Mean Free Path (*MFP*) is given by

$$MFP = \frac{4V}{S}$$

The time it takes for the reflections to die out is known as reverberation time. An estimation of the time for the reflections in a room to be at a value of 60 dB below its original is given by the Sabine equation

$$RT_{60} = \frac{55.25V}{v_g S\overline{\alpha}}$$

Where:

V is a volume of the space, v_g = velocity of sound in gas; S is a surface area of the space; The average absorption ($\overline{\alpha}$) coefficient is then given by

$$\overline{\alpha} = \frac{s_1\alpha_1 + s_2\alpha_2 + \cdots + s_n\alpha_n}{s}$$

Where:

s_n is the surface area of the wall and α_n is the corresponding absorption coefficient.

The inverse distance law shows the relationship between the level of sound and the distance away from the source (Figure 32).

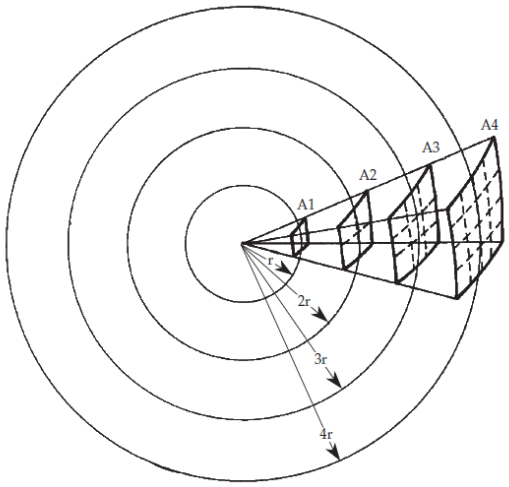

Figure 32: Sound propagating in a free field spreading out as the distance increases (Alton and Everest, 2009)

In a free field, sound travels in a straight line without disturbances such as reflections, etc. in enclosed spaces. However, sound is subjected to reflections from surfaces which affect the way in which the sound travels and the inverse square law does not describe the entire sound field.

The sound in the space will have a combination of direct and reflected sound (Figure 33 – note the transition at the critical distance). The distance from the source can be divided into different regions which define the direct and reverberant sound and the combination thereof. Very close to the source, the sound intensity will be much stronger compared to the reflections. Beyond the critical distance, the sound field will even out as a function of the surrounding and its absorption.

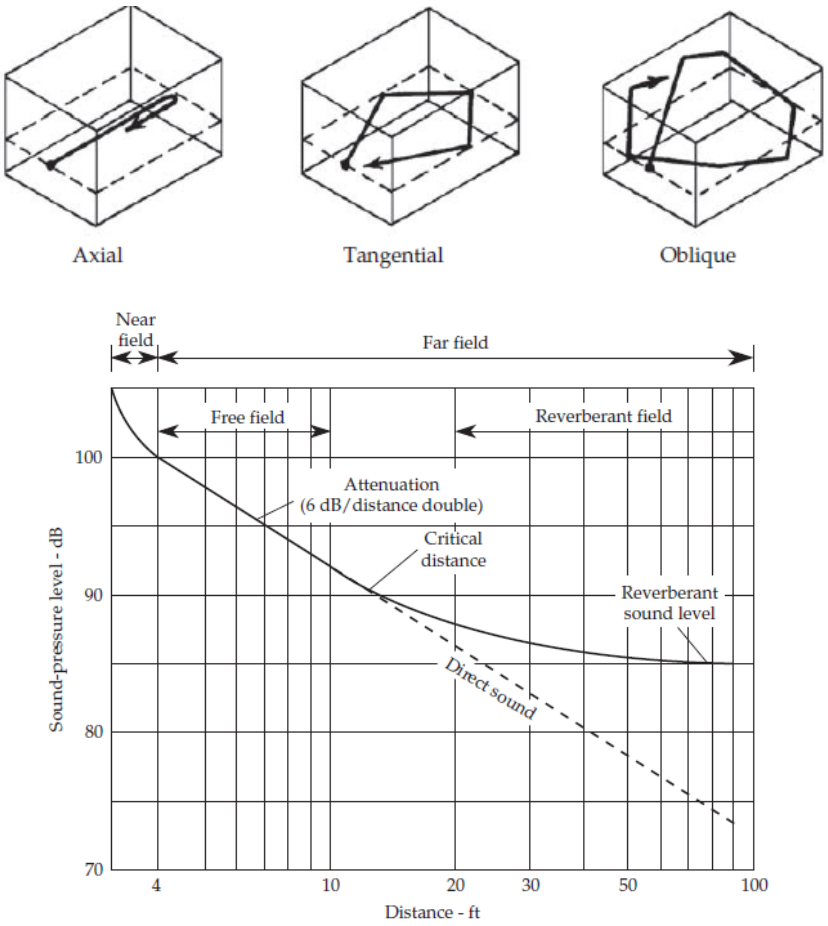

Figure 33: Axial, tangential, and oblique room modes (top). Enclosed sound field (bottom), (Alton and Everest, 2009).

The critical distance is calculated by

$$d_c = 0.057\sqrt{\frac{V}{RT_{60}}}$$

The sound pressure at a point in a closed space will vary not only due to direct and reflected sound, but also modal resonance within the space. A standing wave will be generated in the space as the wave travels back and forth between reflective surfaces. Resonance will also have different modes depending on the size of the space and the frequency. The resonance will be a combination of the axial, tangential and oblique modes. These resonances can be complex in nature as many different interactions exist between surfaces, these are usually only considered for frequencies below the crossover frequency, because above the crossover frequency mode spacing is so small and the frequency response is much smoother.

The modes can be calculated by the room mode calculation given by Rayleigh

$$f_{mode} = \frac{v}{2}\sqrt{(\frac{p}{L})^2 + (\frac{q}{W})^2 + (\frac{r}{H})^2}$$

Where:

L, *W*, *H* = length, width, and height

p, *q*, *r* = integers 0, 1, 2, 3, . . .

v = speed of sound

Since we are considering a small chamber, the crossover can be calculated by the Schroeder equation:

$$f_{cross\ over} = 2000\sqrt{\frac{RT_{60}}{V}}$$

2.4.3 AE data acquisition and signal processing

Signal processing is a field which is ever evolving and the mathematical possibilities are endless; therefore, this section barely scratches the surface, nevertheless, it will be useful to the reader. Time-domain signals represent the amplitude of the signal at a point in time during which it is sampled. In contrast, a signal can be expressed in terms of its individual frequency components and is known as the frequency-domain. The algorithms used to transform a signal from time to frequency domain are known as Discrete Fourier Transform (DFT), and an algorithm designed to speed up the computational time is called Fast Fourier Transform (FFT).

Signals in time-domain contain N number of samples that are sampled at a specific rate of fs. The sampling interval Δt can be calculated:

$$\Delta t = \frac{1}{f_s}$$

Where f_s is a sampling rate.

With a sample denoted by x[n], $0 \leq n \leq N-1$ the DFT is given by:

$$X_k = \sum_{n=0}^{N-1} x[n]\ e^{-j\frac{2\pi}{N}nk} \qquad for\ k = 0, 1, 2, \ldots, N-1$$

Since DFT and FFT are complex, they contain both amplitude and phase information. The phase information is relative to the start of the signal. Because both the time and frequency domain have N number of samples, the frequency resolution Δf of the DFT is given by:

$$\Delta f = \frac{f_s}{N} = \frac{1}{N\Delta t}$$

The power of each frequency in a signal can be determined by squaring the magnitude of specific frequency $|X[k]|^2$ and the plot is called the power spectrum. This is useful in applications were phase information is not necessary, for example, to calculate power in harmonics of a signal.

According to the Nyquist theorem, the sampling rate(f_s) should be at least double that of the maximum frequency present in the signal. Under-sampling will make the signal appear to be at a lower frequency; this phenomenon is known as aliasing. The effect of aliasing is shown in Figure 34 below.

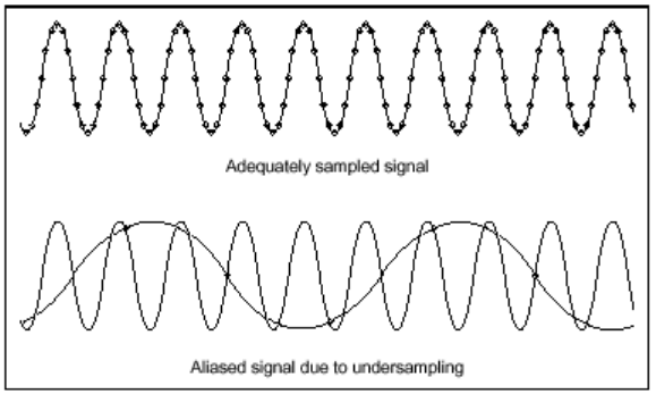

Figure 34: Effect of sampling rate on signal (Cerna and Harvey, 2000)

To prevent aliasing before measurement, an antialiasing filter can be used. An antialiasing filter will make all frequencies above the Nyquist smaller depending on the frequency response of the filter, i.e. bandwidth (frequency range) and attenuation of each frequency.

Signal-to-noise ratio (SNR) refers to the ratio between the signal and the power and can be described by:

$$\frac{average\ signal\ power}{average\ noise\ power} = \frac{S}{N} = SNR_{Power}$$

SNR can be defined in several different ways. The SNR ratio in terms of voltage is proportional to the square root of the power and is given by:

$$SNR_{dB} = 20\ log \frac{V_{rms}\ signal}{V_{rms}\ noise}$$

An analysis method for AE could be a Short Time Fourier Transform (STFT). STFT is used to obtain time-frequency analysis of data signals. STFT calculates the energy distribution in the joint time-frequency domain. STFT is accomplished by calculating the Fast Fourier Transform (FFT) of the signal in a sliding window. This window is moved across the signal to give a representation of the frequency content at that specific portion in time (National Instruments Corporation, 2012; Cerna and Harvey, 2000; École Polytechnique Fédérale de Lausanne, 2018).

2.4.4 Online monitoring by AE in material processing

Online monitoring using AE is a versatile method as it can be developed and applied in various forms for each specific need. AE can be divided into gas- and structure-borne emission originating from the stress waves induced by changes in the internal structure of the part being processed. Various methods have been developed for specific applications and it is no different for the AM industry. For structure-borne AE, the contact installation of transducers is necessary, whereas with air-borne emission inspection it is quite difficult to isolate noise to acquire a useful signal (Shao and Yan, 2005). For structural monitoring, qualitative types of AE signals are burst (discrete) and continuous. “Burst” signals are especially useful for detection of delamination and crack initiation under deformation. Acoustic signals from diffusive phase transformations or coalescence of microcracks can be classified as continuous signals (Lu and Wong, 2018; Kuba abd Aken, 2013; Shi et.al., 1999). AE in materials that undergo deformations and fractures depends on physical properties of material as well as environmental factors (Al-Obaidi *et al.* 2012; Muravin, 2009).

The environment and type of machinery being used can influence the results and determine the method used to record data. The method is especially important with respect to other sources of acoustic noise. Yusof *et al.* (2017) investigated the feasibility of using acoustic monitoring of pulse-mode laser welding to indicate the depth-of-penetration. One of the conclusions drawn is that post-processing is needed to eliminate the influence of noise. Horvat *et al.* (2011) proposed a new algorithm that eliminates reverberation and background noise during AE monitoring of gas metal arc welding (GMAW). Similarly, Alfaro and Cayo (2012) showed that the quality of online AE monitoring was affected more by environmental conditions when compared to online infrared monitoring during GMAW. Thus, factors like the effect of sound

reflections, machine environment, noise and the location of the recording device need to be considered as a basis of qualification.

AE has been used with great success in laser welding and cutting (Clough, 1987; Duley and Mao, 1994; Gu and Duley, 1994; Gu and Duley, 1999; Li and Steen, 1992; Nakamura *et al.*, 2000; Ortega *et al.*, 2015; Schiry *et al.*, 2016; Stepanova *et al.*, 2019; Yusof *et al.*, 2017).

For quality control of the ever-growing laser technology implemented in industrial applications, Mao *et al.* (1993) suggest the use of AE as it has high signal-to-noise ratio, fast response, and no contact is needed. It was shown that the acoustic spectrum of conduction welding is different to that of keyhole welding and there is strong correlation between AE energy signal and laser power, welding speed and focusing distance (laser spot size). This study aimed at using a microphone, i.e. gas-borne AE, compared to others which used an ultrasonic transducer (Figure 35). A photo diode was used to compare the optical data. The data was then processed using real time FFT (Mao *et al.*, 1993).

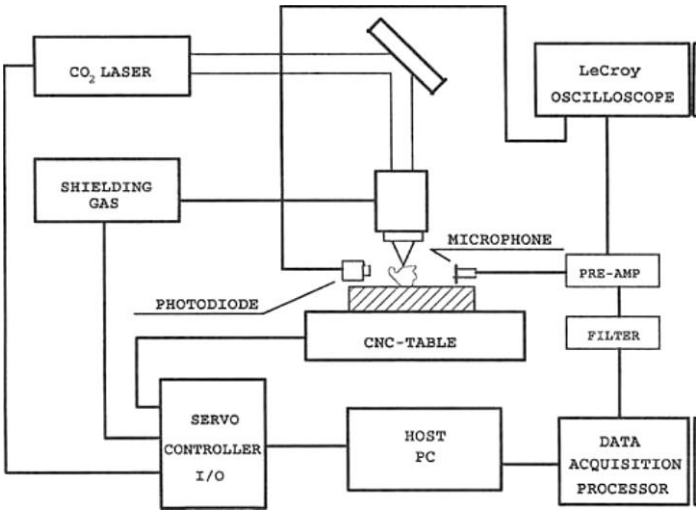

Figure 35: Schematic of AE monitoring system during laser welding, Mao et al. (1993)

Although clear differences were shown in the AE results of Mao *et al.* (1993), tests were carried out inconsistently by changing too many process parameters at once, thereby making it difficult to make good comparisons. One test which is comparable did show a clear difference between different welding regimes; a 2 mm aluminium plate welded at different laser powers produced conduction and keyhole regimes. In the AE data shown in Figure 36, a clear peak at 7 kHz is observed during keyhole mode compared to conduction-mode welding. It was concluded that differences were due to the presence of fluctuations in plasma.

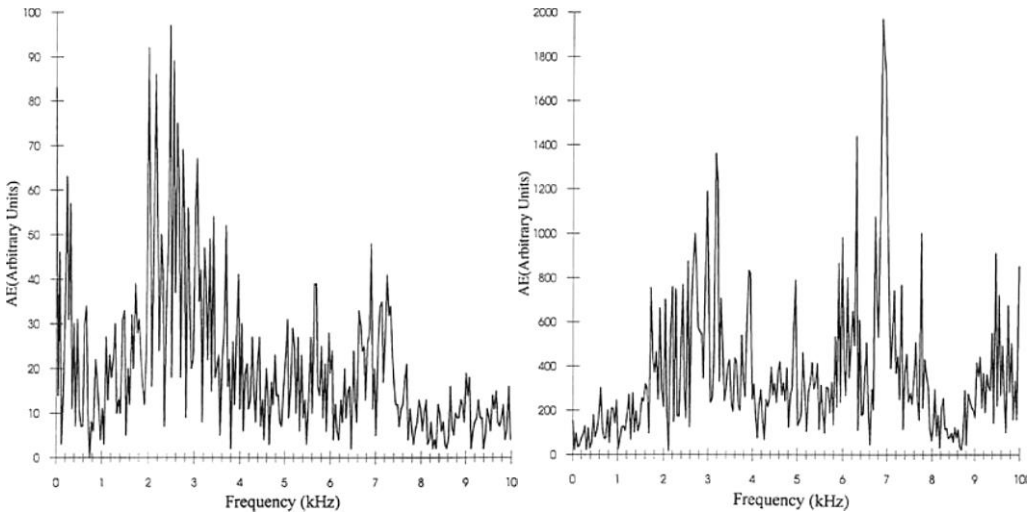

Figure 36: AE spectrum in CO2 laser welding of aluminium at 1 kW at 1 524 mm/s causing conduction mode (left) and AE spectrum at 1.6 kW at 1 524 mm/s causing keyhole mode (right) (Mao et al., 1993)

Leaks and frictions, *i.e.* interactions of media in relative motion, chemical reactions and changes of size of magnetic domains also generate acoustic waves and create other classes of AE signals that can be studied for quality control of tooling and manufacturing. Charde *et al.* (2016) interpreted weld formation using AE from carbon and stainless steel welds using servo-based resistance spot welding. Typical acoustic behaviour was found for amplitude of frequencies and corresponding phase shifts for "ideal" and expulsion welding conditions. It was found that different AE patterns were used to distinguish the behaviour of ideal and fault welding processes that were qualified using macrographs. Similar results were received for laser welding of Al and polyamide sheets by Schiry *et al.* (2016). A rough joint was a result of excessive energy input. Gas bubbles provoked creation of the gas channels registered by hits-time from AE monitoring during the process. Higher hits in the area of the gas channels correlated with the appearance of the holes in welding. With decreased energy input, a weak joint with low tensile strength was created and the corresponding AE signal was irregular showing wide scatter. Also, it was shown that the distance from the weld spot to the sensor has a strong influence on the signal strength.

Air-coupled ultrasound is a non-contact inspection method that transmits ultrasonic waves through the air and into the part being inspected. It is commonly used for composite materials because for steel low acoustic impedance and weak transmission between steel-air barrier make it difficult to transmit the waves. With technology development air-coupled ultrasound is becoming more popular in steel industries such as welding. Abbasi et al. (2018) used air-coupled ultrasound to correlate various GMAW defects and microstructures to the ultrasonic features. A study by Luo *et al.* (2019) investigated the effect of the plasma plume during pulsed-

laser welding on the structure-borne AE. The YAG (4.5kw, 1 060 nm and 6 ms pulse width) laser was defocused to produce different plasma plumes. The AE of these different plumes were compared and shown to have valuable information. They showed that each pulse has a certain AE development corresponding to the plasma plume, as shown in Figure 37a, and high-speed images of the plume during different times of the pulse are compared in Figure 37b. This difference in amplitude was due to increased laser absorption.

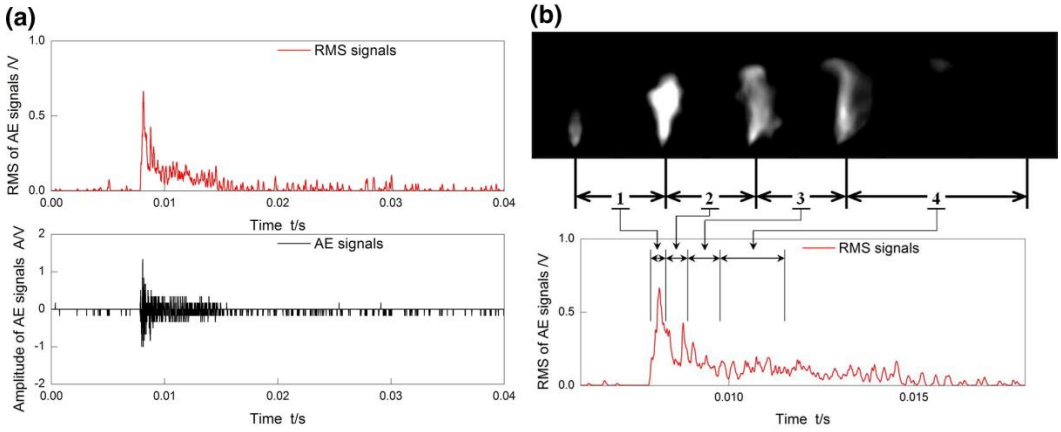

Figure 37: Relationship between plasma and the structure-borne AE of 6 ms pulsed laser. RMS and actual signal (A) and development of plume during the pulse (B) (Luo et al., 2019)

This evolution of the AE signal over time (Figure 37) gives rise to many concerns during AE monitoring as the LPBF process consists of consecutive single tracks which starts and stops according to the laser modulation. The start-stop nature can cause unwanted resonances to appear in the frequency measurements.

In laser welding, AE arises in response to oscillations in the keyhole and to the expansion of vapour as it leaves the keyhole. The frequency may include components as high as several hundred kHz (Li and Steen, 1992; Gu and Duley, 1999) because resonances within the keyhole work in the same way as an organ pipe. It was found that the frequency response is correlated with the welding quality, i.e. keyhole formation, plasma formation, and crack propagation. Laser ablation and AE of the plasmas were studied by Planco and Laserna, (2003) where it was shown that spectral analysis of acoustic waves is a reliable technique for diagnosing the laser plasma phenomena. The sound level during laser welding has not been shown to be a strong predictor of weld quality when compared to the spectral information (Spears and Gold, 2016).

An in-process non-contact method for quality control can be realized using AE as it is seen to have high signal-to-noise ratio and fast response. This non-contact method can be used for quality control of the ever-growing laser technology implemented in industrial applications.

2.4.5 Acoustic emission in AM

AE was mentioned in reviews of non-destructive and in-situ monitoring methods for AM (Lu and Wong, 2018, Lu and Wong, 2017; Wu *et al.*, 2016, Wu *et al.*, 2019). AE signatures as a function of various process parameters during metal AM were studied by Fisher *et al.*, 2016; Gaja and Liou, 2017; Koester *et al.*, 2018; Taheri *et al.*, 2019; Wasmer *et al.*, 2018. Fisher *et al.*, (2016) showed measurable and repeatable differences in the acoustic signatures of the LPBF process as a function of laser power. Wasmer *et al.* (2018) found correlation of AE data from a fibre Bragg grating acoustic sensor and porosity of samples manufactured at different scanning speeds. Gaja and Liou (2017), Koester *et al.* (2018) and Taheri *et al.* (2019) recorded AE signals during a laser deposition process and found correlation between AE events, various process conditions and defects. AE has also been applied with success to the crack monitoring in fatigue tests of additively manufactured titanium which also illustrates the sensitivity to crack detection by the technique (Strantza *et al.*, 2017). A non-contact acoustic in-situ monitoring method for AM was recently patented by General Electric (Gold and Spears, 2018; Redding *et al.*, 2017) and Renishaw (Hall, 2016). In Redding *et al.*, 2017, the AE acoustic sensors may be arranged to detect acoustic signal previously received from a reference defect-free part (confirmed by other methods) and then compared to real-time data of the printed part. It is alleged that sudden deviations in the amplitude of acoustic signals indicated a fault in the process.

AE holds promise as a simple, low-cost process monitoring tool, however, AE in-situ monitoring devices are not yet commercially available for AM. In an LPBF process, a simple microphone was used to monitor the process signature (Ye *et al.*, 2017). Machine-learning methods were employed to find process signals correlating to irregular track formation and porosity formation, due to balling and overheating, and showed great promise for the method (Williams *et al.* 2018; Ye *et al.*, 2018). Under less severe conditions with smaller porosities, a similar approach was recently found to be successful, though using a more specialized microphone (fibre Bragg grating) (Shevchik *et al.*, 2018; Wasmer *et al.*, 2018, Wasmer *et al.*, 2019). A similar concept is under development and preliminary results were reported in Eschner *et al.*, 2018. The above methods combine machine learning with AE, with the aim to find irregular process signatures and potentially correct these, for example, by inducing a full remelting of a layer with defects. Recently the method was used to identify crystallographic textures, initially in an offline scenario, but potentially also deployable for in-situ process monitoring (Dryburgh *et al.*, 2019). The detection of artificial cavities of only 0.2 mm in size

has recently been demonstrated using laser-induced phased arrays, although the response is not equal throughout the volume (Pieris *et al.*, 2020).

Another structure-borne AE study by Lawrence Livermore National Laboratory showed that a notable difference could be obtained from the acoustic signatures of varying laser powers. They used an experimental test bed to carry out experiments. Two different sets of laser power were chosen, 150 W and 600 W, with a 50 μm powder layer of steel powder (ASME318) and a scanning speed of 250 mm/s, 50 of 12 mm tracks were produced at each laser power with a hatching distance of 200 μm. A 10 MHz sensor was placed on the bottom of the test bed, i.e. structure-borne AE was measured. It was found that there was a clear shift and missing peaks in spectral analysis at different laser powers, as shown in Figure 38. Authors have shown that the quality of AE results is dependent on noise and found these results were repeatable (Fisher *et al.*, 2016).

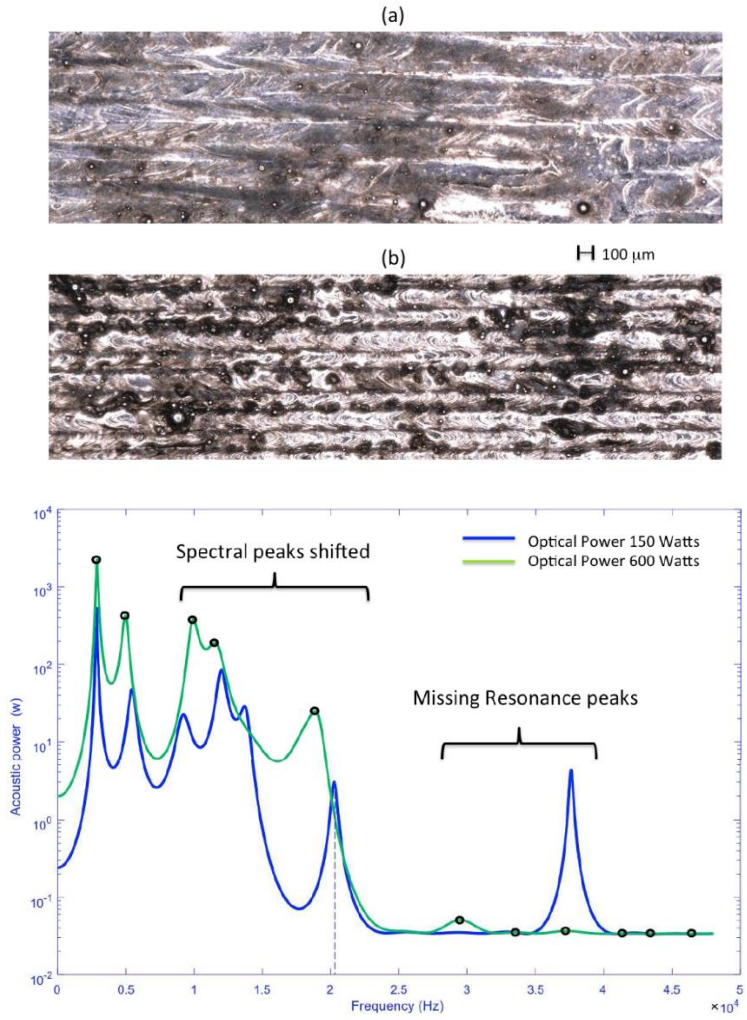

Figure 38: UT acoustic spectra of two different layers during LPBF of ASME 318 steel at different laser powers (bottom) and their microscopic images of the top views (a) 600 W and (b) 150 W (Fisher et al., 2016)

Ultrasonic monitoring was also investigated in terms of an online monitoring system for metal AM. Rieder *et al.* (2014) specifically set out to investigate the use of UT monitoring as an additional information source to the already available optical monitoring system. An ultrasonic transducer was fitted at the bottom of the substrate, as shown in Figure 39. An unfocused 10 MHz ultrasonic probe was glued to the building platform.

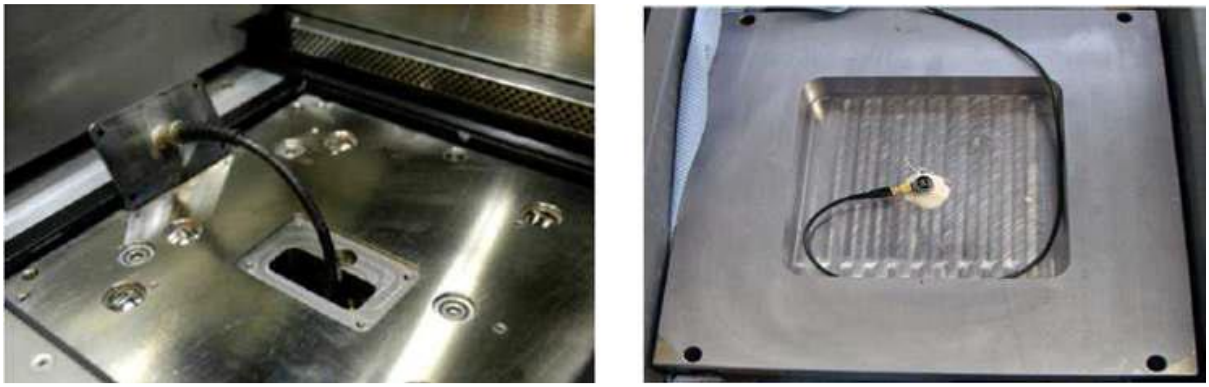

Figure 39: Ultrasonic probe installation in an EOS M270 machine build platform (Rieder et al., 2014)

Their system allowed for a temporal resolution of 4 ns. A scan plot after each layer gave a back-wall echo (BE) representing the top surface of the component. The interference echo (IE) is due to the signal travelling from the base plate to the substrate, as shown in Figure 40.

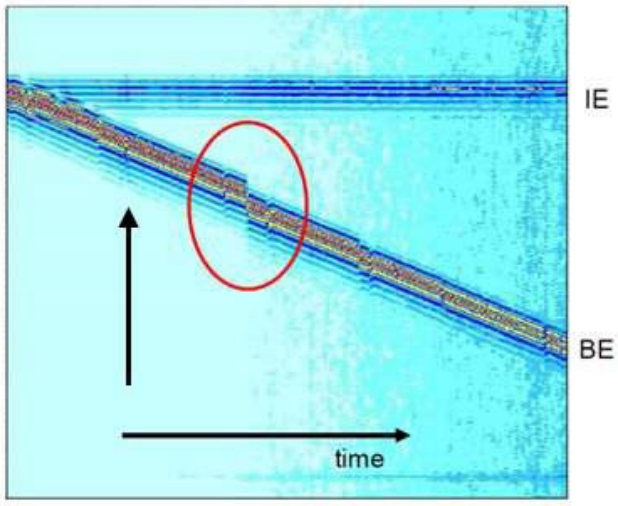

Figure 40: Interference echo and back-wall echo used for build height UT monitoring (Rieder et al., 2014)

Rieder *et al.* (2014) concludes that many possibilities are feasible and that more investigations need to be carried out. Possible identifications that could be identified using UT monitoring include surface dynamics, qualitative residual stress evaluation and porosity identification. It is also noted that these results hold true for non-complex geometries.

Slotwinski *et al.* (2014) investigated the possibility of creating a UT sensor for in-situ monitoring of porosity formation during LPBF of cobalt-chrome (CoCr) with the hope that this would possibly lead to process validation and real-time adjustments to the parameters. An ultrasonic transducer was situated within the substrate facing upwards. Ultrasonic pulse-echo technique was applied to measure the speed of sound within the material. The speed should vary with a change in porosity within the material. The results showed a linear correlation between the percentage porosity (measured using X-ray CT) and the wave speed, as seen in Figure 41. Although the speed of sound shows correlation with the porosity, at low porosity values there seems to be no definite correlation and the higher values are so high that the part would have been building a part with porosity for more than a few layers, therefore, it cannot really be consider an online monitoring system.

For other AM technologies, Wu *et al.* (2016) applied AE to fused deposition modelling (FDM) for online monitoring; an AE sensor was placed on the filament extruder. The relationship between the sound emitted at certain machine operating conditions enables recognition of five different extruder operating conditions. In a similar application, Whiting *et al.* (2018) studied the application of AE during laser-engineered net shaping (LENS) as a process monitoring system in which the powder flow through the nozzle was measured with AE (Figure 42).

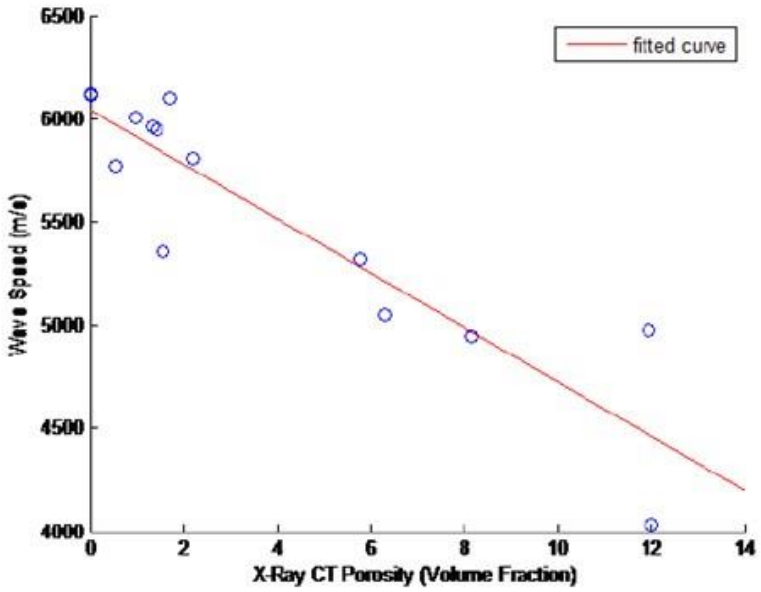

Figure 41: Porosity vs. wave speed (Slotwinski et al., 2014)

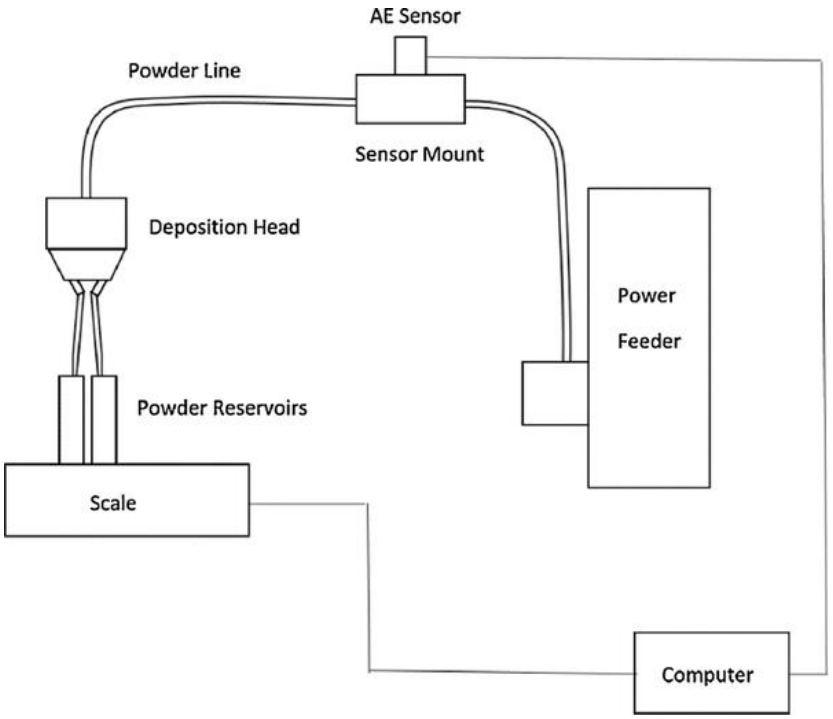

Figure 42: AE system for powder flow rate measurements during LENS (Whiting et al., 2018)

2.4.6 Summary

Online monitoring is the focus of many research institutions as the need from industry has been put forward. Research shows that AE can be a promising tool for online monitoring as the frequency and amplitude change at different AM process parameters. In contrast to the use of digital signal processing, the implementation of AE with machine learning has lately been receiving much interest. Many different AE approaches and sensor types have been implemented in AM. When considering the spatial and temporal resolution of imaging monitoring methods compared to AE: AE can obtain a high temporal resolution with relatively inexpensive data acquisition hardware. Imaging systems have high spatial resolution and depending on the optical setup can typically be in the range of 100 µm, whereas the spatial resolution in gas-borne AE is non-existent for a single microphone setup. A more complex setup known as a microphone array can be used to pinpoint the origin of the sound based on difference in time-of-flight. It is shown that AE monitoring during LPBF is able detect residual stress, cracks, porosity, changes in laser power and scanning speed. Although research has shown that a microphone can be used for online monitoring during laser welding, the use of a microphone to monitor LPBF has many possibilities. Some possible features of gas borne AE that can be taken advantage of are:

- the sensor does not need to be attached to the substrate;

- the sensor is not very sensitive to position;
- it can record other events such as recoating and gas flow;
- it needs minimal hardware adjustments and easy installation;
- it is inexpensive equipment;
- it has good temporal resolution (compared to imaging devices);
- it has a small data size.

Since many LPBF defects originate from powder delivery issues, this work will set out to determine whether there is a probability of detection using gas borne AE monitoring.

Chapter 3: MATERIALS AND METHODS

Firstly, preliminary tests investigating the critical powder layer thickness which causes lack-of-fusion porosity in 3D LPBF parts were conducted. Secondly, AE signals under different layer thicknesses and laser powers were studied for single track formation. Lastly, two methods were explored for defect recognition. The final algorithm can accurately identify three different powder layer thicknesses: no powder, reference (optimal) powder layer thickness and critical (thick) powder layer thickness.

3.1 EOSINT M280

All samples were manufactured from Ti6Al4V (ELI) powder using an EOSINT M280 LPBF machine (Figure 43). The M280 system's specification is shown in (Table 5).

Figure 43: EOSINT M280 machine

Table 5: The technical data for LPBF machine

Building volume	250 mm x 250 mm x 325 mm
Laser type	Yb-fibre laser, 400 W
Laser	1 075 nm TEM00 Gaussian profile and 80 µm spot size
Precision optics	F-theta-lens, high-speed scanner
Scan speed	up to 7.0 m/s
Variable focus diameter	80–500 µm
Power supply	32 A
Power consumption	maximum 8.5 kW/typical 3.2 kW
Software	EOS RP Tools; EOSTATE Magics RP (Materialise)
CAD interface	STL. Optional: converter for all standard formats

3.2 Powder

Experiments were carried out on a Ti6Al4V extra-low interstitials (ELI) substrate in Ar protective atmosphere. Pre-alloyed gas-atomized powder Ti6Al4V ELI from TLS Technik GmbH & Co. Spezialpulver KG (Germany) was used. The equivalent diameters of the powder particles were d10 = 12.03 µm, d50 = 21.38 µm and d90 = 31.15 µm. Values of d10, d50, and d50 correspond to the 10%, 50%, and 90% of particles (weighted by volume) in the reported particle size. For the preliminary data for layer recognition, experiments were run parallel with other experiments that were aimed at obtaining an insight into the development of the single track and layer formation of in-situ alloying of Ti6Al4V-5 at .% Cu during LPBF. The Ti6Al4V (ELI) and Cu powders were spherical in shape and argon-atomized. Chemical composition of Ti6Al4V (ELI) was 89.26 wt% of Ti, 6.31 wt% of Al, 4.09 wt% of V, 0.12% of O, and Cu powder with 99.9 % purity. The 10th, 50th and 90th percentiles of equivalent diameter (weighted by volume) were 12.6 µm, 22.9 µm, 37.0 µm for Ti6Al4V (ELI) powder and 9.45 µm, 21.9 µm and 37.5 µm for Cu powder, respectively. The building chamber was filled with an inert (argon) atmosphere.

3.3 Laboratory equipment

3.3.1 Visual testing

Surface and cross-section analysis was done using a scanning electron microscope (SEM) and optical microscopes. Optical and SEM tests provide detailed, in-depth visual analyses of components. SEM was carried out with a NeoScope JCM 5000 (Figure 44), operated at 10–15 kV. The optical microscopes used were a Smartzoom 5 and a Scope A1, both from Zeiss.

(a) (b) (c)

Figure 44: SmartZoom5 (a) and Scope A1 (b) optical microscopes; NeoScope JCM 5000 scanning electron microscope (c)

For pore analysis and analysis of the cavities' sizes and shapes, samples were cut with an electrical discharge machine (EDM). The small templates were incorporated into MultiFast resin by CitoPress (Figure 45a). Samples were polished with a Tegramine-25 system (Figure 45b), as recommended by Taylor & Weidmann (2009), and etched with Kroll's reagent.

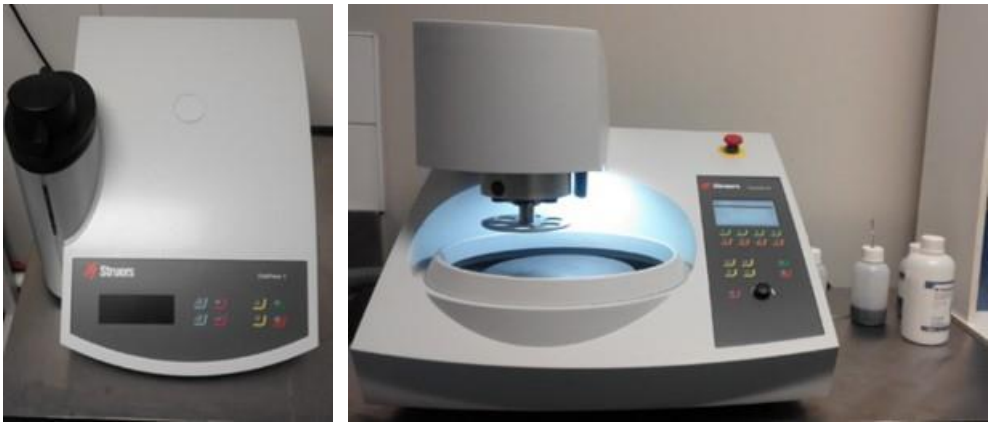

(a) (b)

Figure 45: CitoPress 1 (a) and polishing machine Tegramin-25 (b)

3.3.2 Microcomputed tomography

General Electric phoenix v|tome|x L240/NF180

X-ray microcomputed tomography (microCT) was used in this study (Figure 46). A General Electric phoenix v|tome|x L240/NF180 installed in the Central Analytical Facility at Stellenbosch University was used.

Figure 46: Phoenix v|tome|x L 240 X-ray CT scanner (top) (GE Oil & Gas, 2020) and personal photo (bottom)

X-ray settings were 150 kV and 150 µA with 2 000 images acquired in a full rotation at an image acquisition time of 500 ms per image, with averaging set to two images and one image skip per rotation. Detector shift was activated to minimize ring artefacts. Background calibration was performed, and the scan time was approximately 40 minutes per scan at 40 µm

voxel size. A 1 mm copper beam filter was used. Analysis was performed with Volume Graphics VGStudio Max 2.1.

3.4 AE data acquisition

AE signal analysis was performed by post-processing, compiled and implemented using systems engineering software LabView (National Instruments) and its signal processing algorithms library.

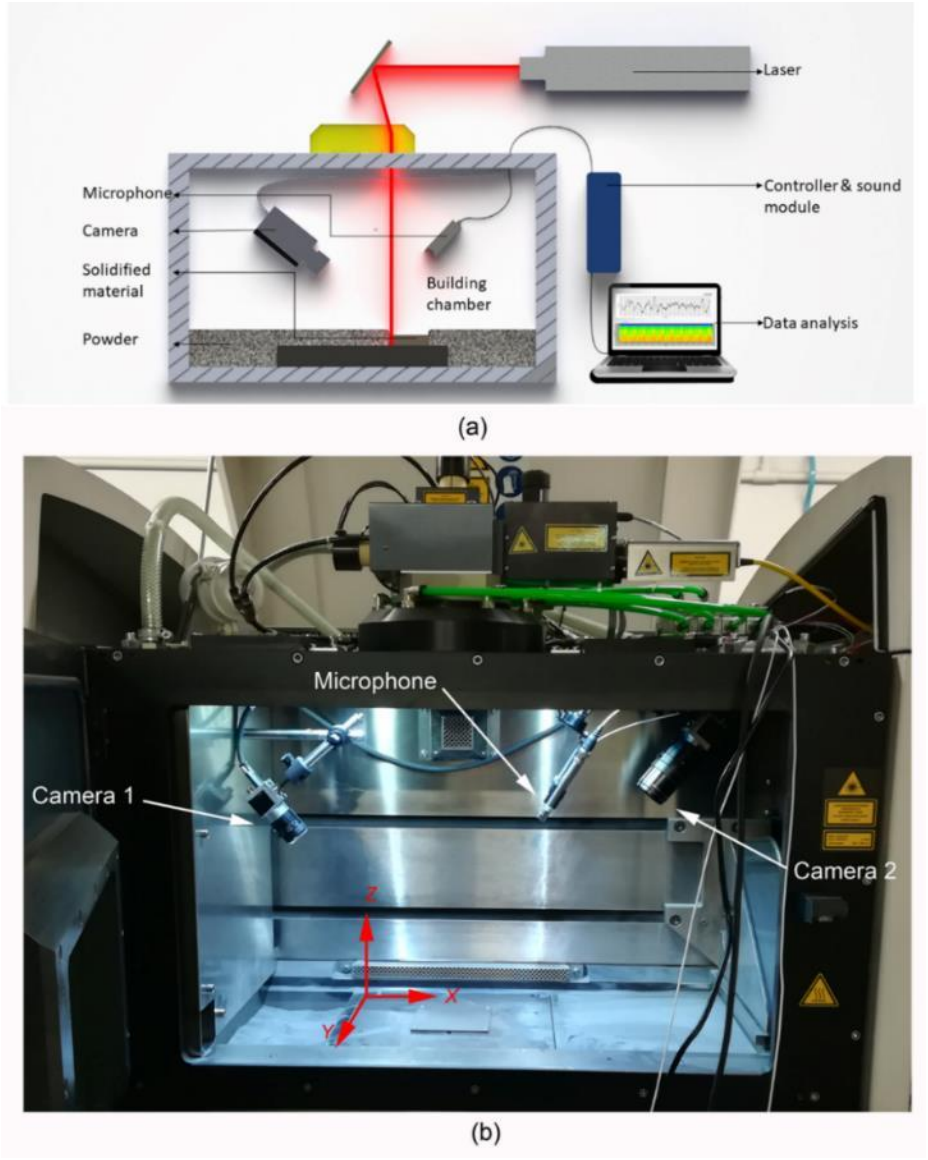

Figure 47: Schematic of experimental setup (a) and building chamber view showing the location of the microphone and cameras. Laser scanning direction and Ar flow were in Y direction for single tracks and layers

The sound propagating through the surrounding protective atmosphere was recorded and analyzed after the LPBF process. The data was recorded using NI CompactRIO-9030 Controller and a 24-bit measurement module: NI 9250, specifically designed for recording signals from microphones (Figure 47). An integrated circuit piezoelectric (ICP) microphone

(Model 378BO2, see appendix for calibration certificate) was installed at an angle of 20° to the vertical and 240 mm above the edge of the building platform and used to record the AE signal (Figure 48). The 378B02 microphone (PCB Piezotronics) has an optimal frequency range of 3.75–20 000 Hz (±2dB). According to the Nyquist criterion, the sampling frequency for Fast Fourier Transform (FFT)-based measurements is required to be at least twice the maximum frequency component in the signal. In the present investigations, AE data for each test was acquired at a sampling frequency of 102.4 kHz, i.e. ~5 times higher than the maximum measured frequency of 20 kHz.

Figure 48: NI CompactRIO-9030 Controller, NI 9250 sound module and PCB 378BO2 microphone.

3.5 Design of experiments

3.5.1 Validation of microphone placement in the building chamber

The effects of the environment, noise, location of the sensor, etc. need to be considered before taking measurements (Alfaro and Cayo, 2012; Horvat *et al.*, 2011; Yusof *et al.*, 2017). Factors can change for various reasons, for example, absorption of a material is a function of the frequency, i.e. different frequencies from the process will be reflected and absorbed at different rates within the machine.

Microphone placement was the only test carried out using maraging steel. Maraging steel MS1 from EOS, with the chemical composition being Ni 17.6%, Co 8.88%, Mo 4.85, Ti 1.06%, was used. From literature it can be seen that a change can be expected in acoustic signature between MS1 and Ti6Al4V due to different process parameters that are used. This section only considers the effects of the experimental setup which stays constant irrespective of the material being used. Powder layer thickness was 50 µm. The building chamber was filled with nitrogen atmosphere. Single tracks, 200 mm in length, were scanned at a laser power of 305 W with a scanning speed of 1.01 m/s.

To determine if AE differs with respect to the distance from the microphone, the microphone was fixed above the substrate and the laser scanned at five different positions 40 mm apart. Each set contained three tracks. Tracks were scanned consecutively from Position 1; Track 1 (P1; T1) on the right, to the left end at Position 5; Track 3 (P5; T3) (Figure 49).

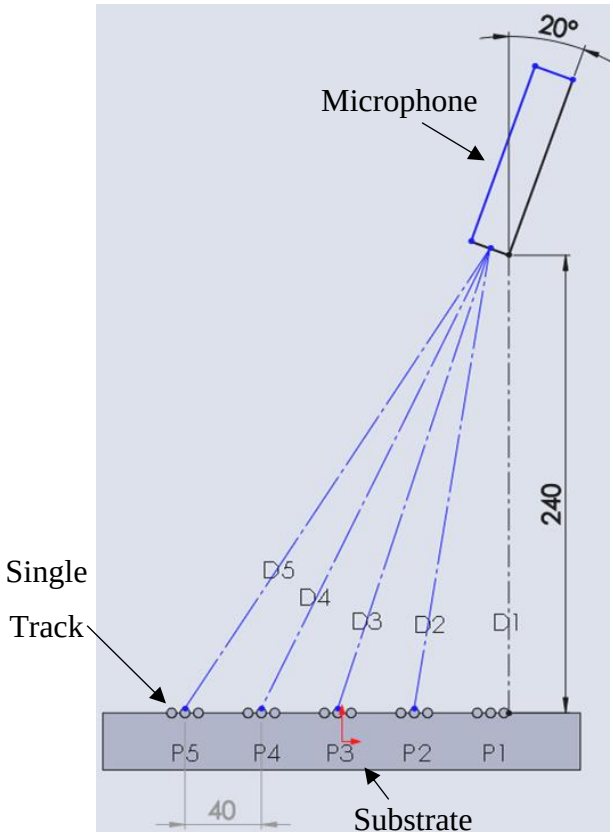

Figure 49: Correctional view of system layout.

In Figure 49, the distance from the microphone edge to the midpoint of each position is indicated and their corresponding values are shown in Table 6.

Table 6: Distance from microphone to different scanning position

	D1	D2	D3	D4	D5
Distance (mm)	240	243.31	252.982	268.328	288.444

According to the microphone polar plot (Figure 50), any sound entering the microphone at an angle greater then 20 degrees will influnce the measurement. The angle of the microphone at different scanning positions is shown in Table 7.

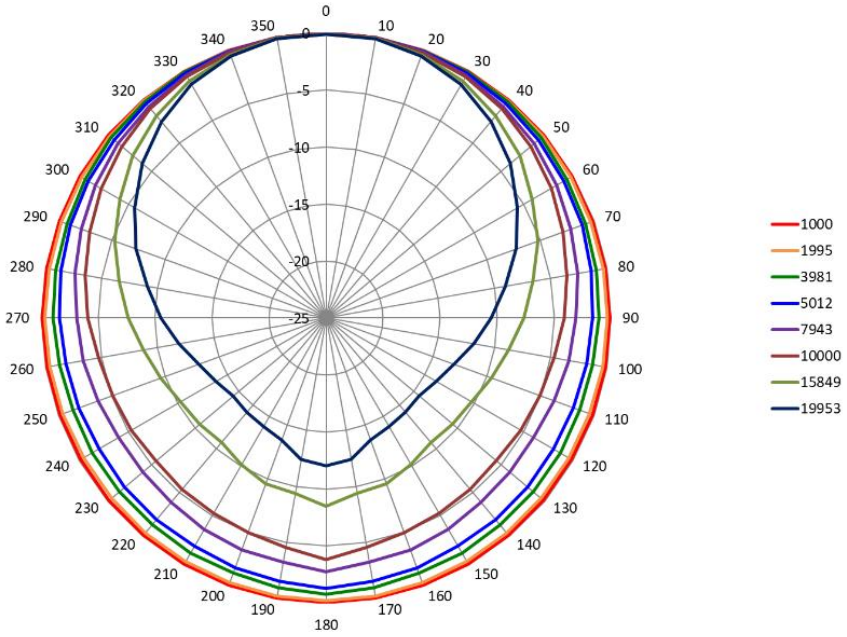

Figure 50: Microphone polar plot, frequency in Hz at 10-degree increments (377B02; SN167925)

Therefore, the microphone angle should be < 20 degrees to make accurate comparisons. The angle between the microphone and the centre of the five positions can be calculated by;

$$\theta' = \tan^{-1}\frac{x}{h} - \theta$$

Where:

x= horizontal distance

h= *height*

θ= angle of microphone

Table 7: Angle between microphone at different scanning positions

	P1	P2	P3	P4	P5
Angle (degrees)	-20	-10.54	-1.57	6.57	13.69

Each individual scan track was extracted from the total data scan to ease analysis. The average sound pressure at individual scans was calculated. Thereafter, the frequencies at each position were analyzed to determine whether certain positions might amplify or absorb some frequencies due to their position in the system. The individual frequency content was analyzed

using power spectrum and correlated with one another. Since all the process parameters are physically the same with the only difference being distance from sensor, good correlation results would indicate the optimal sensor placement (*>0.99, results are shown in section 4.2,* Table 12*)*. Microphone placement was the same for all experiments.

3.5.2. Critical powder layer thickness pores

It is important to estimate the critical thickness of the powder layer where irregular track formation and hence, porosity in 3D objects initiate. This was investigated by manufacturing 3D samples with intentionally designed horizontal cavities where the laser beam does not melt areas of between 30 to 300 µm in height. In this way, the critical layer thickness for porosity formation can be evaluated. In order to evaluate the porosity quantitatively, samples were micro-CT scanned and cross-sectioned. After determining critical layer thickness, single tracks were investigated. As the basic building blocks of the LPBF process, single tracks were manufactured at different process parameters and with different layer thicknesses.

A test sample with artificial rectangular cavities was designed to find at what critical powder layer thickness pores start to form. The thickness of the designed cavities varied from one to six times that of a single powder layer (30 µm to 180 µm), as shown in Figure 51. Each step is 1 mm in height and 5 mm in width and length. The resulting porosity found by CT scans and cross-sections, as shown in section 4.1, in each of these cases in the final part aim to demonstrate what the critical layer thickness is for optimal process parameters.

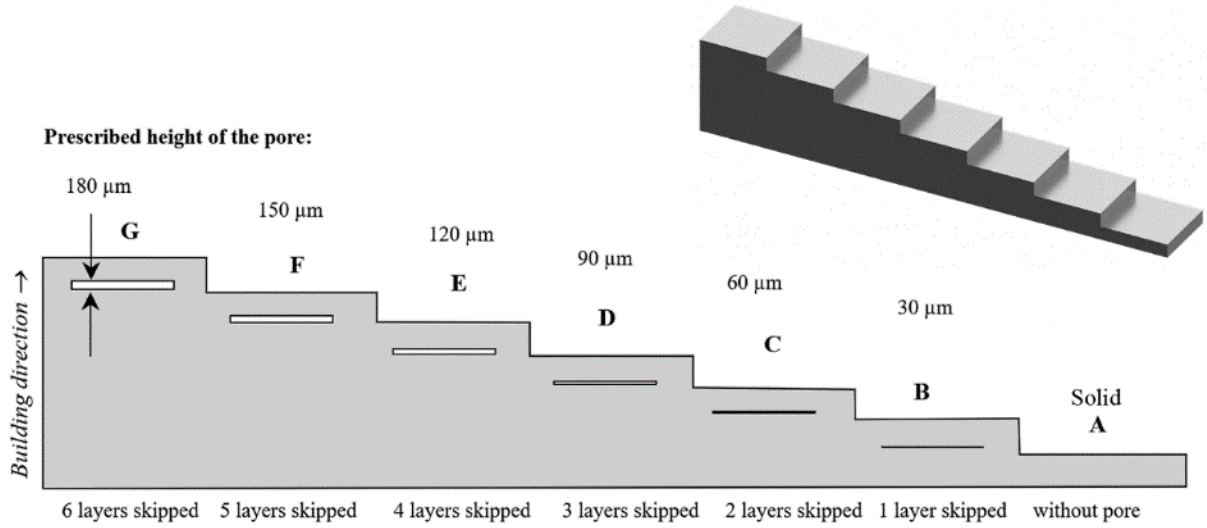

Figure 51: Test sample: solid part (A) and parts with prescribed internal cavities of 30–180 µm (1–6 powder layers skipped) (B-G)

3.5.3 Experiments with single tracks at different process parameters

Various papers on the use of AE and machine learning for online monitoring are available, however, none really investigating the effect of the AE under different circumstances. This section establishes some fundamental basis of how variables might change the AE. This information can then be used later for development.

To establish a correlation between the sound pressure level (SPL), the frequency spectrum of the sound and the shape of the single tracks, a series of experiments were performed. Firstly, two tracks per set, 48 mm in length, were manufactured on a substrate without powder and with different thicknesses of the powder layer (30, 60, 120, 150 and 300 µm) at a laser power of 170 W and scanning speed of 1.2 m/s, which is optimal for 30 µm layer thickness (Yadroitsava *et al.*, 2015). The signals from each set of tracks were split into four parts, and average values of eight signals were analyzed.

Secondly, to study the effect of laser power, single tracks (two tracks in each set) were produced on a substrate without powder at 100 W, 170 W and 340 W at fixed scanning speed of 1.2 m/s.

Thirdly, to evaluate the effect of different laser operating modes, laser power was varied at between 100 W, 170 W and 340 W and this time the scanning speed was constant at - 0.6 m/s. This resulted in two tracks positioned 40 mm apart for each layer and set of process parameters. Two tracks were sintered without powder, then a powder layer was delivered, and the laser scanned two tracks next to the previous tracks (1 mm apart). This procedure was repeated for the corresponding layers.

Each track's corresponding sound waveform was extracted from the recording and analyzed with Fast Fourier Transform (FFT) and the sound pressure level (SPL) calculated as shown in the results, section 4.3. For optical microscopy, top and cross-sectional images were obtained. The data was used to correlate the track morphology to the frequency spectrum for the specific layer thickness.

3.6 Layer thickness recognition algorithms

After considering the critical layer thickness and understanding the relationship between the AE and process variables, the following section investigates possible ways in which the LPBF process can be monitored online, although these results were obtained using recordings. It was shown that rapid heating by laser beam, melting, solidification and cooling of powder and substrate materials generate temperature gradients in gaseous medium, and in turn, gas pressure

changes. Pressure gradients lead to the generation of the acoustic waves and create a “voice of the process”. The emission of acoustic vibrations in the protective Ar atmosphere is registered by the microphone. From a mathematical point of view, analysis of the AE signal during processing is based on a pattern recognition problem. For this section only, layer thickness recognition will be variable. Two methods were proposed: the first method that was investigated was as a preliminary proof of concept. The second method only considered the audible range (0–20kHz), and being superior to the first with a greater statistical significance.

Layer thickness recognition algorithm 1

These research experiments were run parallel with other experiments that were aimed at obtaining an insight into the development of the single-track and layer formation of in-situ alloying of Ti6Al4V-5 at % Cu during LPBF. To determine the effect of powder thickness on AE during laser scanning, single tracks with a length of 20 mm were manufactured. Three tracks were produced at two different layer thicknesses: one layer (30 µm) and five layers. Two tracks from each layer thickness were used to create the models. The third track of each sample that was not used in the generation of these models was then evaluated against the models to see whether the model could predict from which layer the track was produced. Laser parameters were constant at 170 W and 1.2 m/s. Data was then analyzed by making use of an FFT. The proposed method is described in section 4.4.1

Layer thickness recognition algorithm 2

To investigate the repeatability of the AE signals, three sets of ten tracks, each 90 mm in length, were produced at 170 W and 1.2 m/s scanning speed. Tracks for the reference layer thickness of 30 µm, tracks without any powder and tracks with a 120 µm thick layer were produced. This series of experiments simulates extreme scenarios of non-homogeneous powder layer thickness in LPBF. From the preliminary test, a critical powder layer thickness (120 µm) was chosen to trigger the balling effect that is known to provoke porosity in 3D-printed LPBF parts. Single layers of 10 mm x 10 mm were produced at the same laser parameters with a one-directional scanning strategy and 100 µm hatch distance.

To identify the model required for the identification of irregular morphology of tracks through AE, the recorded data was also processed using STFT. To obtain an initial general conception of the sound emitted during the LPBF process, STFT was selected as it is relatively easy to implement and interpret. An STFT spectrogram of ten tracks for each set was done without powder (0), one layer (1, reference 30 µm layer) and critical (thick 120 µm layer)

powder thickness. To create the models, ten tracks for each layer thickness were used. These ten tracks were then split into two groups. One group was used to build the model and another group for testing. The model was built using the first six tracks. The remaining four tracks were each tested against the models.

The steps in the forming of the algorithm are:

- Apply a 2 kHz high-pass filter to remove the noise from the signal
- Calculate the frequency domain and identify the frequency content of each layer thickness
- Use the identified frequency content and create a model that could recognize a deviation

The aim of the model is to make use of the identified frequency content to determine regimes of "balling-humping"-forming phenomena, scanning without powder or on a thick layer of powder that can cause lack-of-fusion defects in parts manufactured by LPBF.

Chapter 4: RESULTS AND DISCUSSION

4.1. Powder layer thickness and pore formation in 3D samples

The height of the rectangular cavities in 3D samples were designed in the range of 30–180 µm. Up to 180 µm (six skipped powder layers), an open cavity was not produced as expected, and the designed rectangular pore had the appearance of a chain of irregular pores, as observed in CT scans (du Plessis *et al.*, 2016) and physical cross-sections (Figure 52). The cross-section of the sample showed that the internal cavities had irregular shapes and pronounced lack-of-fusion defects which only started at 120 µm thickness of the powder layer (samples E–G), Figure 52. In samples with defects designed at 30, 60 and 90 µm in height, only random small pores with sizes less than 50 µm were found. Thus, at the selected laser power and scanning speed, a layer thickness designed at and above 120 µm led to a chain of pores, or lack-of-fusion porosity samples E–G in Figure 52.

The shape of single tracks at different powder layer thicknesses, at similar laser power and scanning speed, was analyzed further in section 4.3. The progression of increasing track irregularity with increasing powder thickness is clear, up to balling effect at high thickness.

Surfaces and size resolution for fine structures remain a limitation in LPBF, even after applying special scanning strategies. CT in combination with physical sectioning has proved to be a powerful analysis combination. Critical layer thickness for porosity in LPBF samples is 120 µm. Powder inside pores and component mass (due to removal from substrate) remains a concern for LPBF components. Establishing the limitations of AE, i.e. minimum size and the typical defects, will assist as a quality control method for LPBF components.

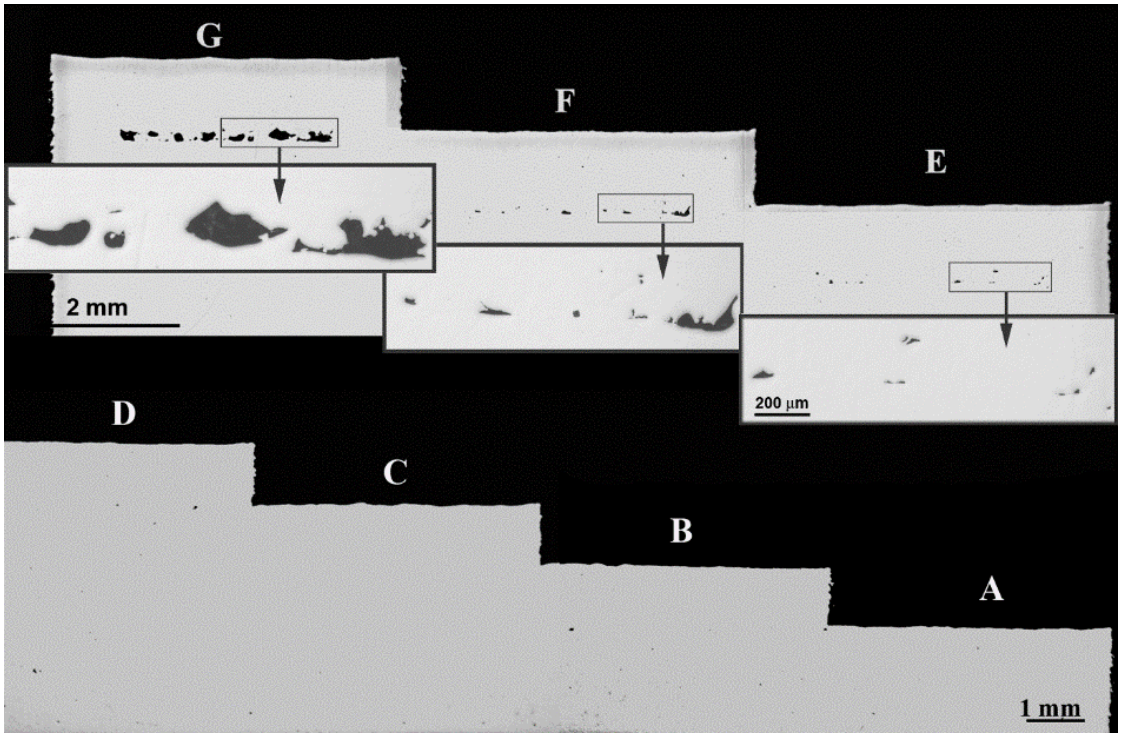

(a)

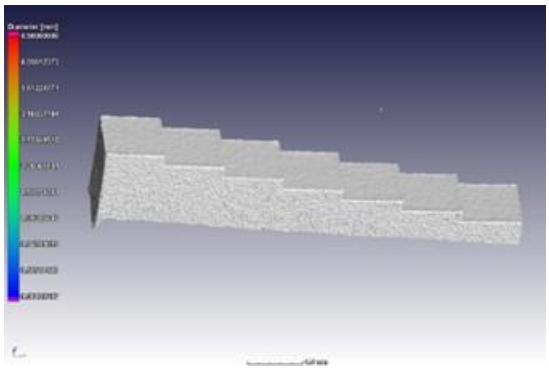

(b)

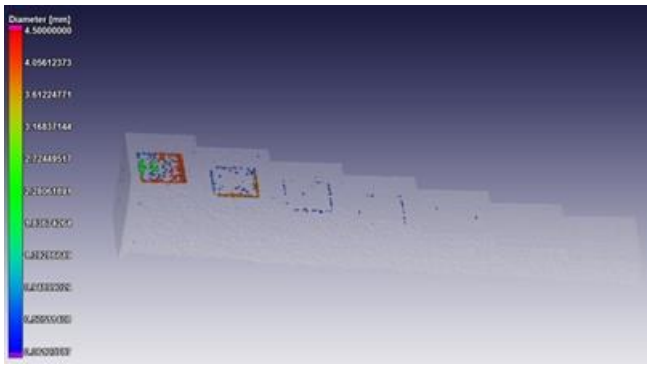

(c)

Figure 52: Images from optical microscope of cross-sections of the 3D test sample with designed internal cavities of 30–180 µm (a) and pore volumes from CT reconstruction (b) and transparent image with pores (c)

4.2. Validation of microphone placement for AE processing during metal LPBF

Factors like the effect of sound reflections, machine environment, noise and the location of the recording device need to be considered as a basis of qualification. This section shows the analysis of the results of AE sensor placement as sampled in the actual metal LPBF machine. These results include all the environmental factors as well. The tracks were visually analyzed and no major irregularities were present. A section of the tracks at Position 1 is shown in Figure 53.

Figure 53: Track 1 to 3 of Position 1 on maraging steel tracks on the substrate at 305 W laser power and scanning speed of 1.1 m/s at 50 µm powder layer thickness

The entire signal of the process, from start to finish, is shown in Figure 54. Here it can be seen that the EOSINT M280 has various processes that emit sound, but no clear scanning is shown until the filtering and processing is applied. When listening to the recording, one can hear two distinct sounds of valves opening/closing at ~6 and ~17 seconds, thereafter the sound of a blower starting at ~25 seconds and ending with a laser scanning at ~52 seconds. A high-pass filter was used to remove the low-frequency noise from the blower and ambient noise. It was found that by applying the 2 kHz high-pass filter, the tracks were clearly distinguishable in the time domain. The scanning time of each track is equal to the time that it would take to scan a track 200 mm in length at a speed of 1.1 m/s, as shown in the bottom of Figure 54.

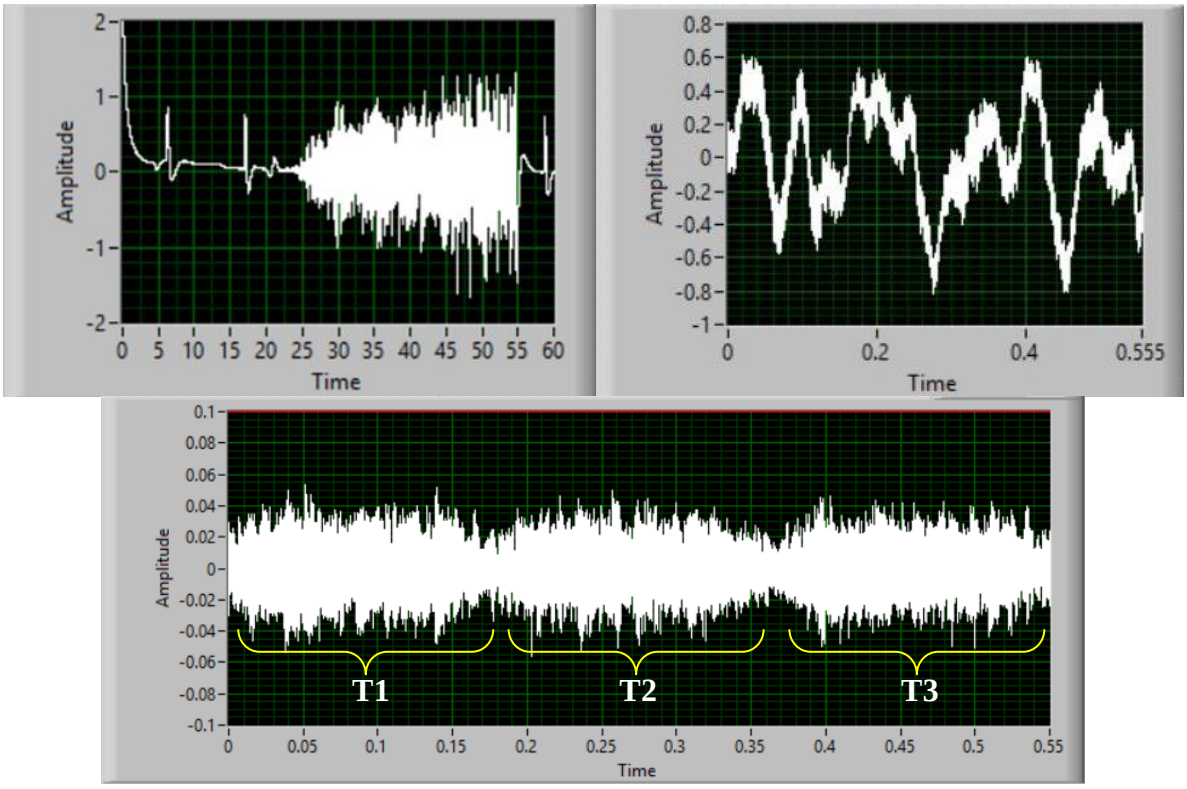

Figure 54: Graph of entire process recording over time in seconds (top right), signal of first three tracks before filtering referenced from zero (top left) and after applying signal filtering (bottom) (note the amplitude of the actual scanning)

After the tracks were identified, some calculations were carried out to determine what the effect of the machine and scanning position were. The individual RMS value sound pressure level

(SPL) showed no large variations in relation to the distance from the microphone. Variations could be attributed to slight differences in powder layer thickness over the platform. Table 10 shows the SPL of scanning at each position. The maximum fluctuations in sound pressure during the process were calculated by taking the maximum and minimum value of Track 1, 2 and 3, as shown in Table 8 and Table 9.

Table 8: SPL at each position (dB)

	P1	P2	P3	P4	P5
Average	83.25	83.12	83.17	82.85	83.39
Standard deviation	0.657	0.351	0.760	0.472	0.198

The maximum expected difference due to the distance to scanning is given by

$$\Delta SPL = 20log\frac{d_{P5}}{d_{P1}}$$

$$\Delta SPL = 20log\frac{0.288}{0.24}$$

$$\Delta SPL = 1.579dB$$

Table 9: Maximum and minimum SPL value and corresponding SPL difference

Track	Max	Min	Δ SPL
T1	83.52	82.35	1.17
T2	84.01	83.29	0.72
T3	83.59	82.50	1.10

The speed of sound in argon; T = 298 K, R = 208.13 J/kg·K, γ = *cp* / *cv* =1.667 is equal to 321.006 m/s and for nitrogen (R = 296.8 J/kg·K, γ=1.4) is equal to 351.807 m/s. Based on this speed, the maximum change in frequency at 2 kHz, due to the Doppler effect, at a scanning speed of 1.2 m/s is calculated;

$$f_{p(2kHz\ at\ 1.2m/s)} = 2000\frac{321}{321 - 1.2}$$

$$f_{p(2kHz\ at\ 1.2m/s)} = 2007.50Hz$$

Table 10 shows how different scanning speeds will change the perceived frequency at different laser parameters for different frequencies.

Table 10: Doppler frequency at various frequencies and scanning speeds in argon

	Scanning speed (m/s)	Perceived f *(Hz)*	Δf *(Hz)*
2 kHz	0.6	2003.75	3.75
	1.2	2007.50	7.50
	2.4	2015.07	15.07
20 kHz	0.6	20037.45	37.45
	1.2	20075.05	75.05
	2.4	20150.66	150.66
50 kHz	0.6	50093.63	93.63
	1.2	50187.62	187.62
	2.4	50376.65	376.65

The maximum change in frequency due to scanning speed can be ignored for this study, since we will not consider such small changes.

Assuming the shape of the chamber to be a simple rectangle with dimensions; l = 675, w = 338 and h = 430mm, the mean free path between reflections is;

$$MFP = \frac{4(0.675 \times 0.338 \times 0.43)}{2(0.675 \times 0.43) + 2(0.675 \times 0.338) + 2(0.338 \times 0.43)}$$

$$MFP = 0.296m$$

Thus, the time for average reflection $= \frac{0.296}{321} = 0.001$ sec which is equivalent to 1 kHz (this is smaller than filter discussed later in the section).

The reflection in the LPBF chamber will be complex due to the nature of the components present and the changing environment. The absorption coefficient for powder varies with thickness of the layer. Absorption is strongly dependent on the frequency. Okudaira *et al.* (1993) measured absorption for non-metal powder beds: for frequencies below 1.2 kHz, absorption has very distinct high peaks, thereafter it remains constant at approx. 0.2–0.4, depending on the material, type and particle size distribution. Smaller particle sizes have lower absorption at high frequencies (Okudaira *et al.*, 1995). Fine powders (~50µm) with a higher bulk density do not seem to have high absorption values (<0.2) (Sakamoto *et al.*, 2019). As for

the metal powder used in AM, we can assume that absorption coefficient is equal to 0.1 (the author is not aware of any literature regarding the sound absorption coefficients for metal powder). For an estimation, assuming all surfaces are treated as having the same absorption coefficient, the absorption coefficient can be approximated for a constant value that is similar for powder and sheet metal; 0.1 (NRCratings.com., 2020), then the time it takes for the reflections to die out, *i.e.* reverberation time, is given by

$$RT_{60} = \frac{55.25\ (0.675 \times 0.338 \times 0.43)}{321 \times 2(0.675 \times 0.43) + 2(0.675 \times 0.338) + 2(0.338 \times 0.43) \times 0.1}$$

$$RT_{60} = 0.127sec$$

With the critical distance being

$$d_c = 0.057\sqrt{\frac{V}{RT_{60}}}$$

$$d_c = 0.057\sqrt{\frac{0.098}{0.13}}$$

$$d_c = 0.05m$$

meaning that the measurements were taken in the reverberant field. This will not influence the comparisons since the environment remains the same. The axial resonance mode has the greatest effect (tangential having half the energy and oblique a quarter), and the fundamental of each wall of the rectangular area are given by

$$f_{mode} = \frac{v}{2}\sqrt{(\frac{p}{L})^2 + (\frac{q}{W})^2 + (\frac{r}{H})^2}$$

$$f_{1st\ axial} = \frac{321}{2}\sqrt{(\frac{1}{0.675})^2 + (\frac{0}{0.338})^2 + (\frac{0}{0.430})^2}$$

$$f_{1st\ axial} = 238\text{Hz}$$

The first twelve modes for this rectangular chamber are given in Table 11.

Table 11: First 12 resonant modes of LPBF chamber

p	q	r	Resonant frequency *(Hz)* and mode
1.00	0.00	0.00	238, axial
0.00	1.00	0.00	475, axial
0.00	0.00	1.00	373, axial
1.00	1.00	0.00	531, tangential
2.00	0.00	0.00	476, axial
1.00	0.00	1.00	443, tangential
0.00	1.00	1.00	603, tangential
2.00	1.00	0.00	672, tangential
1.00	1.00	1.00	649, oblique
2.00	0.00	1.00	604, tangential
3.00	0.00	0.00	713, axial
0.00	2.00	0.00	949, axial

The frequency range where modal resonance end is

$$f_{\text{crossover}} = 2000\sqrt{\frac{0.13}{0.098}}$$

$$f_{\text{crossover}} = 2277\ Hz$$

Since no strong modal resonances are present above 2 kHz and the crossover frequency is close to 2 kHz, the possibility of resonance or standing waves influencing the results can be excluded. In order to understand the machine environment, the signal-to-noise ratio (SNR) of the AE can be calculated. The AE registered signal was comprised of a sound from the environment and from the LPBF process. Therefore, the useful and noise signals were chosen as opposed to extraction of a predetermined/known background noise signal. It was found that after applying a 2 kHz high-pass filter, the signal level was about half that of the noise level with SNR equalling to -4.731 dB. Signal-to-noise ratio was calculated from a FFT as ratio of summing the amplitudes from 0–2 kHz for the noise and 2–20 kHz for the signal. The sound pressure levels reaching the microphone were relatively consistent over the baseplate. To be sure no other frequency distortion was present, the individual frequency content for each track was

calculated (power spectrum) and correlated with Track 1 at Position 1. Table 12 shows that all the positions had good correlation with one another.

Table 12: Power spectrum correlation value of Track 1 with other tracks

P1			P2			P3		
T1	T2	T3	T1	T2	T3	T1	T2	T3
1	0.993	0.999	0.994	0.991	0.993	0.988	0.991	0.994

P4			P5		
T1	T2	T3	T1	T2	T3
0.997	0.994	0.991	0.9995	0.992	0.993

The resonances associated with start-stop of consecutive single tracks need to be considered. Two aspects need to be considered: one being the time between start and stop of the track itself and the other being the time delay between the stop of the previous track and the start of the following track (for a square layer, the electrical signal which turns the laser on and off will be modulated by rectangular wave). For the start-stop of the track itself the frequency can be calculated by approximating the time between the start and stop of the laser to be equal to the time taken to scan each track. For the core of the part, EOSINT M280 uses a scanning strategy that uses a 5 mm and 10 mm long series of tracks (stripes) for Ti6Al4V and MS1 respectively. The 3rd harmonic of a square layer scanned at 1.2 m/s is shown in Table 13, included is a 1 mm square to see the effect of shorter tracks. Varying tracks (shorter than stripe size) are always present in complex part due to the shape of the part being produced.

Table 13:Resonant frequency of laser start-stop modulation for 1, 5 and 10mm square layer at 1.2m/s

Length (mm)	Time (ms)	Fundamental frequency *(Hz)*	3rd harmonic *(Hz)*
1	0.833	1200	3600
5	4.167	240	720
10	8.333	120	360

For the time delay between stop and start of consecutive tracks, a delay time of 1.5 ms will result in a fundamental frequency of 666.667 Hz. These modulation calculations do not take

into consideration the effect of the AE frequencies emitted due to melting and solidification phenomena. If we assume that the higher harmonics (>3rd) contain negligible amplitudes, this will not contribute to FFT amplitudes of this study but does warrant further investigation.

In the present study, using a 2 kHz high-pass filter, good correlation and similar RMS values were obtained and one can conclude that the current sensor position in this setup was not influenced by the environment or scanning position. Analysis was done inside the EOSINT M280 machine using maraging steel; placement with chosen distances seem to be adequate, but care should be taken if any variable, such as machine, sensor or material, is changed. Thus, quality of online AE measurements can be trusted for non-contact AE during online detection of porosity-forming phenomena during metal LPBF.

4.3 AE for LPBF process at different process parameters

This section establishes some fundamental basis of how different variables affect the AE. Since single layer is a superposition of the synthesized single tracks, surface morphology of the layers depend on geometrical characteristics of single tracks, scanning strategy and hatch distance. Therefore, a fundamental knowledge of the single tracks and corresponding AE are needed.

4.3.1 Powder thickness variation

The extracted sound signal of Track 2 after filtering is shown in Figure 55. The amplitude of signals clearly increases with powder thickness. The start of the track can be identified by the increase in activity (red colour). A clear initial spike is observed at the beginning of scanning without powder which agrees with the development of AE shown by Luo *et al.*, (2019). With powder layer processing, the sound does not exhibit the initial peak at the start of scanning. The amplitude of the average signal reaches a maximum at a certain powder thickness, thereafter the amplitude decreases, as seen when comparing two and ten layers in Figure 55.

In the first series of AE experiments with single tracks, clear differences in track morphology were observed from the top and cross-sectional views at different layer thickness, (Figure 56). Note the uniform smooth tracks on the substrate without powder. Regular continuous tracks were produced up to layer thickness of 60 μm.

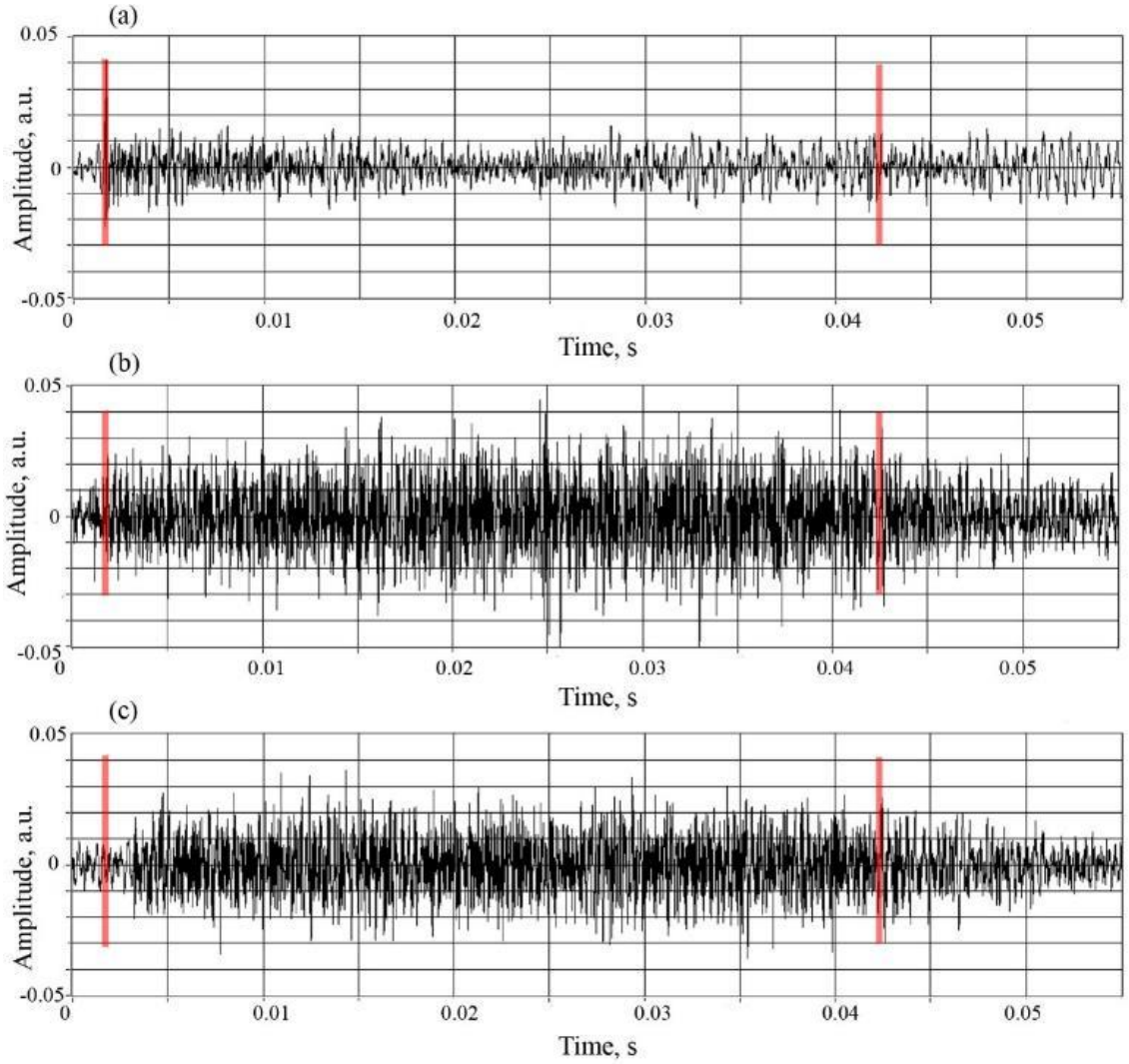

Figure 55: Extracted and filtered AE signal of Track 2 without powder (a), two layers (b) and 10 layers (c) showing registered amplitude versus time

Irregular tracks started at 120 µm powder layer thickness. At this thickness pre-balling effect begins, where tracks were still continuous but had an irregular shape in the form of a sequence of beads interconnected by curved tapering tracks. The tracks on the 300 µm thick powder layer had no regular metallurgical contact with the substrate – only some molten beads were slightly attached to the substrate at random areas. This means that at this laser power, spot size and scanning speed, the energy from the laser beam was not enough to melt both the 300 µm powder layer and the substrate material.

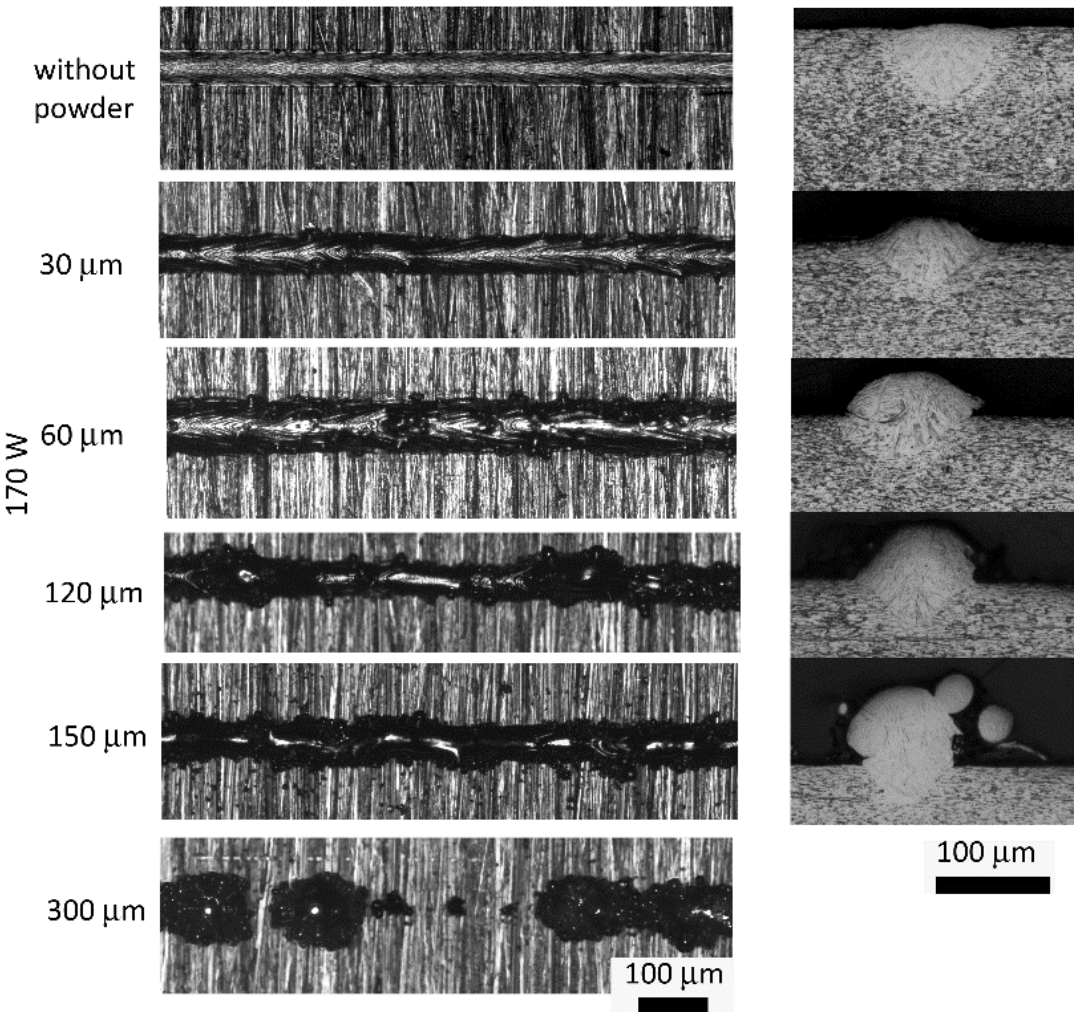

Figure 56: Typical view of single tracks on the substrate at different powder layer thickness: top view (left) and cross-sections (right) at scanning speed of 1.2 m/s and 170 W

With increased powder layer thickness, more material is involved in the process which increases the size of the top part of the track and decreases the depth of penetration into the substrate and contact zone (Figure 56 and Figure 57). With increasing powder layer thickness, variations of geometrical characteristics also increased (Figure 57); tracks lost a stabilizing factor such as joint melt pool with the substrate and became irregular. A decreased penetration depth into the substrate material ultimately caused lack-of-fusion porosity (Yadroitsev, 2009; Oliveira *et al.*, 2020). During the process of formation of a single track, the value of the recorded SPL increases with increasing layer thickness up to 120 µm and then a turning point is reached (Figure 57). The analysis of the cross-section showed similar behaviour in the contact zone, which also reached a maximum at a layer thickness of 120 µm (Figure 57). When more powder and substrate material were involved in the process, this corresponded to higher AE intensity. Then, when the track lost continuous contact with the substrate, the SPL decreased. At laser power of 170 W and scanning speed of 1.2 m/s, and layer thickness above

60 µm, single tracks start to lose metallurgical contact with the substrate. Thus, the substrate begins to be excluded from the process and, therefore, AE is emitted. Any further increase in the powder thickness will lead to absorption of sound by the powder and ultimately stabilize the SPL value.

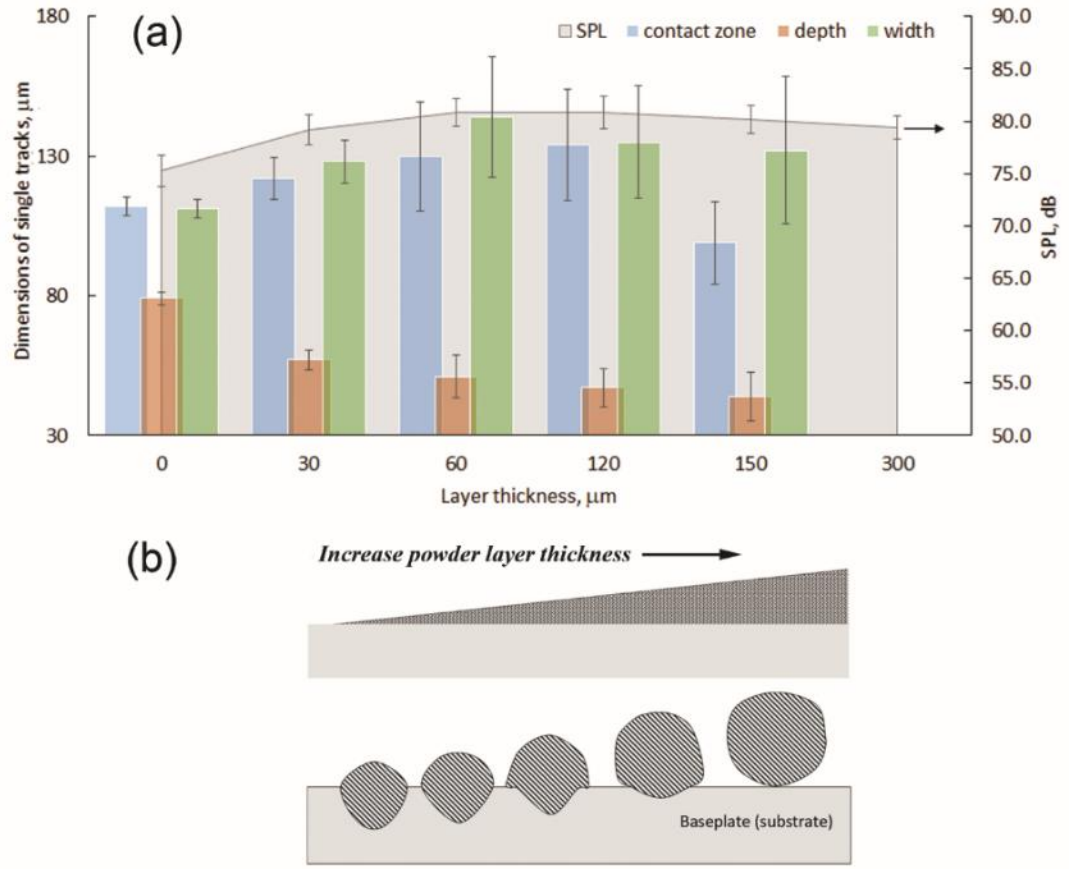

Figure 57: Geometrical characteristics of single tracks at 170 W and 1.2 m/s and the corresponding total SPL (a); evolution of the cross-section shape with powder layer thickness (b)

Spectral analysis of the signal for the single tracks showed that with an increase in the thickness of the powder layer, not only the total SPL changed, but also the spectral frequency of the sound (Figure 58). At low layer thickness it is very difficult to deliver a homogenous powder layer due to individual particle sizes in the same order of magnitude. Some heterogeneity in the layer thickness will be present and will affect the morphology of the single track and the corresponding AE. Thus, non-parametric median values of AE frequency spectrum were studied.

All processed layers had high median values of AE intensity amplitudes at 2 and 3 kHz. Without powder, the peaks were low, especially beyond 10 kHz (Figure 58). At the reference 30 μm powder layer the amplitude of the signal increased for all frequencies. The signal was stable without expressed peaks. With an increase in the layer thickness to 60 μm, peaks were found at 12 kHz. Further increasing layer thickness up to the critical value of 120 μm led to the appearance of high signals, near 6–7 kHz, with amplitudes 1.5 higher than without powder. At 150 μm layer thickness, peaks shifted to lower frequencies. Some high amplitude peaks were found for 300 μm single tracks at 5.5–8 kHz, the high frequency spectrum had lower amplitude and shifted left. The overall amplitude of the frequencies follows the same pattern as with the SPL in that the energy increases up to 120 μm layer thickness and then decreases thereafter. As the powder layer increases beyond 10 layers (300 μm), the melt pool will not touch the substrate at all as the penetration depth into the powder bed stays at maximum regardless of the thickness of the powder layer beneath the track and, therefore, the intensity of sound at all frequencies stayed the same (Figure 58). In general, due to the high variability of the amplitudes, it was difficult to find a trend between the dominant frequencies and the thickness of the layer at the studied frequencies. A correlation was not readily apparent, therefore not quantitatively assessed.

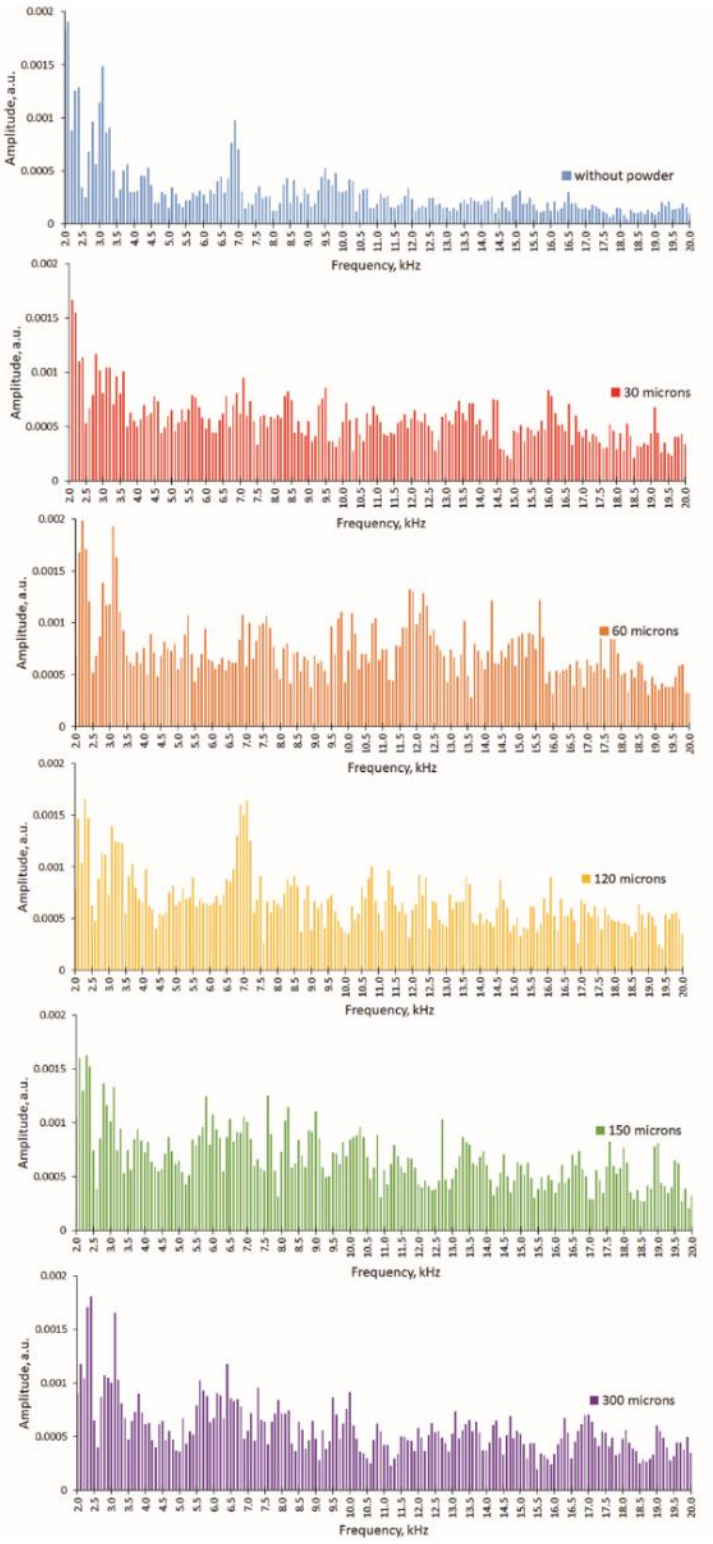

Figure 58: Frequency spectrum and median intensity of AE signals for single tracks produced without powder and 30–300μm powder layer thickness

Apparently, the main sign of an increase in the layer thickness and the associated balling effect is the presence in the spectrum of high amplitudes at frequencies of about 7–10 kHz, but this

assumption should be studied on a larger number of single tracks forming a single layer at different layer thicknesses.

4.3.2 Influence of laser power on AE signal during scanning single tracks

AE signal for laser processing of the substrate without powder at 100 W, 170 W and 340 W and 1.2 m/s scanning speed was studied. At 100 W, the amplitude of frequencies above ~7 kHz was low, and the cumulative amplitude was almost constant (Figure 59). At 170 W and 340 W, high frequencies started to contribute more in AE and the cumulative amplitude increased 1.5 and 2.7 times in comparison with 100 W processing, correspondingly.

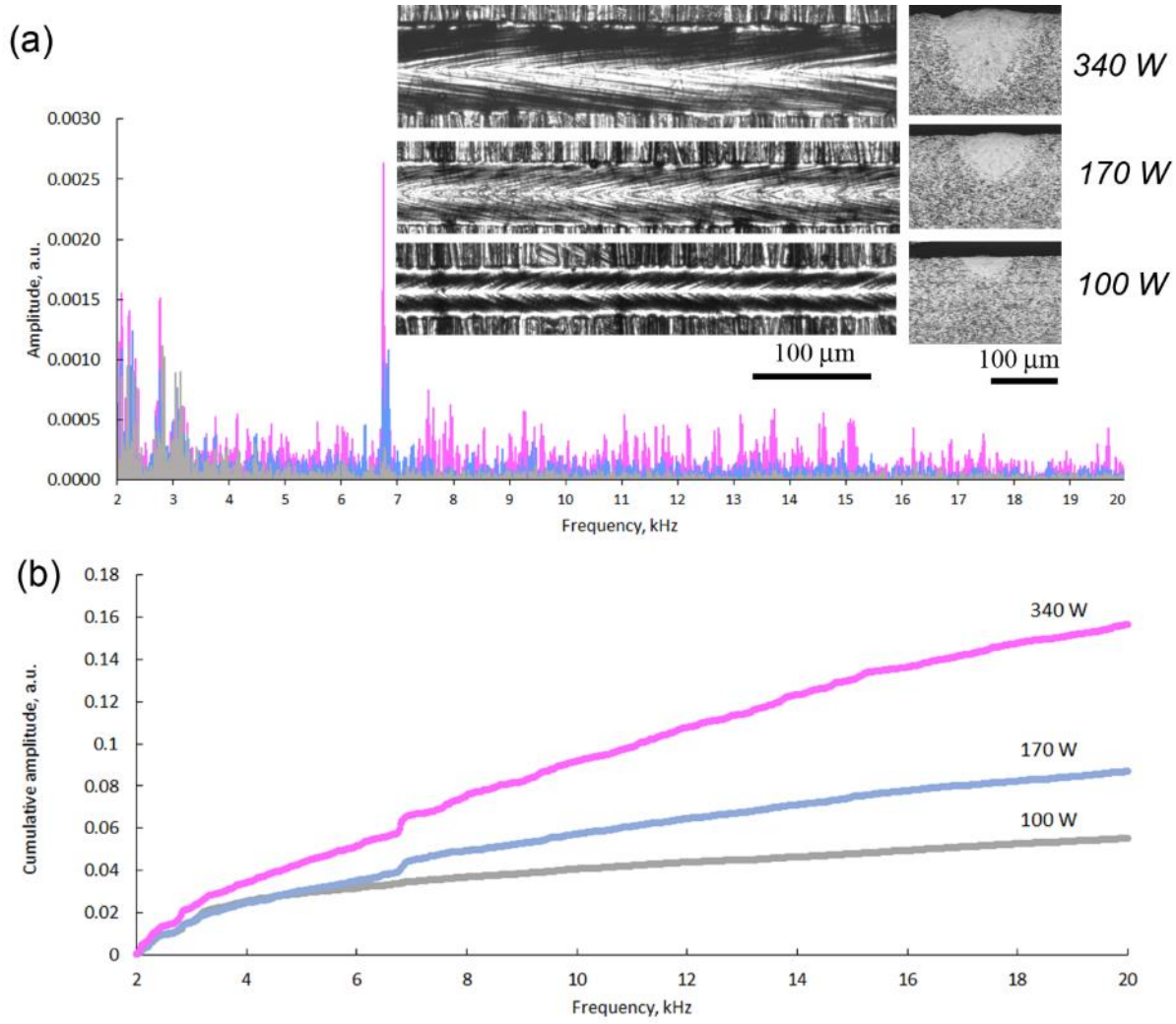

Figure 59: Typical FFT spectrum and photos of single tracks without powder at 100 W, 170 W and 340 W laser powers and 1.2 m/s scanning speed (a) and cumulative amplitude at 2–20 kHz (b)

Increasing laser power leads to a wider and deeper melt pool (Figure 59a) and the AE energy that is integral to the FFT power spectrum over all frequencies also increased (Figure 59b). The SPL at the formation of single tracks without powder was 73.5 ± 1.49 dB, 75.3 ± 1.48 dB and 78.6 ± 3.0 dB at 100 W, 170 W and 340 W laser power, respectively. The generation of

acoustic waves during melting and solidification of the material can be due to phase transformations in the powder and substrate, instantaneous change in the volume of the gas in the region of the melt pool, and the ejection of particles in the process of spattering. An increase in the laser power leads to an increase in the temperature and size of the melt pool with deeper penetration into the substrate up to keyhole regimes. As shown in Mao *et al.*, 1993, keyhole mode dramatically raised AE for laser welding. In LPBF, changing scanning parameters has a drastic effect on the melt pool shape, denudation zone and spattering effects (Bidare *et al.*, 2018a; Yadroitsev, 2009). As shown in Figure 57, the intensity of the AE signal increased when more material was involved in the process. With increasing laser power, the temperature of the melt pool and the vapour pressure significantly increases, which leads to a change in AE signal. Higher energy input also increases the spatter process (Taheri *et al.*, 2018; Wang *et al.*, 2017) which will certainly affect the frequency and intensity of the AE signals. In the present experiments, the spatter effect increases with powder layer thickness and corresponds with the SPL and frequency changes.

4.3.3 LPBF modes and AE

This section sets out to show the characteristic audible AE of single tracks at different keyhole process parameters using the EOSINT M280 system. Conduction mode is obtained at laser power of 100 W, and the keyhole mode at laser powers of 170 W and 340 W (Figure 60). From the top view it can be observed that the track width for all laser powers is uniform throughout the length of the track. The depth of the tracks increased greatly with increase in laser power.

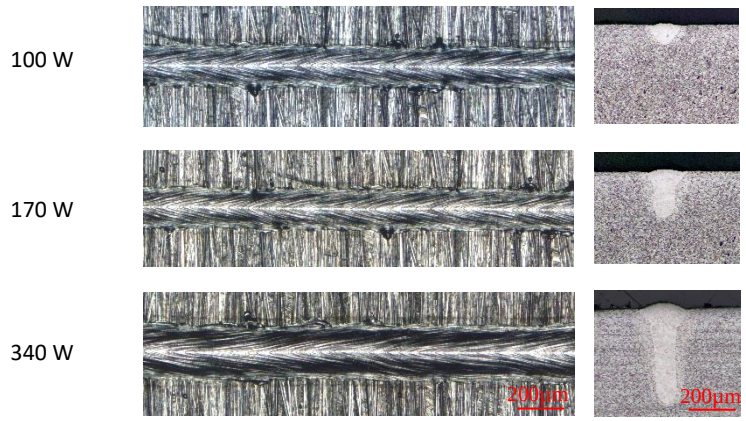

Figure 60: Top view and cross-sections of single tracks without powder at 100 W, 170 W and 340 W laser power and 0.6 m/s scanning speed

Keyhole-mode process parameters are undesirable since they can cause porosity during the LPBF process. At 340 W and 0.6 m/s, various defects are present (Figure 61). An increase in

layer thickness produced vastly irregular tracks with great volume protruding above the substrate, and at 300 µm, there were unmelted particles attached to the irregular track.

Figure 61: Cross-sections showing keyhole porosity and irregular surface of single tracks without powder (left), layer thickness of 120 µm (middle) and 300 µm (right) at 340 W laser power and 0.6 m/s scanning speed

At laser power of 100 W and powder layer thickness of 300 µm, the single tracks did not have contact with the substrate. From the microscopic analysis of the tracks, it was found that the contact zone decreased with an increase in layer thickness for all three laser powers (Figure 62). The contact zone proved to be the only dimension that has a distinct relationship with the sound pressure level. In Figure 63, it can be observed that the SPL decreases with decrease in contact zone; note the increase for 100 W at 30 µm. The width of the tracks followed the same pattern as the contact zone up to 120 µm, and above 120 µm "ice cream cone"-shaped tracks formed which resulted in higher width measurements. At 30 µm, 340 W laser power produced a wider shallow track in comparison to the other layer thicknesses.

The SPL was highest at no powder with 340 W being 89.58 dB. Figure 63 shows SPL increased with laser power and decreased with increasing powder thickness; opposite results were found in the previous section (4.3.1 Powder thickness) which showed that the SPL increases with powder layer thickness at a higher scanning speed of 1.2 m/s. This change in AE can be attributed to the melt pool dynamics that change at higher scanning speeds (Bidare *et al.* 2018).

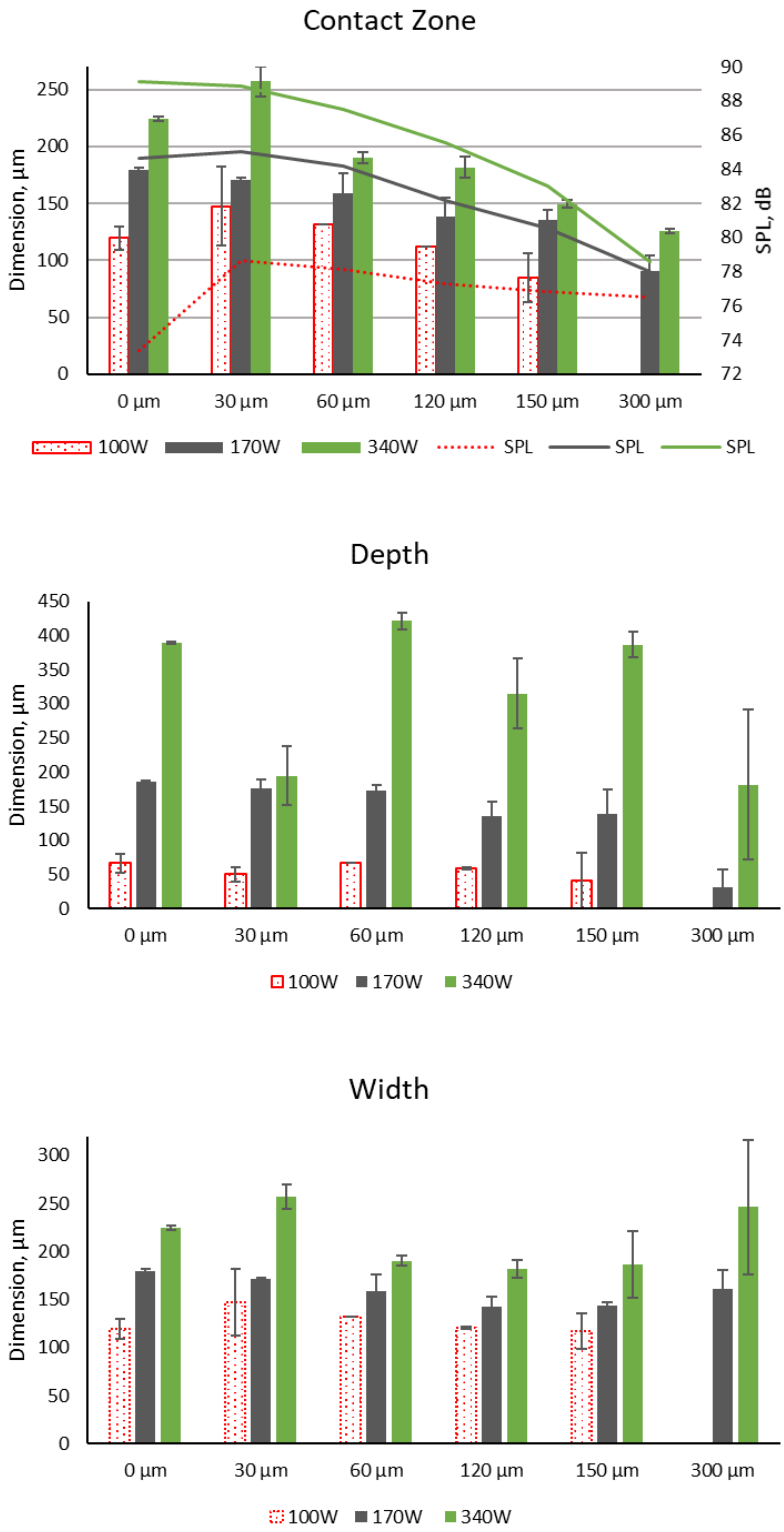

Figure 62: Geometrical characteristics of single tracks at different process parameters, error bars represent standard deviation from mean.

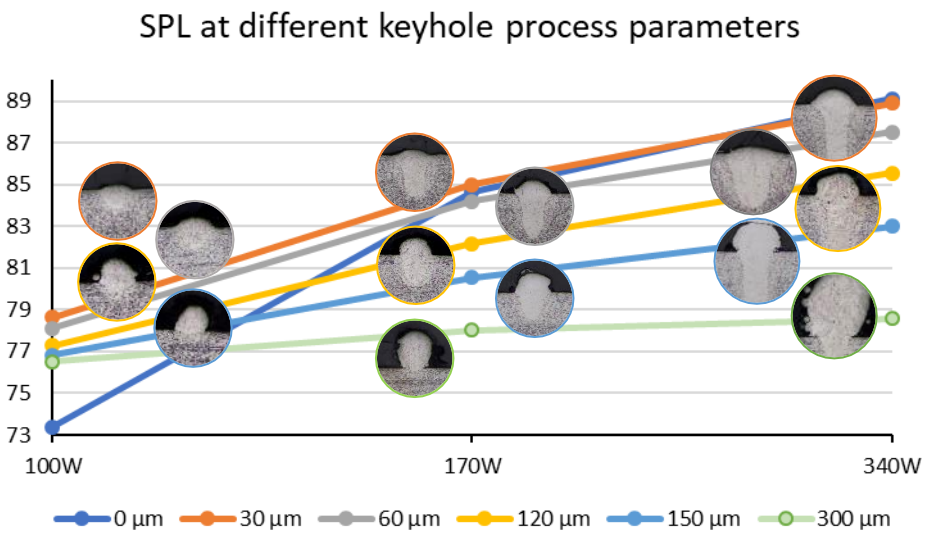

Figure 63: SPL of single tracks at 100 W, 170 W and 340 W laser power and 0.6 m/s scanning speed. Cross-sections at corresponding layer thickness shown.

The frequencies emitted at the two different keyhole parameters (170 W and 340 W at 0.6 m/s) are very similar (Figure 64). This suggests that at these two parameters, the melt pool dynamics are very stable and similar. The same shape is present in both 170 W and 340 W, but 340 W has deeper penetration.

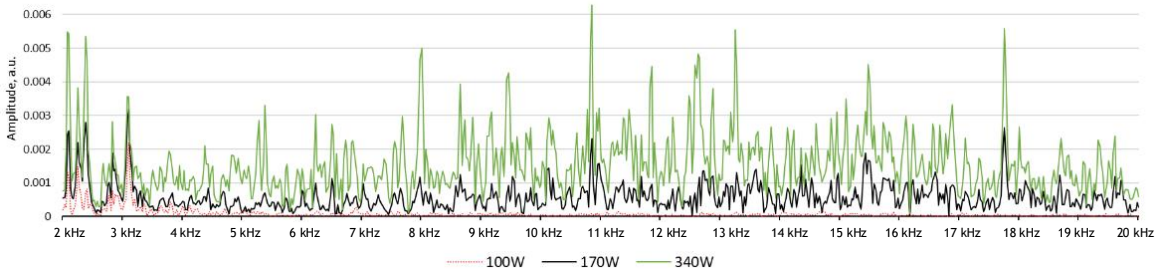

Figure 64: FFT spectrum of single tracks without powder at 100 W, 170 W and 340 W laser power and 0.6 m/s scanning speed

For "no powder" case at 100 W, the linear energy density (*P/V*) is 166.667 J/m and resulted in conduction-mode LPBF. It is interesting that for conduction mode produced with similar linear energy density (*P/V* = 141.7 J/m), but at higher scanning speed (1.2 m/s), a different frequency response was found in the previous section 4.3.2 with a single high peak at ~7 kHz, which cannot be seen for 0.6 m/s (Figure 65). This implies that there is no definite clear relationship between AE spectral peak identification and the linear energy density. Each combination of process parameters produces a unique morphology of tracks and unique sound.

The FFT spectrum for the different laser powers had a similar shape with varying amplitude from 30 µm to 300 µm powder thickness. In Figure 65, for 300 µm the different laser power

spectrums' shapes almost seem to merge. This is possibly, due to the melt pool that loses contact with the substrate and cannot conduct heat away rapidly leading to similar melt pool dynamics for the different laser powers.

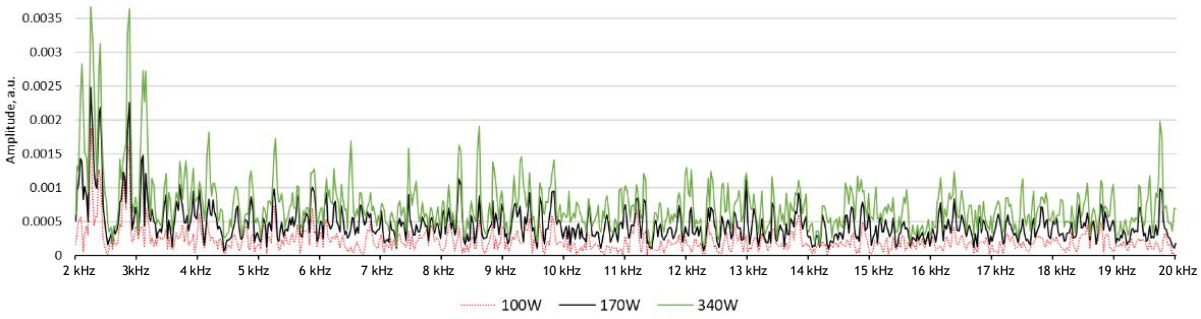

Figure 65: FFT spectrum single tracks with 300µm powder layer thickness at 100 W, 170 W and 340 W laser powers and 0.6 m/s scanning speed

Gas-borne AE results are reported for different layer thicknesses, laser powers and LPBF modes. From this data it is clear that track morphology cannot be used alone to correlate to AE, but one should consider the different combinations of process parameters. This information on the single tracks can be used to aid development of a monitoring system.

4.4 Recognition algorithms

At optimal process parameters, LPBF Ti6Al4V ELI samples can show very high density (>99.9%) and only randomly distributed small pores (Yadroitsev *et al.*, 2018). However, non-homogenous powder delivery or redistribution of the powder layer during processing of complex-shaped samples can cause too thick a layer of powder layer, or inversely, create areas without powder. In the case of a critically thick powder layer, there will not be metallurgical contact between the melt pool and the previous solidified layer/substrate. Laser processing of areas without powder will only result in re-melting of the previously solidified layer. When applying the subsequent powder layer, a thicker layer will be obtained, which can cause a balling effect. Early online detection of the unstable formation of single tracks due to these problems could prove to be an effective way of preventing porosity and other defects in LPBF-manufactured parts.

The present work analyzes the unique AE signatures at the formation of a single track with optimal process parameters as well as the identification of tracks manufactured on powder-free areas and thick powder layers. The simple algorithm and methodology demonstrated can

potentially be applied in-situ for correcting errors in a feedback control scheme, which is extremely important in manufacturing high-quality LPBF parts (Druzgalski *et al.*, 2020).

4.4.1 Layer thickness recognition algorithm 1

Measurements of the single tracks from the top view and their cross-sections showed that width and height of the tracks depend on the powder layer thickness, because it defines the amount of material involved in the process (Figure 66). The energy input was enough to fuse all powder under the laser beam and to penetrate into the substrate with a depth of about 70 µm. The conductive mode of the laser fusion promoted U-shaping of the molten pool when the selected process parameters were applied. Thus, tracks were different in width and height.

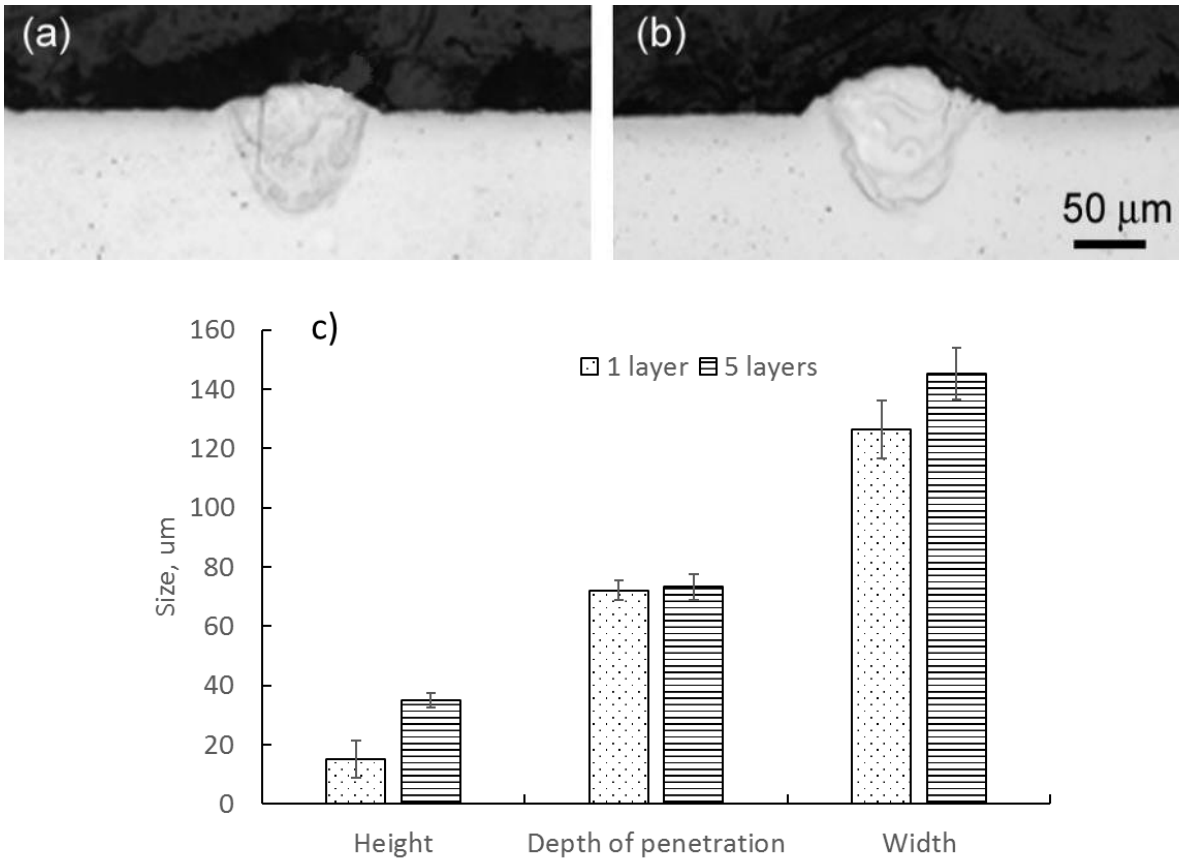

Figure 66: Cross-sections of single tracks: one layer (a), five layers (b) and their geometrical characteristics.

Figure 67 shows the signal obtained at frequencies between 2–50 kHz for the three tracks at each layer at the two different layer thicknesses. Signals were sampled at 100 kHz and according to the Nyquist rate, the maximum frequency measured can be 50 kHz. A 2 kHz high-pass filter was used to remove low-frequency environmental noise. The recorded signal indicated a strong correlation between the AE signal amplitude and the sequence of tracks. Since the low level of the signal shows a short pause between the scanning, this type of filtration

could also be used as one of the qualitative characteristics of the presence or absence of defects during LPBF.

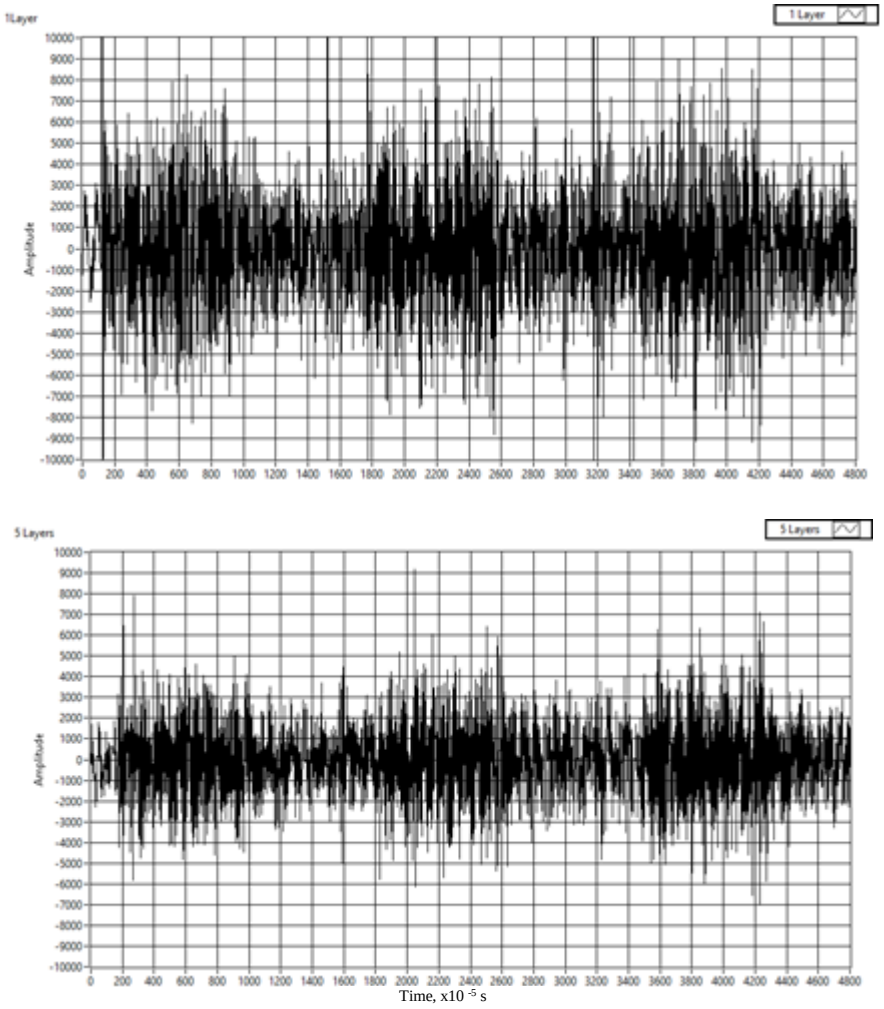

Figure 67: Signal registered for three scans after a 2 kHz high-pass filter: one layer (top) and five layers (bottom) with amplitude in a.u.

Figure 68 presents acoustic spectra of the first two tracks after FFT with threshold lines (red colour). A threshold is introduced to remove low energy components, which is always present in both, thus making it plausible to distinguish between differences in the models. The threshold near 70 000 for the one-layer model and 50 000 for the five-layer model was found to give the best correlation to the ground truth when it is 15% of the maximum value. The percentage is calculated from maximum to reduce the negative effect of slight changes in sound amplitude.

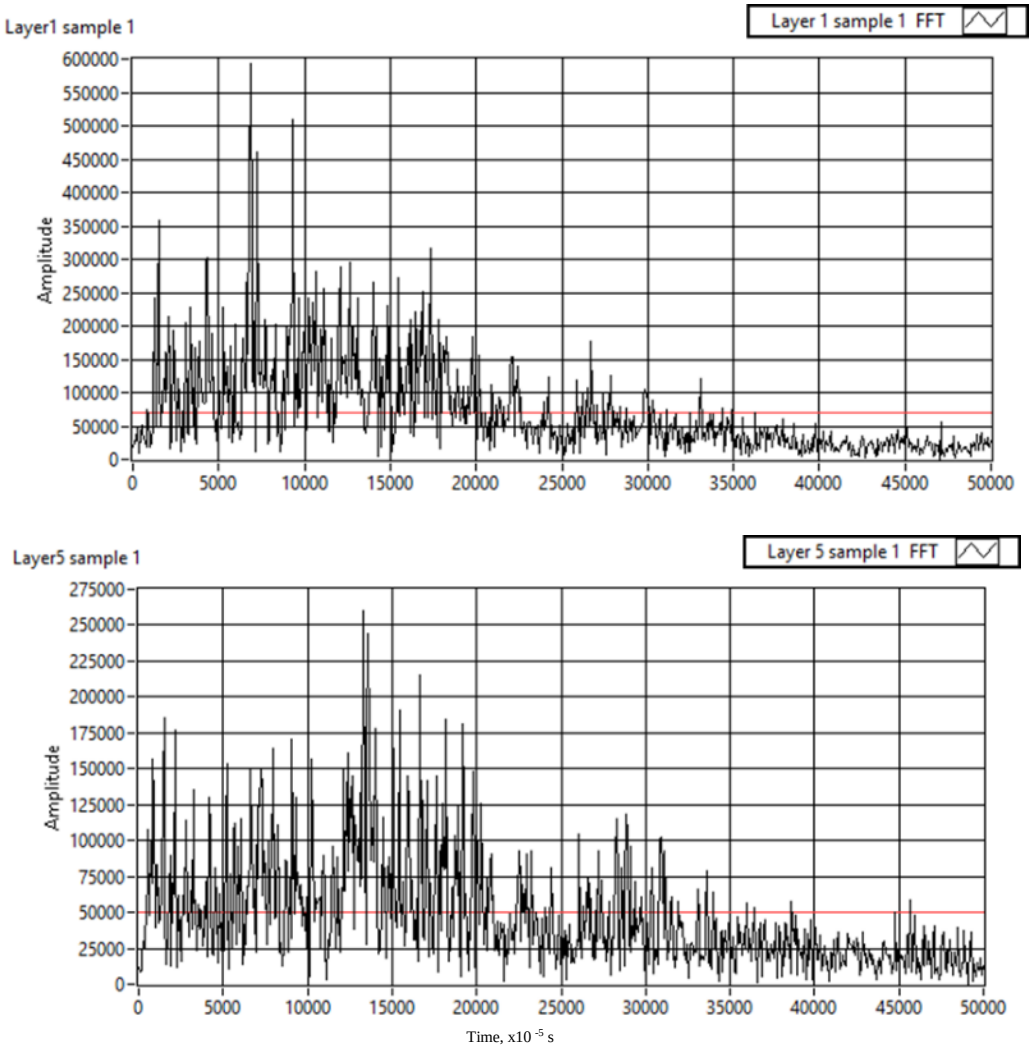

Figure 68: FFT spectra of AE from one layer (top) and five layers single tracks (bottom). Threshold value for FFT peak classification is indicated by red line.

The spectra from the five-layer tracks had more intensive high-frequency components. Probably, this was due to a higher temperature of the molten pool which resulted from a thicker powder layer. Since the powder has higher effective absorptivity than solid material, maximum temperature of the molten pool can be reached with the thicker powder layer. Another possible reason is the creation of the deeper channel in the melt pool for the generation of AE at higher layer thickness. Sparking effect can also be taken into account for future analysis.

To find significant difference in the frequency spectrum of the tracks, all frequencies present in the FFT above the threshold lines were recorded as “1” and the rest as “0”. This procedure normalizes the magnitude and gets rid of low energy components. The resulting classification of AE signals according to this criterion is shown in Figure 69.

Results of classifications for both layer thicknesses were combined (multiplied) to see what frequencies were presented in both models. The combined coded frequencies were subtracted

from the original signals to make a model that should only consist of the unique frequencies present for each powder layer thickness (Figure 70).

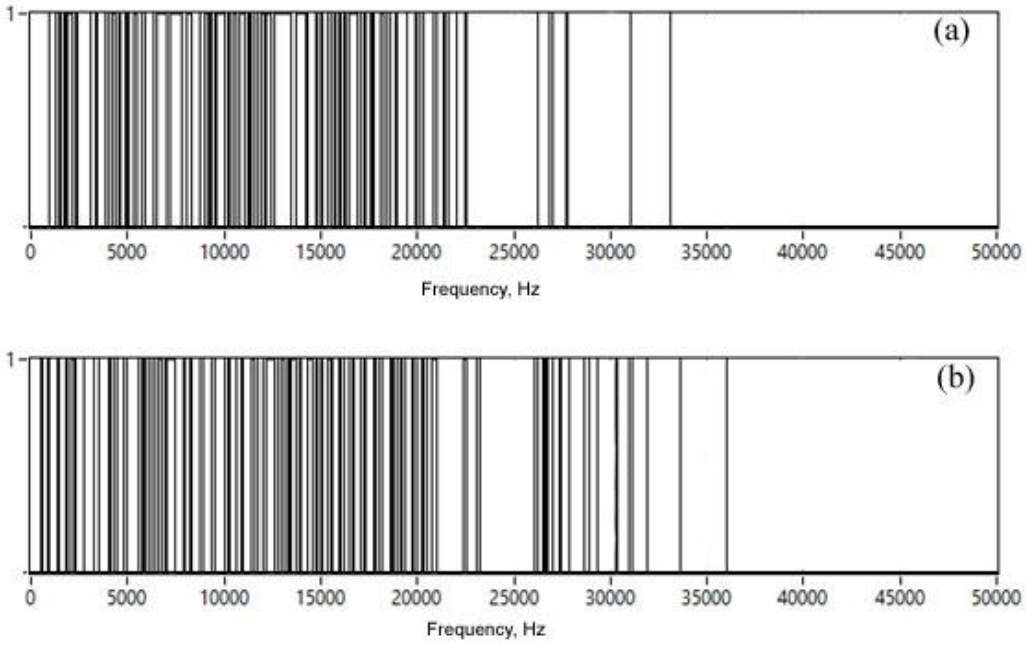

Figure 69: Coded FFT signals for the two tracks after classification: one layer (a) and five layers (b).

The third track of each sample that was not used in the generation of these models was then evaluated against the models to see whether the model could predict from which layer the track was produced. The evaluation tracks (third tracks) at one layer and five layers were subtracted from the model and then all the points added up. All the points of the one-layer and five-layer model were summed. The evaluation sum was then divided by the model sum as a percentage correlation corresponding to the model used. It was found that the one-layer track had 80% correlation with the one-layer model and only 50% correlation with the five-layer model. The five-layer track had 70.3% correlation with the five-layer model and only 52.2% correlation with model derived from the one-layer model.

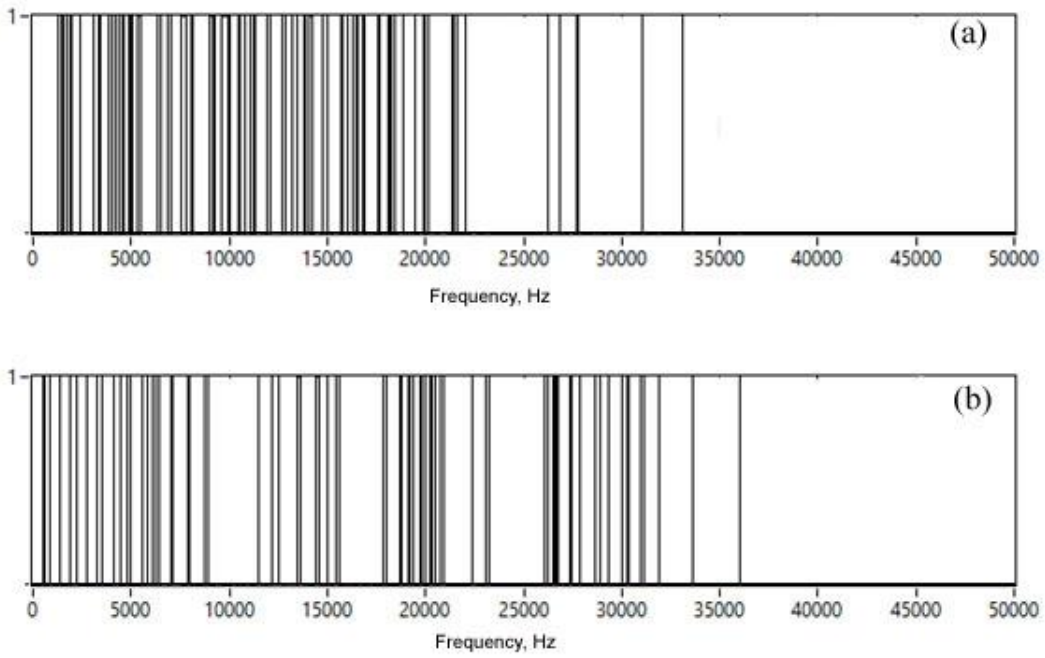

Figure 70: Coded signals for the two tracks after classification: one layer (a) and five layers (b).

As was indicated, tracks were manufactured at the same process parameters but at different powder layer thicknesses. Differences were found in the width of molten pool and the track height. Changes in the powder layer can occur when the previously sintered layer was very rough and keyhole or balling started. The newly delivered layer will be inhomogeneous and thick. The proposed approach can be useful in the prediction of a larger molten pool when more powder material is involved in the process. The high-frequency band at 25–35 kHz with enhanced AE from the molten pool looks promising for defect detection.

The typical AE frequency bands for different process parameters when keyhole or balling effect arises can be determined and used for in-process monitoring and spatial recognition of defects. A real-time monitoring AE system could be realized using these models. This real-time monitoring AE system could be achieved using the 1's and 0' of the models, seen in Figure 69 and Figure 70 as pole, zero placement in the real-time filter design.

4.4.2 Layer thickness recognition algorithm 2

This section only considers audible sound. FFT for AE signals from three sets of ten tracks, each with a length of 90 mm produced at 170 W and 1.2 m/s scanning speed, shows similar results. The case without a powder layer showed low AE, especially at a higher frequency; about 50% of signal strength was concentrated between 2–7 kHz (Figure 71). There is a clear

corresponding rise in cumulative amplitude of AE signals after 6 kHz with layer thickness. These types of indicators can be used to develop online monitoring identifiers. Analysis of SPL and dominant FFT frequencies averaged over the entire signal time intervals suggested that the AE signal can correlate with processed layer thickness and with the size of the melt pool.

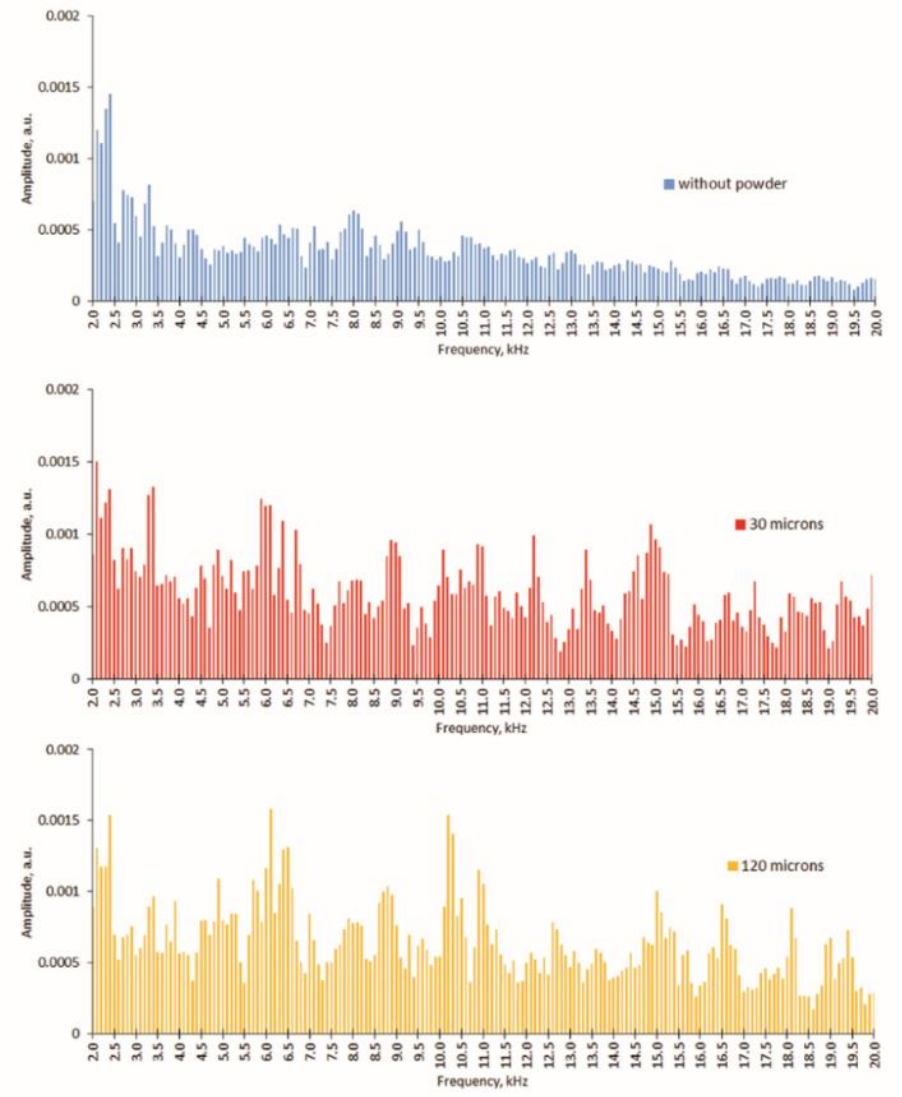

Figure 71: FFT spectra and average intensity of AE signals for 10 single tracks produced without powder, 30 μm and 120 μm powder layer thickness.

In the present experiments, the spatter effect increased with powder layer thickness and corresponds with the SPL and frequency changes. No spattering was observed without powder (Figure 72).

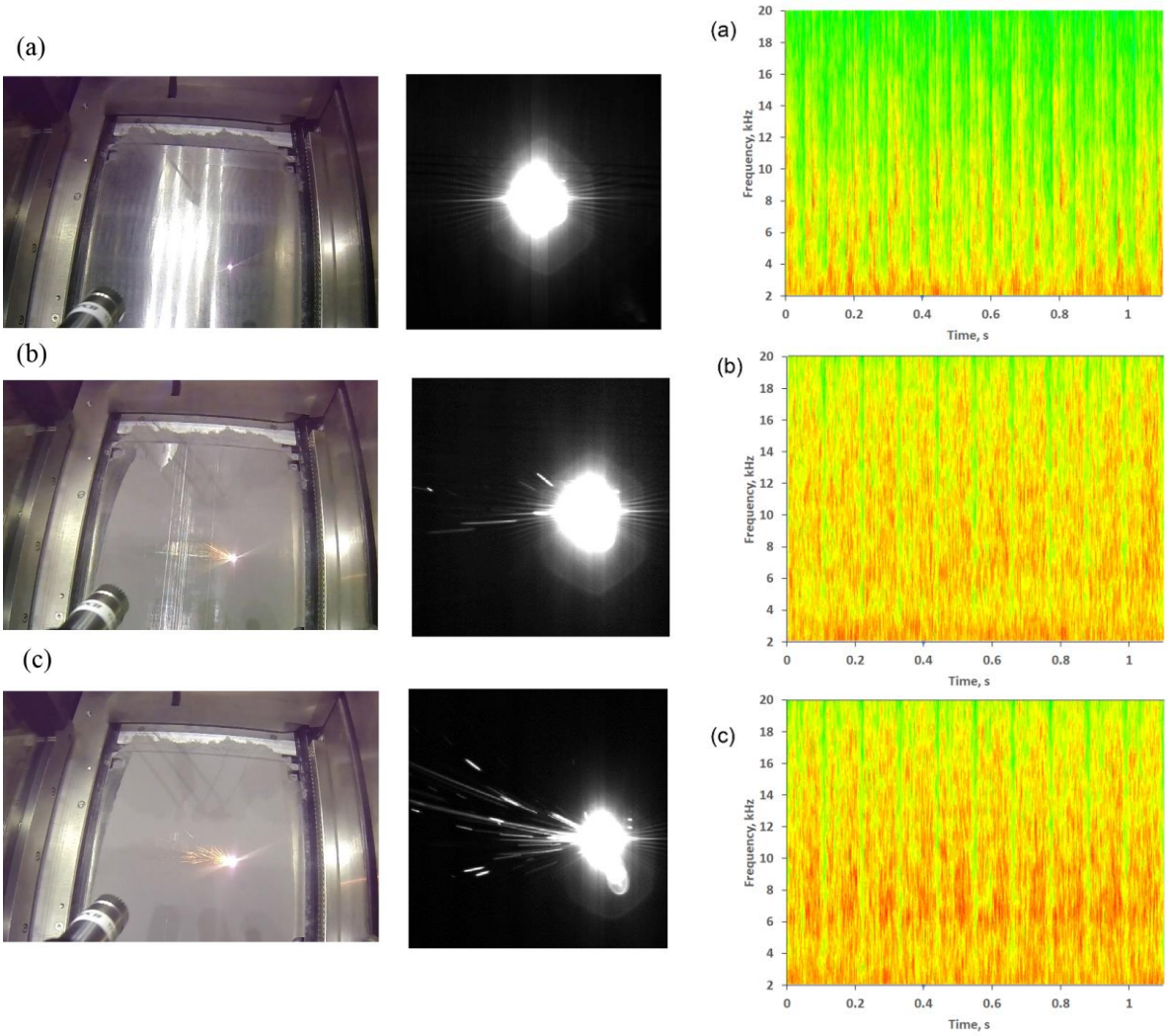

Figure 72: Images of scanning of 10 sequential, non-overlapping tracks at different layer thicknesses (scanning direction from left to right) with layer thickness: (a) no powder, (b) and (c) with powder: 30 μm powder layer and 120 μm powder layer, correspondingly. Spectrograms of the scans showing increasing intensity of AE signal (right). The colour indicates amplitude: green is low values and red is higher values

In the case without powder, the SNR value was -10.185 dB, for one layer of powder (30 μm) and the thick layer of 120 μm, or for "optimal" and "non-optimal" conditions it was -4.731 dB and -3.688 dB, respectively which indicates that the signal strength increases with thicker powder layers. In general, due to the high variability of the amplitudes, it was difficult to find a correlation between the dominant frequencies and the thickness of the layer at the 2–20 kHz range in these studies (Figure 72). Apparently, the main sign of an increase in the layer thickness and the associated balling effect is the presence of high amplitudes in the spectrum at frequencies of 6–10 kHz, but this assumption should be investigated on a larger number of single tracks forming a single layer. FTT amplitudes of single tracks varied significantly with

time during processing, so STFT was used to evaluate the effect of powder layer thickness on the AE process.

Summing up all the SFFT values at individual frequencies over time can indicate how much of each frequency was present as AE signal for each powder thickness (without powder, 30 µm, 120 µm), Figure 73a. The proposed layer recognition algorithm works by creating a signature for each deviation from reference signal, one signature for the deviation from "reference-to-no-powder layer" and another signature for the deviation from "reference-to-thick powder layer".

The amplitude A_f for each frequency f was calculated as

$$A_f = \sum_{t=0}^{T-1} STFF_{t,f} \quad (1)$$

and then it was scaled to [-1; 1] by equation (2):

$$AScaled_f = \frac{A_f - 0.5\,(MAX(A_f) - MIN(A_f))}{0.5\,(MAX(A_f) - MIN(A_f))} \quad (2)$$

Each set of track data was subtracted from the reference set to obtain the two signature/characteristic curves: "reference layer" minus "no powder layer" and "reference layer" minus "thick powder layer". The characteristic difference ΔA_f in amplitudes for each frequency is calculated by:

$$\Delta A_f = ARefScaled_f - ATestScaledA_f \quad (3)$$

The results of the two signature/characteristic curves for the thick powder layer and scanning without powder calculated from Equation 2 are shown in Figure 73c. The signature/characteristic curves c were used in the algorithm to test the remaining tracks. This was done by subtracting the new AE signal from the reference signal and correlating the answer to the two signature curves ("reference–no powder" and "reference–thick layer"), Figure 73.

For the quantitative data comparison algorithm, normalized correlation between the remaining set of tracks and the two characteristic curves from the model were calculated by:

$$C = \frac{1}{\sqrt{ETest \times EModel}} \sum_f \Delta AModel_f \times \Delta AModel_f \quad (4)$$

Where

$$EModel = \sum_{f} |\Delta AModel_f|^2 \qquad ETest = \sum_{f} |\Delta ATest_f|^2 \tag{5}$$

The models showed high correlation values: >0.8 for the “reference–no powder” model and >0.6 for the thick powder layer (Table 14). The reference tracks showed very low correlation with either model, as expected.

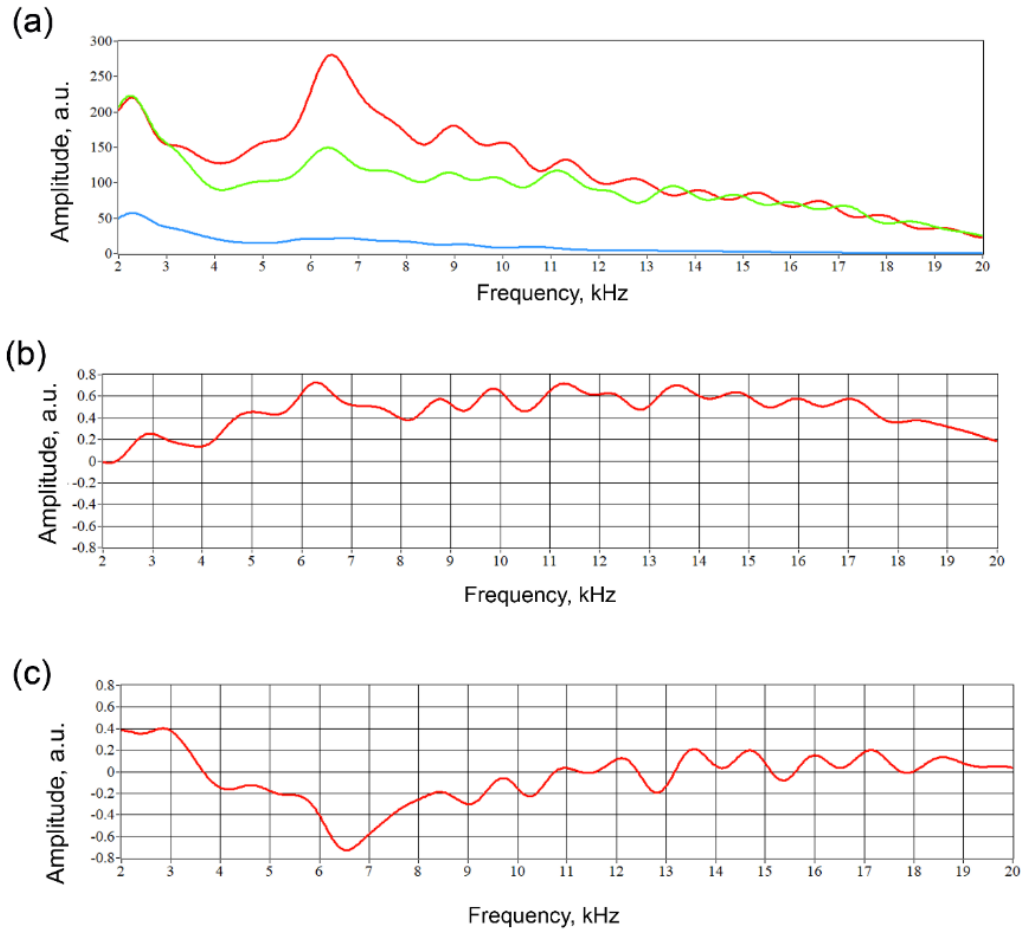

Figure 73: Cumulative amplitude of AE signals for six tracks in different sets: no powder (blue colour), one layer (30 µm as reference, green colour) and four layers (120 µm, red colour) of powder thickness (a). Signature curves of “reference powder layer–no powder” (b) and “reference-thick powder layer” (c).

To implement this approach for online monitoring by AE, the recorded sound must be compared to both the models. Low correlation to either model means that the process is stable and defect-free. High correlation with the "no powder" model indicates that tracks were processed with lower powder thickness than expected. This will increase the probability of thick powder being present on the next layer. High correlation with the "thick powder layer" model indicates a high probability of balling effect and subsequent lack-of-fusion porosity in

the corresponding area of the part. Additionally, other types of defect signatures can potentially be created and added to expand the type of defects which the system can recognize).

Table 14: Correlation coefficients for experiments with single tracks

		"Reference–no powder" model	"Reference–thick powder layer" model
No powder	Tracks 1–6	**1**	0.087
	Track 7	**0.867**	0.078
	Track 8	**0.936**	0.079
	Track 9	**0.926**	0.081
	Track 10	**0.873**	0.071
Reference thickness (30 µm)	Track 7	0.340	0.122
	Track 8	0.034	0.135
	Track 9	0.000	0.202
	Track 10	0.000	0.415
Thick (critical) powder layer (120 µm)	Tracks 1–6	0.087	**1**
	Track 7	0.093	**0.801**
	Track 8	0.116	**0.779**
	Track 9	0.163	**0.683**
	Track 10	0.218	**0.713**

The same steps were used to create and test the algorithm for the layers. The results appear to be similar in that: the AE energy increases with powder layer thickness; the same peaks are present at ~6 to 8kHz and for no powder the energy is low at higher frequencies (Figure 74).

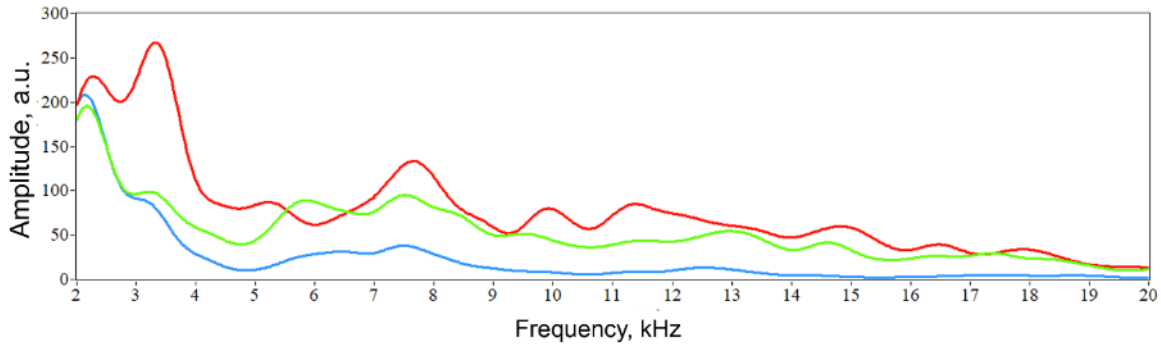

Figure 74: Cumulative amplitude of AE signals for single layers in different sets of powder thickness: one layer (30 µm as reference, green colour), four layers (120 µm, red colour), and without powder (blue colour)

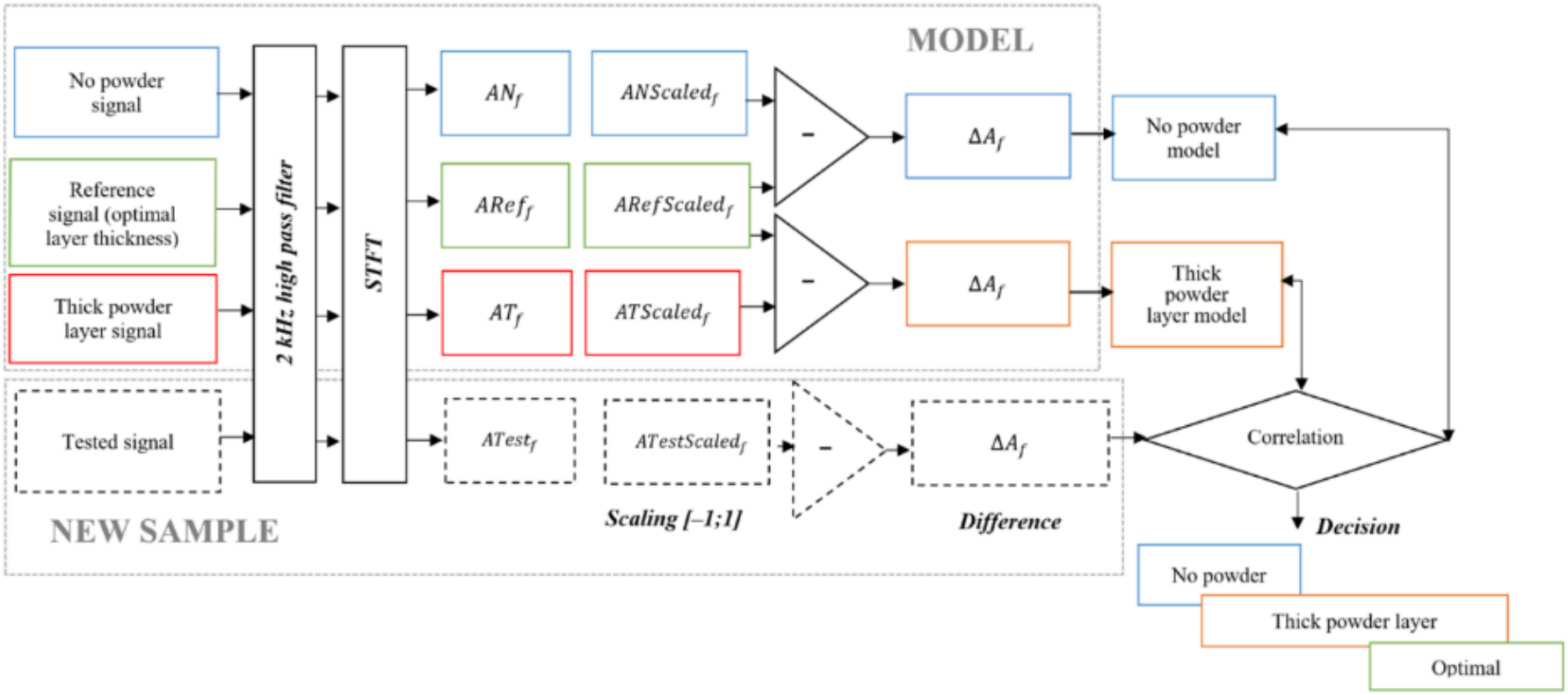

Figure 75: Flowchart for recognition of layer thickness by AE signals

One notable difference between single tracks and single layers is observed for no powder. At 60 µm and 120 µm there is an increased amplitude at ~3.5 kHz. This can be due to an increase in local heating and in the regular change of the denudation zone in the manufacturing of a sequence of tracks, i.e. layer, which is absent in the manufacture of single track (Yadroitsev and Smurov, 2011). The layers correlated very well with the two models (Table 15). Correlation values of the reference thickness showed some correlation to "reference–no powder" model. The threshold for the layers can be set as high as 0.9 to warn the system of a defect powder layer.

Table 15: Correlation coefficients for experiments with single layers

		"Reference–no powder" model	"Reference–thick powder layer" model
No powder	Model	**1**	0.017
	Test layer	**0.996**	0.020
Reference thickness (30 µm)	Test layer	0.469	0.103
Thick (critical) powder layer (120 µm)	Model	0.017	**1**
	Test layer	0.042	**0.947**

4.4.3 Summary

A detailed analysis of airborne AE signals for LPBF of single tracks is presented. Track morphology at different layer thickness and laser powers are compared to AE signals. The results show that a simple algorithm could accurately identify problematic situations where the thickness of the powder layer is irregular: it can identify between cases when there is no powder, reference powder layer and thick powder layer (lack of fusion) when the balling effect starts, and when tracks are irregular in shape.

CONCLUSIONS AND FUTURE RESEARCH

Manufacturing components for industries where quality is crucial requires that the parts be tested before being commissioned into service. "*How does the quality compare to that of conventional manufacturing methods?*" Manufacturing standards and testing procedures need to be in place to give the end-user peace of mind. When new technologies emerge, formal issued standards always lag, which hinder technology growth. Each alloy has a unique processing window within which optimal tracks are produced. Literature shows that many researchers are looking to develop optimal process parameters for new materials. Parallel to this, companies and researchers are developing machines and equipment to enhance the capabilities and quality of LPBF, real-time control using online monitoring being one of the major drives seen from LPBF platform suppliers. Quality of aerospace and medical components must be verified. Current methods depend much upon post-processing methods such as CT scanning. Post-processing is time-consuming and adds significant cost to the parts being produced. The nature of adding single tracks to form layers which are then added to form 3D parts exhibits specific defects and material properties. It is, therefore, very important to understand LPBF, design for AM and the capabilities of the online monitoring equipment (probability of detection).

Intricacies of defects are dependent on many factors: material, build orientation, layer thickness, geometry, laser parameters, etc. All these factors interplay making it difficult to predict the type of defect that might arise; this is also why the idea of creating a digital twin is currently receiving much attention from the AM community. Single track morphology under different process parameters is shown. The critical layer thickness for lack-of-fusion porosity was found for the 3D objects and correlated well to the shape of the single track.

Regarding online monitoring, gas-borne AE is relatively easy to implement, inexpensive and able to give valuable information. For online monitoring the current equipment, microphone placement, scanning position and signal filtering were verified for the M280 environment. Online AE can distinguish events within the time domain. The AE during the LPBF process presented promising results in that it changes with the powder thickness, laser power and laser operating modes. Track morphology at different layer thicknesses and laser powers were compared to their corresponding AE signals. Different combinations of process parameters yielded different acoustic signals. When comparing different parameters, tracks might look the same and even be processed with equal energy density but yield a completely different acoustic

signal, therefore, track morphology alone cannot be used to correlate to AE; one should consider a process parameter set.

A detailed analysis of airborne AE signals of single tracks and layers were presented. Determining the typical AE frequency bands for different process parameters when keyhole or balling effect arise can be used for in-process monitoring and spatial recognition of defects in LPBF manufacturing. The results show that a simple algorithm could accurately identify problematic situations where the thickness of the powder layer is irregular – it can identify between cases when there is no powder, optimal powder and a thick powder layer (lack of fusion) when balling starts, and when tracks are irregular in shape. These post-processing algorithms can be used in the design of online process monitoring of LPBF. As shown in this study, changes in layer thickness have a great effect on AE. The SPL and spectral analysis can, therefore, be used to identify keyhole mode or lack-of-fusion defect scenarios. This AE approach can possibly be implemented using a device such as a Field Programmable Gate Arrays (FPGA). A FPGA can record new data and do signal processing simultaneously. The correlation values can then be used to interrupt the building process.

The complex nature of the LPBF process leaves much space for investigation of the sources of AE and how each parameter may affect the signal along with the limitations. The limit of the smallest thickness deviation that this method can detect should be investigated. Future work involves finding what information might be hidden within the machine noise (0–2 kHz) and using other signal processing tools. To develop an online monitoring method, further research is needed to determine how other factors can change the sound emitted during the LPBF process. For example, factors like laser modulation, scanning strategies which influence melt pool temperature and part geometry containing overhang areas could also affect this. The proposed algorithms can be fine-tuned and extended to include different events other than layer thickness. This approach can then be integrated with the software to either alarm or adapt system parameters when AE does not correlate to the required reference values.

Future work can include investigating other AE systems such as air-coupled ultrasound and other signal processing methods such as using other linear time invariant algorithms with the identified frequencies. Establishing the limitations of AE online monitoring, i.e. minimum size and the typical defects, will assist as a quality control method for LPBF components. AE data in combination with x-ray CT can be used to develop a digital twin for production parts. The establishment of standards in terms of what type of defects are allowed would assist not only the end-users but also the development of online monitoring systems, because these systems

are considered with respect to the probability of detection. AE might be a valuable missing complementary tool in online monitoring systems.

References

3D Systems, 2020. DMP Inspection (Online) Available from: https://www.3dsystems.com/dmpinspection (Accessed on 18 August, 2020).

Abbasi, Z., Yuhas, D., Zhang, L., Basantes A-D-C., Tehrani, NN., Ozevin, D., Indacochea, E., 2018. The Detection of Burn-Through Weld Defects Using Noncontact Ultrasonics. Materials. 11(1), p.128. https://doi.org/10.3390/ma11010128

Agius, D., Kourousis, K.I. and Wallbrink, C., 2018. A review of the as-built SLM Ti-6Al-4V mechanical properties towards achieving fatigue resistant designs. Metals, 8(1), p. 75.

Alfaro, S.C.A. and Cayo, E.H., 2012. Sensoring fusion data from the optic and acoustic emissions of electric arcs in the GMAW-S process for welding quality assessment. Sensors, 12(6), pp. 6953–6966.

Al-Obaidi, S.M.A., Leong, M.S., Hamzah, R.I.R. and Abdelrhman, A.M., 2012. A review of acoustic emission technique for machinery condition monitoring: defects detection & diagnostic. Applied Mechanics and Materials. 229–231, pp. 1476–1480.

Aloisi, V. and Carmignato, S., 2016. Influence of surface roughness on X-ray computed tomography dimensional measurements of additive manufactured parts. Case Studies in Nondestructive Testing and Evaluation, 6 (B), pp. 104–110.

Alton, F. and Everest, P., 2009. Master handbook of acoustics. 5th ed. McGraw Hill ISBN 978-0-07-160332-4, New York, 2009.

ASTM F2792-12a, Standard Terminology for Additive Manufacturing Technologies, (Withdrawn 2015), ASTM International, West Conshohocken, PA, 2012.

ASTM F3001-14, Standard Specification for Additive Manufacturing Titanium-6 Aluminum-4 Vanadium ELI (Extra Low Interstitial) with Powder Bed Fusion, ASTM International, West Conshohocken, PA, 2014, www.astm.org https://doi.org/10.1520/F3001-14

ASTM, 2020. Committee F42 on Additive Manufacturing Technologies. (Online) Available from: https://www.astm.org/COMMITTEE/F42.htm (Accessed on 19 Jan, 2020).

Bartlett, J.L. and Li, X., 2019. An overview of residual stresses in metal powder bed fusion. Addit. Manuf. 27, pp. 131–149. https://doi.org/10.1016/j.addma.2019.02.020

Beretta, S., Gargourimotlagh, M., Foletti, S., du Plessis, A. and Riccio, M., 2020. Fatigue strength assessment of “as built” AlSi10Mg manufactured by SLM with different build orientations. Int. J. Fatigue. 139. https://doi.org/10.1016/j.ijfatigue.2020.105737

Berumen, S., Bechmann, F., Lindner, S., Kruth, J.P. and Craeghs, T., 2010. Quality control of laser- and powder bed-based Additive Manufacturing (AM) technologies. Physics Procedia, 5, pp. 617–622.

Bidare, P., Bitharas, I., Ward, R.M., Attallah, M.M. and Moore, A.J., 2018. Fluid and particle dynamics in laser powder bed fusion. Acta Mater. 142, pp. 107–120. https://doi.org/10.1016/j.actamat.2017.09.051

Bidare, P., Bitharas, I., Ward, R.M., Attallah, M.M. and Moore, A.J., 2018a. Laser powder bed fusion at sub-atmospheric pressures. International Journal of Machine Tools and Manufacture. 130–131, pp. 65–72. https://doi.org/10.1016/j.ijmachtools.2018.03.007

Bikas, H., Stavropoulos, P. and Chryssolouris, G., 2016. Additive manufacturing methods and modelling approaches: a critical review. The International Journal of Advanced Manufacturing Technology, 83(1–4), pp. 389–405.

Boley, C. D., Mitchell, S. C., Rubenchik, A. M. and Wu, S. S. Q., 2016. Metal powder absorptivity: modeling and experiment. Applied Optics, 55(23), pp. 6496–6500. https://doi.org/10.1364/ao.55.006496

Bono, R. and Sorensen, S., 2008. Resonant acoustic method delivers defect-free parts. Advanced Materials & Processes, 166(7), pp.25–28.

Bono, R.W. and Stultz, G., 2010. Automated resonant inspection to validate resonant frequency characteristics within brake components for improved NVH Performance (No. 2010-01-1699). SAE Technical Paper.

Bono, R.W., Schiefer, M.I. and Stultz, G.R., 2007. Resonant inspection as an automated NDT method for sinter brazed powder metal components, SAE International, 2007.

Bono, R.W., Sorensen, S.A. and Stultz, G.R., 2010. New methodology applying resonant inspection for quality testing of very small powder metal components. International Conference on Powder Metallurgy & Particulate Materials, June 27–30, 2010, Hollywood, Florida.

Bordatchev, E. V. and Nikumb, S.K., 2006. Effect of focus position on informational properties of acoustic emission generated by laser-material interactions. Appl. Surf. Sci. 253, 1122–1129. https://doi.org/10.1016/j.apsusc.2006.01.047

Cai, C., Song, B., Xue, P., Wei, Q., Wu, J.M., Li, W. and Shi, Y., 2016. Effect of hot isostatic pressing procedure on performance of Ti6Al4V: Surface qualities, microstructure and mechanical properties. J. Alloys Compd. 686, pp. 55–63. https://doi.org/10.1016/j.jallcom.2016.05.280

Carino, N.J., 2013. Training: Often the missing link in using NDT methods. Construction and Building Materials, 38, pp. 1316–1329.

Cerna, M. and Harvey, A.F., 2000. The fundamentals of FFT-based signal analysis and measurement. National Instruments, Junho, p. 54.

Charde, N., Ahmad, R. and Abidin, N.I.Z. 2016. Interpreting the weld formations using acoustic emission for the carbon steels and stainless steels welds in servo-based resistance spot welding. The International Journal of Advanced Manufacturing Technology, 86 (1–4), pp. 1–8.

Chen, X., 2014. Computational and experimental approach for non-destructive testing by laser shearography. Doctoral dissertation, University of Zaragoza, Spain.

Clough, R. B. The energetics of acoustic emission source characterization, Materials Evaluation, Vol. 45, 1987, pp. 556–63.

Craeghs, Tom, Clijsters, Stijn, Yasa, Evren and Kruth, Jean-Pierre., 2011. Online quality control of selective laser melting. 22nd Annual International Solid Freeform Fabrication Symposium – An Additive Manufacturing Conference, SFF 2011.

CRPM, 2020. Centre for Rapid Prototyping and Manufacturing. (Online) Available from: http://www.crpm.co.za/#about (Accessed on 18 June, 2020).

de Beer, D., du Preez, W., Greyling, H., Prinsloo, F., Sciammarella, F., Trollip, N., Vermeulen, M. and Wohlers, T., 2016. A South African additive manufacturing strategy. (Online) Available from: https://www.dst.gov.za/index.php/resource-center/strategies-and-reports/2629-a-south-african-additive-manufacturing-strategy (Accessed on 18 June, 2020).

De Chiffre, L., Carmignato, S., Kruth, J.P., Schmitt, R. and Weckenmann, A., 2014. Industrial applications of computed tomography. CIRP Annals-Manufacturing Technology, 63(2), pp. 655–677.

DebRoy, T., Mukherjee, T., Milewski, J.O., Elmer, J.W., Ribic, B., Blecher, J.J. and Zhang, W., 2019. Scientific, technological and economic issues in metal printing and their solutions. Nat. Mater. 18, pp. 1026–1032. https://doi.org/10.1038/s41563-019-0408-2

DebRoy, T., Wei, H.L., Zuback, J.S., Mukherjee, T., Elmer, J.W., Milewski, J.O., Beese, A.M., Wilson-Heid, A. and De, A., Zhang, W., 2018. Additive manufacturing of metallic components – Process, structure and properties. Prog. Mater. Sci. 92, pp. 112–224. https://doi.org/10.1016/j.pmatsci.2017.10.001

Design for Additive Manufacturing, 2020. Elsevier. https://doi.org/10.1016/C2017-0-04238-6

Dordlofva, C., Borgue, O., Panarotto, M. and Isaksson, O., 2019. Drivers and guidelines in design for qualification using additive manufacturing in space applications. Proceedings of the Design Society: International Conference on Engineering Design, 1(1), pp. 729–738. https://doi.org/10.1017/dsi.2019.77

Druzgalski, C.L., Ashby, A., Guss, G., King, W.E., Roehling, T.T., Matthews, M.J., 2020. Process optimization of complex geometries using feed forward control for laser powder bed fusion additive manufacturing. Addit. Manuf. 101169. https://doi.org/10.1016/j.addma.2020.101169

Dryburgh, P., Patel, R., Pieris, D.M., Hirsch, M., Li, W., Sharples, S.D., Smith, R.J., Clare, A.T. and Clark, M., 2019. Spatially resolved acoustic spectroscopy for texture imaging in powder bed fusion nickel superalloys, in: AIP Conference Proceedings. American Institute of Physics Inc., p. 020004. https://doi.org/10.1063/1.5099708

du Plessis, A., Broeckhoven, C., Guelpa, A. and Le Roux, S.G., 2017. Laboratory X-ray micro-computed tomography: a user guideline for biological samples. GigaScience, 6(6), pp. 1–11.

du Plessis, A., Broeckhoven, C., Yadroitsava, I., Yadroitsev, I., Hands, C.H., Kunju, R., Bhate, D., 2019. Beautiful and functional: A review of biomimetic design in additive manufacturing. addit. manuf. 27, pp. 408–427. https://doi.org/10.1016/j.addma.2019.03.033

du Plessis, A., Le Roux, S.G. and Guelpa, A., 2016. The CT Scanner Facility at Stellenbosch University: An open access X-ray computed tomography laboratory. Nuclear Instruments and Methods in Physics Research Section B: Beam Interactions with Materials and Atoms, 384, pp. 42-49.

du Plessis, A., Le Roux, S.G., Booysen, G. and Els, J., 2016a. Directionality of cavities and porosity formation in powder-bed laser additive manufacturing of metal components investigated using X-ray tomography. 3D Printing and Additive Manufacturing, 3(1), pp. 48–55.

du Plessis, A., Le Roux, S.G., Booysen, G. and Els, J., 2016b. Quality control of a laser additive manufactured medical implant by X-ray tomography. 3D Printing and Additive Manufacturing 3 (3), pp. 175–182.

. and Macdonald, E., 2020. Hot isostatic pressing in metal additive manufacturing: X-ray tomography reveals details of pore closure. Addit. Manuf. 34. https://doi.org/10.1016/j.addma.2020.101191

du Plessis, A., Seifert, T., Booysen, G. and Els, J., 2014. Microfocus X-ray computed tomography (CT) analysis of laser sintered parts. The South African Journal of Industrial Engineering, 25(1), pp. 39–49.

du Plessis, A., Yadroitsava, I. and Yadroitsev, I., 2020. Effects of defects on mechanical properties in metal additive manufacturing: A review focusing on X-ray tomography insights. Mater. Des. 187. https://doi.org/10.1016/j.matdes.2019.108385

du Plessis, A., Yadroitsev, I., Yadroitsava, I. and Le Roux, S.G., 2018. X-ray microcomputed tomography in additive manufacturing: A review of the current technology and applications. 3D Print. Addit. Manuf. 5, pp. 227–247. https://doi.org/10.1089/3dp.2018.0060

Duley, W.W. and Mao, Y.L., 1994. The effect of surface condition on acoustic emission during welding of aluminium with CO2 laser radiation. J. Phys. D. Appl. Phys. 27, pp. 1379–1383. https://doi.org/10.1088/0022-3727/27/7/007

École Polytechnique Fédérale de Lausanne, 2018. Digital Signal Processing (Online) Available from: https://www.coursera.org/learn/dsp#ratings (Accessed on 21 November, 2018).

EOS GmbH, 2020. Additive Manufacturing (Online) Available from: http://www.eos.info/ (Accessed on 14 March, 2020).

EOS Training Manual, 2012. Basic Training EOSINT M280, Edition: 04.12, Article number: 9229-3501.

Errede, S. (2017) The human ear-hearing, sound intensity and loudness levels (2002–2015). Department of Physics, University of Illinois at Urbana-Champaign, Illinois, pp. 1–34.

Eschner, N., Weiser, L., Häfner, B. and Lanza, G., 2018. Development of an acoustic process monitoring system for the selective laser melting (SLM), in: Solid Freeform Fabrication Symposium. pp. 2097–2117.

Everton, S.K., Hirsch, M., Stravroulakis, P., Leach, R.K. and Clare, A.T., 2016. Review of in-situ process monitoring and in-situ metrology for metal additive manufacturing. Materials & Design, 95, pp. 431–445.

Fisher, K.A., Candy, J.V., Guss, G. and Mathews, J.M., 2016. Evaluating acoustic emission signals as an in situ process monitoring technique for selective laser melting (SLM) (No. LLNL-TR-706659). Lawrence Livermore National Laboratory (LLNL), Livermore, CA.

Fogagnolo, J.B., Sallica-Leva, E., Lopes, E., Jardini, A.L. and Caram, R., 2012. The effect of the laser process-parameters in the microstructure and mechanical properties of Ti-6Al-4V produced by selective laser sintering/melting, Proceedings of METAL 2012, Brno, Czech Republic, 23–25 May, 2012.

Gaja, H. and Liou, F., 2017. Defects monitoring of laser metal deposition using acoustic emission sensor. Int. J. Adv. Manuf. Technol. 90, pp. 561–574. https://doi.org/10.1007/s00170-016-9366-x

GE Additive, 3D-Printed Joints & Implants: 100,000 Patients Later, The 3D-Printed Hip Is A Decade Old And Going Strong, (online) Available From: https://www.ge.com/additive/stories/3d-printed-joints-implants-100000-patients-later-3d-printed-hip-decade-old-and-going-strong (Accessed 16 July, 2021).

GE Oil & Gas, phoenix v|tome|x L300, (Online) Available from: https://www.bakerhughesds.com/inspection-technologies/radiography-ct/x-ray-computed-tomography/phoenix-vtomex-l-300 (Accessed 3 August, 2020).

Gold, S.A. and Spears, T.G., 2018. Acoustic monitoring method for additive manufacturing processes. https://patents.google.com/patent/US9989495B2/en?oq=US+9989495+B2

Grasso, M. and Colosimo, B.M., 2017. Process defects and in situ monitoring methods in metal powder bed fusion: a review. Meas. Sci. Technol. 28, 044005. https://doi.org/10.1088/1361-6501/AA5C4F

Gu, H. and. Duley, W.W. Resonant acoustic emission during laser welding of metals. J. Phys. D: Appl. Phys. Vol. 29, 1999, pp. 550–555.

Gu, D.D., Meiners, W., Wissenbach, K. and Poprawe, R., 2012. Laser additive manufacturing of metallic components: materials, processes and mechanisms. Int. Mater. 57, pp. 133–164. https://doi.org/10.1179/1743280411Y.0000000014

Gu, H. and Duley, W.W., 2018. Acoustic emission and optimized CO2 laser welding of steel sheets, in: International Congress on Applications of Lasers & Electro-Optics. Laser Institute of America, pp. 77–85. https://doi.org/10.2351/1.5058866

Hall, L.D., 2016. WO2016198885A1 – Additive manufacturing apparatus and method – Google Patents. L.D. Hall, https://patents.google.com/patent/WO2016198885A1/en) (Accessed on 17 June, 2020).

Hauk, V. ed., 1997. Structural and residual stress analysis by nondestructive methods: Evaluation-Application-Assessment. Elsevier.

Hellier, C. J., 2012. Handbook of nondestructive evaluation, 2nd ed., Mcgraw-Hill, USA.

Hirsch, M., Patel, R., Li, W., Guan, G., Leach, R.K., Sharples, S.D. and Clare, A.T., 2017. Assessing the capability of in-situ nondestructive analysis during layer based additive manufacture. Additive Manufacturing, 13, pp. 135–142.

Hooper, P. A., 2018. Melt pool temperature and cooling rates in laser powder bed fusion. Additive Manufacturing, 22, pp. 548–559. https://doi.org/10.1016/J.ADDMA.2018.05.032

Horvat, J., Prezelj, J., Polajnar, I. and Čudina, M., 2011. Monitoring gas metal arc welding process by using audible sound signal. Strojniški vestnik-Journal of Mechanical Engineering, 57(3), pp. 267–278.

IMCE, 2020 (Online) Available from: Imce http://Www.Imce.eu (Accessed on 8 July, 2020).

ISO, 2020. Technical committees ISO/TC 261 Additive Manufacturing. (Online) Available from: https://committee.iso.org/home/tc261 (Accessed on 18 June, 2020).

Kacaras, A., Bächle, M., Schwabe, M., Zanger, F., León, F.P. and Schulze, V., 2019. Acoustic emission-based characterization of focal position during ultra-short pulse laser ablation, in: Procedia CIRP. Elsevier B.V., pp. 270–275. https://doi.org/10.1016/j.procir.2019.03.047

Karme, A., Kallonen, A., Matilainen, V.P., Piili, H. and Salminen, A., 2015. Possibilities of CT scanning as analysis method in laser additive manufacturing. Physics Procedia, 78, pp. 347–356.

Khairallah, S.A., Anderson, A.T., Rubenchik, A. and King, W.E., 2016. Laser powder-bed fusion additive manufacturing: Physics of complex melt flow and formation mechanisms of pores, spatter, and denudation zones. Acta Materialia, 108, pp. 36–45.

Kim, F.H., Moylan, S.P. and Villarraga-Gómez, H., 2016. Inspection of embedded internal features in additively manufactured metal parts using metrological x-ray computed tomography. 2016 Summer Topical Meeting: Dimensional Accuracy and Surface Finish in Additive Manufacturing, 27–30 June, 2016, Raleigh, NC.

Koester, L.W., Taheri, H., Bigelow, T.A., Bond, L.J. and Faierson, E.J., 2018. In-situ acoustic signature monitoring in additive manufacturing processes, in: AIP Conference Proceedings. American Institute of Physics Inc., p. 020006. https://doi.org/10.1063/1.5031503

Krakhmalev, P., Fredriksson, G., Yadroitsava, I., Kazantseva, N., Du Plessis, A. and Yadroitsev, I., 2016. Deformation behavior and microstructure of Ti6Al4V manufactured by SLM. Physics Procedia, 83, pp. 778–788.

Krauss, H. C., Eschey C. and Zaeh, M.F., 2014. Thermography for monitoring the selective laser melting process, Physics Procedia, 56, pp 64–67.

Kruth, J.P., Badrossamay, M., Yasa, E., Deckers, J., Thijs, L. and Van Humbeeck, J., 2010. Part and material properties in selective laser melting of metals. 16th International Symposium on Electromachining (ISEM XVI) edition: 16, Shanghai, China, 19–23 April 2010.

Kruth, J.P., Bartscher, M., Carmignato, S., Schmitt, R., De Chiffre, L. and Weckenmann, A., 2011. Computed tomography for dimensional metrology. CIRP Annals-Manufacturing Technology, 60(2), pp. 821–842.

Kruth, J.P., Froyen, L., Van Vaerenbergh, J., Mercelis, P., Rombouts, M. and Lauwers, B., 2004. Selective laser melting of iron-based powder. Journal of Materials Processing Technology, 149(1), pp. 616–622.

Kuba, M. and Van Aken, D.C. 2013. Analysis of acoustic emission during the melting of embedded indium particles in an aluminum matrix: A study of plastic strain accommodation during phase transformation. Metallurgical and Materials Transactions A 44(8), pp. 3444–3455.

Kuo, C.N., Chua, C.K., Peng, P.C., Chen, Y.W., Sing, S.L., Huang, S. and Su, Y.L., 2020. Microstructure evolution and mechanical property response via 3D printing parameter development of Al–Sc alloy. Virtual Phys. Prototyp. 15, pp. 120–129. https://doi.org/10.1080/17452759.2019.1698967

Kyogoku, H. and Ikeshoji, T.-T., 2020. A review of metal additive manufacturing technologies: Mechanism of defects formation and simulation of melting and solidification phenomena in laser powder bed fusion process. Mech. Eng. Rev. 7, 19-00182-19–00182. https://doi.org/10.1299/mer.19-00182

Leuders, S., Thöne, M., Riemer, A., Niendorf, T., Tröster, T., Richard, H.A. and Maier, H.J., 2013. On the mechanical behaviour of titanium alloy TiAl6V4 manufactured by selective laser melting: Fatigue resistance and crack growth performance. International Journal of Fatigue, 48, pp. 300–307.

Lewandowski, J.J. and Seifi, M., 2016. Metal additive manufacturing: A review of mechanical properties. Annu. Rev. Mater. Res. 46, pp. 151–186. https://doi.org/10.1146/annurev-matsci-070115-032024

Li, L. and Steen, W. M., 1992. Non-contact acoustic emission monitoring during laser processing, ICALEO 1992 Orlando, FL: Laser Institute of America, pp. 719–728.

Lopez E., Brueckner, F., and Gruber S., 2021. Industrial applications, in "Laser powder bed fusion of metals", Elsevier, pp. 583-595. https://doi.org/10.1016/B978-0-12-824090-8.00027-5

Lu, Q.Y. and Wong, C.H., 2017. Applications of non-destructive testing techniques for post-process control of additively manufactured parts. Virtual Phys. Prototyp. 12, pp. 301–321. https://doi.org/10.1080/17452759.2017.1357319

Lu, Q.Y. and Wong, C.H., 2018. Additive manufacturing process monitoring and control by non-destructive testing techniques: challenges and in-process monitoring. Virtual Phys. Prototyp. 13, pp. 39–48. https://doi.org/10.1080/17452759.2017.1351201

Luo, Y., Zhu, L., Han, J., Xie, X., Wan, R. and Zhu, Y., 2019. Study on the acoustic emission effect of plasma plume in pulsed laser welding. Mechanical Systems and Signal Processing, 124, pp. 715–723.

M2M, 2020. Gekko (Online) Available from: https://www.eddyfi.com/en/product/gekko (Accessed on 3 August, 2020).

Manfredi, D., Calignano, F., Krishnan, M., Canali, R., Ambrosio, E.P., Biamino, S., Ugues, D., Pavese, M. and Fino, P., 2014. Additive manufacturing of Al alloys and aluminium matrix composites (AMCs). WA Monteiro (Edr.), Light Metal Alloys Applications, InTech.

Mao, Y.L., Kinsman, G. and Duley, W.W., 1993. Real-time Fast Fourier Transform analysis of acoustic emission during CO2 laser welding of materials. Journal of Laser Applications, 5(2), pp. 17–22.

Martin, A. A., Calta, N. P., Hammons, J. A., Khairallah, S. A., Nielsen, M. H., Shuttlesworth, R. M., Sinclair, N., Matthews, M. J., Jeffries, J. R., Willey, T. M., and Lee, J. R. I., 2019. Ultrafast dynamics of laser-metal interactions in additive manufacturing alloys captured by in situ X-ray imaging. Materials Today Advances, 1, 100002. https://doi.org/10.1016/j.mtadv.2019.01.001

Martin, A. A., Calta, N. P., Khairallah, S. A., Wang, J., Depond, P. J., Fong, A. Y., Thampy, V., Guss, G. M., Kiss, A. M., Stone, K. H., Tassone, C. J., Nelson Weker, J., Toney, M. F., van Buuren, T. and Matthews, M. J., 2019. Dynamics of pore formation during laser powder bed fusion additive manufacturing. Nature Communications, 10(1), pp. 1–10. https://doi.org/10.1038/s41467-019-10009-2

Maskery, I., Leach, R.K. and Thompson, A., 2016. X-ray computed tomography for additive manufacturing: a review. Measurement Science and Technology, 27(7), pp. 72001–72017.

Matthews, M. J., Guss, G., Khairallah, S. A., Rubenchik, A. M., Depond, P. J., and King, W. E., 2016. Denudation of metal powder layers in laser powder bed fusion processes. Acta Materialia. 114, pp. 33–42. https://doi.org/10.1016/j.actamat.2016.05.017

Muravin, B., 2009. Acoustic Emission Science and Technology. Journal of Building and Infrastructure Engineering of the Israeli Association of Engineers and Architects, Tel Aviv, Israel, pp. 1–10.

Nakamura, H., Kawahito, Y., Nishimoto, K. and Katayama, S., 2015. Elucidation of melt flows and spatter formation mechanisms during high power laser welding of pure titanium. Journal of Laser Applications, 27(3), p. 032012.

Nakamura, S., Sakurai, M., Kamimuki, K., Inoue, T. and Ito, Y., 2000. Detection technique for transition between deep penetration mode and shallow penetration mode in CO 2 laser welding of metals. J. Phys. D. Appl. Phys. 33, 2941–2948. https://doi.org/10.1088/0022-3727/33/22/311

National Instruments Corporation 2012, Data Acquisition and Signal Conditioning Course Manual, North Mopac Expressway, Austin, Texas, USA.

NDT Resource Centre 2020, (Online) Available from: https://www.nde-ed.org (Accessed on 3 August, 2020).

Nickels, L., 2016. Additive manufacturing: A user's guide. Metal Powder Report, 71(2), pp. 100–105.

NIST, 2020. Qualification for additive manufacturing materials, processes and parts (Online) Available from: https://www.nist.gov/programs-projects/real-time-monitoring-and-control-additive-manufacturing-processes (Accessed on 3 August, 2020).

NRCratings.com, 2020. Noise reduction coefficients (NRC) for common building materials (Online) Available from: http://www.nrcratings.com/index.html (Accessed on 15 July, 2020).

Okudaira, Y., Ando, H., Satoh, M. and Miyanami, K., 1995. The effect of particle diameter on the acoustic properties of a powder bed. sound absorption characteristic and sound velocity. Journal of the Society of Powder Technology, Japan, 32(5), pp. 311–318. https://doi.org/10.4164/sptj.32.311

Okudaira, Y., Kurihara, Y., Ando, H., Satoh, M. and Miyanami, K., 1993. Sound absorption measurements for evaluating dynamic physical properties of a powder bed. Powder Technology, 77(1) pp. 39–48. https://doi.org/10.1016/0032-5910(93)85005-T

Oliveira, J.P., LaLonde, A.D. and Ma, J., 2020. Processing parameters in laser powder bed fusion metal additive manufacturing. Mater. Des. 193, 108762. https://doi.org/10.1016/j.matdes.2020.108762

Ortega, V.I., López Pumarega, M.I., Nieva, N., Gomez, M.P., Kaplan, A., Docimo, L. Adhesion study in metal-ceramic systems of dental restoration by acoustic emission. Procedia Materials Science, Vol. 9, 2015, pp. 477–483.

Palanco, S. and Laserna, J., 2003. Spectral analysis of the acoustic emission of laser-produced plasmas. Applied Optics. 42 (30), pp. 6078–6084.

PCB Piezotronics (2017) Handbooks-Microphone Handbook (Online) Available from: http://www.pcb.com/Resources/Handbooks (Accessed on 17 February, 2017).

Pieris, D., Stratoudaki, T., Javadi, Y., Lukacs, P., Catchpole-Smith, S., Wilcox, P.D., Clare, A. and Clark, M., 2020. Laser induced phased arrays (LIPA) to detect nested features in additively manufactured components. Mater. Des. 187, 108412. https://doi.org/10.1016/j.matdes.2019.108412

Popovich, A.A., Masaylo, D.V., Sufiiarov, V.S., Borisov, E.V., Polozov, I.A., Bychenok, V.A., Kinzhagulov, I.Y., Berkutov, I.V., Ashikhin, D.S. and Il'inskii, A.V., 2016. A laser ultrasonic technique for studying the properties of products manufactured by additive technologies. Russian Journal of Nondestructive Testing, 52(6), pp. 303–309.

Raj, B., Jayakumar, T. and Thavasimuthu, M., 2007. Practical non-destructive testing. Woodhead Publishing. 3rd ed, Alpha Science, India.

Redding, M.R., Gold, S.A. and Spears, T.G., 2017. US10073060B2 - Non-contact acoustic inspection method for additive manufacturing processes – Google Patents. https://patents.google.com/patent/US20170146489A1/en

Renishaw Plc., 2016, Additive manufacturing apparatus and method, WO2016198885A1.

Repossini, G., Laguzza, V., Grasso, M. and Colosimo, B.M., 2017. On the use of spatter signature for in-situ monitoring of laser powder bed fusion. Additive Manufacturing, 16, pp. 35–48.

Rezanezhad, F., Quinton, W.L., Price, J.S., Elrick, D., Elliot, T.R. and Heck, R.J., 2009. Examining the effect of pore size distribution and shape on flow through unsaturated peat using computer tomography. Hydrology and Earth System Sciences, 13, pp. 1993–2002.

Rieder, H., Dillhöfer, A., Spies, M., Bamberg, J., Hess, T., 2014. Online Monitoring of Additive Manufacturing Processes Using Ultrasound, in: Proceedings of the 11th European Conference on Non-Destructive Testing. pp. 2194–2201.

Rong, Y., 2015. Acoustic emission evaluation and mechanical property characterization of stainless steel specimens manufactured by powder based 3-D printer. MSc dissertation, University of Pittsburgh, 55 p.

Rossing, T.D., Moore, F.R. and Wheeler, P.A., 2001. The Science of Sound. Pearson.

Russell, D.A., 2019 Acoustics and Vibration Animations (online) Available from: https://www.acs.psu.edu/drussell/demos.html (Accessed on 26 July, 2019).

Sakamoto, S., Yamaguchi, K., Ii, K., Takakura, R., Nakamura, Y. and Suzuki, R. (2019). Theoretical and experiment analysis on the sound absorption characteristics of a layer of fine lightweight powder. The Journal of the Acoustical Society of America, 146(4), 2253–2262. https://doi.org/10.1121/1.5126951

Schiefer, M.I. and Sjoeberg, L., 2005. Physical basis of the resonant acoustic method for flaw detection. Advances in powder metallurgy and particulate materials, 3, pp. 87–97.

Schiry, M., Lamberti, C., Böhm, P., Plapper, P., 2016. Acoustic-Emission-Analysis of Dissimilar Laser-welds of Aluminium and Polyamide 6.6. Univers. J. Mater. Sci. 4, 119–124. https://doi.org/10.13189/ujms.2016.040601

Schmidt, M., Merklein, M., Bourell, D., Dimitrov, D., Hausotte, T., Wegener, K., Overmeyer, L., Vollertsen, F. and Levy, G.N., 2017. Laser based additive manufacturing in industry and academia. CIRP Ann. 66, 561–583. https://doi.org/10.1016/j.cirp.2017.05.011

Seifi, M., Gorelik, M., Waller, J., Hrabe, N., Shamsaei, N., Daniewicz, S. and Lewandowski, J.J., 2017. Progress towards metal additive manufacturing standardization to support qualification and certification. JOM 69, pp. 439–455. https://doi.org/10.1007/s11837-017-2265-2

Seifi, M., Salem, A., Beuth, J., Harrysson, O. and Lewandowski, J.J., 2016. Overview of materials qualification needs for metal additive manufacturing. JOM, 68(3), pp. 747–764. https://doi.org/10.1007/s11837-015-1810-0

Sengpielaudio, 2019. Sound intensity and the inverse square law (online) Available from: http://www.sengpielaudio.com/calculator-squarelaw.htm (Accessed on 25 July, 2019).

Shao, J. and Yan, Y. Review of techniques for on-line monitoring and inspection of laser welding. J. Phys.: Conf. Ser. Vol. 15, 2005, pp. 101–107.

Sharratt, B.M., 2015. Non-destructive techniques and technologies for qualification of additive manufactured parts and processes: A literature review. Her Majesty the Queen in Right of Canada, as represented by the Minister of National Defence, 156 p.

Shevchik, S.A., Kenel, C., Leinenbach, C. and Wasmer, K., 2018. Acoustic emission for in situ quality monitoring in additive manufacturing using spectral convolutional neural networks. Addit. Manuf. 21, pp. 598–604. https://doi.org/10.1016/j.addma.2017.11.012

Shi, Z., Jarzynski, J., Bair S. and Jacobs, L.J., 1999. Study of acoustic emission from incipient fatigue failure. in: Review of progress in quantitative nondestructive evaluation. Eds. D. O. Thompson, D. E. Chimenti, 18 A. Springer, Boston, MA, pp. 395–401.

SLM SOLUTIONS, 2020. Additive Quality (Online) Available from: https://www.slm-solutions.com/en/products/software/additivequality/ (Accessed on 18 August, 2020).

Slotwinski, J.A., Garboczi, E.J. and Hebenstreit, K.M., 2014. Porosity measurements and analysis for metal additive manufacturing process control. Journal of Research of the National Institute of Standards and Technology, 119, p. 494. https://doi.org/10.6028/jres.119.019

Smith, R.J., Hirsch, M., Patel, R., Li, W., Clare, A.T. and Sharples, S.D., 2016. Spatially resolved acoustic spectroscopy for selective laser melting. J. Mater. Process. Technol. 236, pp. 93–102. https://doi.org/10.1016/j.jmatprotec.2016.05.005

Spears, T.G. and Gold, S.A., 2016. In-process sensing in selective laser melting (SLM) additive manufacturing. Integr. Mater. Manuf. Innov. 5, pp. 16–40. https://doi.org/10.1186/s40192-016-0045-4

Steen, W. and Mazumder, J., (2010) Laser Material Processing, 4th ed. doi: 10.1007/978-1-84996-062-5

Stepanova, K., Kinzhagulov, I. and Yakovlev Y., 2019. Application of acoustic emission and laser optoacoustics at various stages of defect formation during friction stir welding - IOPscience. J. Phys. Conf. Ser. IOP Publ. 1421.

Strantza, M., Van Hemelrijck, D., Guillaume, P. and Aggelis, D.G., 2017. Acoustic emission monitoring of crack propagation in additively manufactured and conventional titanium components. Mech. Res. Commun. 84, pp. 8–13. https://doi.org/10.1016/j.mechrescom.2017.05.009

Stultz, G.R., Bono, R.W. and Schiefer, M.I., 2005. Fundamentals of resonant acoustic method NDT. Advances in Powder Metallurgy and Particulate Materials, 3, p. 11.

Sü, Z. and Çalışkan, M., 2007. Acoustical design and noise control in metro stations: Case studies of the Ankara Metro System. Build. Acoust. 14, pp. 203–221. https://doi.org/10.1260/135101007781998910

Taheri Andani, M., Dehghani, R., Karamooz-Ravari, M.R., Mirzaeifar, R. and Ni, J., 2018. A study on the effect of energy input on spatter particles creation during selective laser melting process. Addit. Manuf. 20, pp. 33–43. https://doi.org/10.1016/j.addma.2017.12.009

Taheri, H., Koester, L.W., Bigelow, T.A., Faierson, E.J. and Bond, L.J., 2019. In situ additive manufacturing process monitoring with an acoustic technique: Clustering performance evaluation using K-means algorithm. J. Manuf. Sci. Eng. Trans. ASME 141. https://doi.org/10.1115/1.4042786

Tapia, G. and Elwany, A., 2014. A review on process monitoring and control in metal-based additive manufacturing. J. Manuf. Sci. Eng. Trans. 136. https://doi.org/10.1115/1.4028540

Taylor, B. and Weidmann, E. Application notes–metallographic preparation of titanium, Struers, Ballerup, Denmark, pp. 1–6.

The Modal Shop, Inc, 2020. Resonant acoustic method, (Online) Available from: http://www.modalshop.com/ndt/Resonant-Acoustic-Method?ID=73 (Accessed on 21 July, 2020).

Townsend, A., Blunt, L. and Bills, P.J., 2016. Investigating the capability of microfocus X-ray computed tomography for areal surface analysis of additively manufactured parts. In: American Society for Precision Engineering Summer Topical Meeting: Dimensional Accuracy and Surface Finish in Additive Manufacturing, 27th–30th June 2016, Raleigh, NC, USA.

Tran, H.C. and Lo, Y.L., 2019. Systematic approach for determining optimal processing parameters to produce parts with high density in selective laser melting process. Int. J. Adv. Manuf. Technol. 105, pp. 4443–4460. https://doi.org/10.1007/s00170-019-04517-0

Trapp, J., Rubenchik, A.M., Guss, G. and Matthews, M.J., 2017. In situ absorptivity measurements of metallic powders during laser powder-bed fusion additive manufacturing. Applied Materials Today, 9, pp. 341–349. https://doi.org/10.1016/J.APMT.2017.08.006

Van der Schueren, B. and Kruth, J.P., (1995) Powder deposition in selective metal powder sintering, Rapid Prototyping Journal, Vol. 1 Issue: 3, pp. 23–31, https://doi.org/10.1108/13552549510094241

Van Zyl, I., Yadroitsava, I. and Yadroitsev, I., 2016. Residual stress in Ti6Al4V objects produced by Direct Metal Laser Sintering. South African Journal of Industrial Engineering, 27(4), pp. 134–141.

Vrancken, B., Buls, S., Kruth, J.P. and Van Humbeeck, J., 2015. Influence of preheating and oxygen content on Selective Laser Melting of Ti6Al4V. 16th RAPDASA Conference, Pretoria, South Africa, 4–6 November 2015.

Vrancken, B., Thijs, L., Kruth, J.P. and Van Humbeeck, J., 2012. Heat treatment of Ti6Al4V produced by Selective Laser Melting: Microstructure and mechanical properties. J. Alloys Compd. 541, pp. 177–185. https://doi.org/10.1016/j.jallcom.2012.07.022

Waller, J., Parker, B., Hodges, K., Walker, J., Wells, D., Burke, E., Generazio, E., Todorov, E., Price, A., James, S. and Dutton, B., 2015. Qualification of products fabricated via additive manufacturing using nondestructive evaluation. Trilateral Safety & Mission Assurance Conference (TRISMAC 2015) Virtual Meeting ESA-ESRIN; 21–22 May 2015, Frascati, Italy.

Wang, D., Wu, S., Fu, F., Mai, S., Yang, Y., Liu, Y. and Song, C., 2017. Mechanisms and characteristics of spatter generation in SLM processing and its effect on the properties. Mater. Des. 117, pp. 121–130. https://doi.org/10.1016/j.matdes.2016.12.060

Wasmer, K., Kenel, C., Leinenbach, C. and Shevchik, S.A., 2018. In situ and real-time monitoring of powder-bed AM by combining acoustic emission and artificial intelligence, in: industrializing additive manufacturing - Proceedings of Additive Manufacturing in Products and Applications - AMPA2017. Springer International Publishing, pp. 200–209. https://doi.org/10.1007/978-3-319-66866-6_20

Wasmer, K., Le-Quang, T., Meylan, B. and Shevchik, S.A., 2019. In situ quality monitoring in AM using acoustic emission: A reinforcement learning approach. J. Mater. Eng. Perform. 28, pp. 666–672. https://doi.org/10.1007/s11665-018-3690-2

Whiting, J., Springer, A. and Sciammarella, F., 2018. Real-time acoustic emission monitoring of powder mass flow rate for directed energy deposition. Additive Manufacturing, 23, pp. 312–318. https://doi.org/10.1016/j.addma.2018.08.015

Williams, J., Dryburgh, P., Clare, A., Rao, P. and Samal, A., 2018. Defect detection and monitoring in metal additive manufactured parts through deep learning of spatially resolved acoustic spectroscopy Signals. Smart Sustain. Manuf. Syst. 2, 20180035. https://doi.org/10.1520/ssms20180035

Wohlers, T. and Caffrey, T., 2014. Wohlers Report 2014: 3D printing and additive manufacturing state of the industry. Annual Worldwide Progress Report, Fort Collins, Wohlers Associates.

Wohlers, T. Wohlers Report 2015: 3D Printing and additive manufacturing state of the industry. Annual Worldwide Progress Report, Fort Collins, Wohlers Associates.

Wohlers, T. Wohlers Report 2019: 3D Printing and additive manufacturing state of the industry. Annual Worldwide Progress Report, Fort Collins, Wohlers Associates.

Wu, H., Wang, Y. and Yu, Z., 2016. In situ monitoring of FDM machine condition via acoustic emission. The International Journal of Advanced Manufacturing Technology, 84(5–8), pp.1483–1495.

Wu, H., Yu, Z. and Wang, Y., 2019. Experimental study of the process failure diagnosis in additive manufacturing based on acoustic emission. Meas. J. Int. Meas. Confed. 136, pp. 445–453. https://doi.org/10.1016/j.measurement.2018.12.067

Wu, J., Zhao, J., Qiao, H., Sun, B. and Lu, Y., 2020. A new acoustic emission on-line monitoring method of laser shock peening. Optik (Stuttg). 205, 163578. https://doi.org/10.1016/j.ijleo.2019.163578

Yadav, P., Rigo, O., Arvieu, C., Le Guen, E. and Lacoste, E., 2020. In situ monitoring systems of the SLM process: On the need to develop machine learning models for data processing. Crystals 10, 524. https://doi.org/10.3390/cryst10060524

Yadroitsava, I. and Yadroitsev, I., 2015. Residual stress in metal specimens produced by Direct Metal Laser Sintering. International Solid Freeform Fabrication Symposium, August 10–12, 2015, University of Texas at Austin, USA.

Yadroitsava, I., Els, J., Booysen, G. and Yadroitsev, I., 2015a. Peculiarities of single track formation from TI6AL4V alloy at different laser power densities by selective laser melting. South African Journal of Industrial Engineering, 26(3), pp. 86–95. https://doi.org/10.7166/26-3-1185

Yadroitsev, I., 2009. Selective laser melting : direct manufacturing of 3D-objects by selective laser melting of metal powders (Book, 2009) [WorldCat.org]. LAP Lambert Academic Publ., Saarbrücken.

Yadroitsev, I. and Yadroitsava, I., 2015. Evaluation of residual stress in stainless steel 316L and Ti6Al4V samples produced by selective laser melting. Virtual and Physical Prototyping, 10(2), pp. 67–76.

Yadroitsev, I. and Yadroitsava, I., 2021. A step-by-step guide to the L-PBF process. Additive Manufacturing Materials and Technologies, pp. 39-77. https://doi.org/10.1016/B978-0-12-824090-8.00026-3

Yadroitsev, I., 2009. Selective laser melting: Direct manufacturing of 3D-objects by selective laser melting of metal powders. LAP Lambert Publishing, 307 p.

Yadroitsev, I., Gusarov, A., Yadroitsava, I. and Smurov, I., 2010. Single track formation in selective laser melting of metal powders. Journal of Materials Processing Technology, 210(12), pp. 1624–1631.

Yadroitsev, I., Krakhmalev, P. and Yadroitsava, I., 2015. Hierarchical design principles of selective laser melting for high quality metallic objects. Additive Manufacturing, 7, pp. 45–56.

Yadroitsev, I., Krakhmalev, P., Yadroitsava, I. and Du Plessis, A., 2018. Qualification of Ti6Al4V ELI alloy produced by laser powder bed fusion for biomedical applications. JOM 70, pp. 372–377. https://doi.org/10.1007/s11837-017-2655-5

Yadroitsev, I. and Smurov, I., 2011. Surface morphology in selective laser melting of metal powders, in: Physics Procedia. Elsevier, pp. 264–270. https://doi.org/10.1016/j.phpro.2011.03.034

Ye, D., Hong, G.S., Zhang, Y., Zhu, K. and Fuh, J.Y.H., 2018. Defect detection in selective laser melting technology by acoustic signals with deep belief networks. Int. J. Adv. Manuf. Technol. 96, pp. 2791–2801. https://doi.org/10.1007/s00170-018-1728-0

Ye, D., Zhang, Y., Zhu, K., Hong, G.-S. and Ying, J., 2017. Characterization of acoustic signals during a direct metal laser sintering process. In: Zhou, S., Patty, A., Chen, S. (Eds.), International Conference on Energy Equipment Science and Engineering II, (ICEESE 2016). CRC Press, Guangzhou, China, pp. 1315–1320. https://doi.org/10.1201/9781315116174

Ye, D., Zhu, K., Fuh, J.Y.H., Zhang, Y. and Soon, H.G., 2019. The investigation of plume and spatter signatures on melted states in selective laser melting. Optics & Laser Technology, 111, pp. 395–406.

Yusof, M.F.M., Ishak, M. and Ghazali, M.F., 2017. Feasibility of using acoustic method in monitoring the penetration status during the pulse mode laser welding process. IOP Conf. Ser. Mater. Sci. Eng. 238, 012006. https://doi.org/10.1088/1757-899X/238/1/012006

Yusuf, S., Chen, Y., Boardman, R., Yang, S., and Gao, N., 2017. Investigation on porosity and microhardness of 316l stainless steel fabricated by selective laser melting. Metals, 7(2), 64. https://doi.org/10.3390/met7020064

Zhang, S., Lane, B., Whiting, J. and Chou, K., 2019. On thermal properties of metallic powder in laser powder bed fusion additive manufacturing. J. Manuf. Process. 47, pp. 382–392. https://doi.org/10.1016/J.JMAPRO.2019.09.012

Zhang, Y.,. Fuh, J.Y.H., Ye, D. and Hong., G.S., 2019a. In-situ monitoring of laser-based PBF via off-axis vision and image processing approaches. Addit. Manuf., 25, pp. 263–274. https://doi.org/10.1016/j.addma.2018.10.020

Zhao, C., Fezzaa, K., Cunningham, R.W., Wen, H., De Carlo, F., Chen, L., Rollett, A. D. and Sun, T., 2017. Real-time monitoring of laser powder bed fusion process using high-speed X-ray imaging and diffraction. Scientific Reports, 7(1), pp. 1–11. https://doi.org/10.1038/s41598-017-03761-2

Zhao, C.X., Kwakernaak, C., Pan, Y., Richardson, I.M., Saldi, Z., Kenjeres, S. and Kleijn, C.R., 2010. The effect of oxygen on transitional Marangoni flow in laser spot welding. Acta Materialia, 58(19), pp. 6345–6357.

Zheng, H., Li, H., Lang, L., Gong, S. and Ge, Y., 2018. Effects of scan speed on vapor plume behavior and spatter generation in laser powder bed fusion additive manufacturing. Journal of Manufacturing Processes. 36, pp. 60–67. https://doi.org/10.1016/j.jmapro.2018.09.011

Zhou, Y. H., Zhang, Z. H., Wang, Y. P., Liu, G., Zhou, S. Y., Li, Y. L., Shen, J. and Yan, M., 2019. Selective laser melting of typical metallic materials: An effective process prediction model developed by energy absorption and consumption analysis. Additive Manufacturing, 25, pp. 204–217. https://doi.org/10.1016/j.addma.2018.10.046

Ziółkowski, G., Chlebus, E., Szymczyk, P. and Kurzac, J., 2014. Application of X-ray CT method for discontinuity and porosity detection in 316L stainless steel parts produced with SLM technology. Archives of Civil and Mechanical Engineering, 14(4), pp. 608–614. https://doi.org/10.1016/j.acme.2014.02.003

Appendix

~ *Calibration Report* ~

Model: 378B02 Serial Number: 132756
Microphone Model: 377B02 Serial Number: 179115 Description: 1/2" Free-Field Microphone
Preamplifier Model: 426E01 Serial Number: 051802 and Preamplifier

Calibration Data

System Sensitivity @ 251.2 Hz: 48.28 mV/Pa Polarization Voltage, External: 0 V
-26.32 dB re 1V/Pa

Temperature: 69 °F (21°C) Ambient Pressure: 981 mbar Relative Humidity: 36 %

Frequency Response (0 dB @ 251.2 Hz)

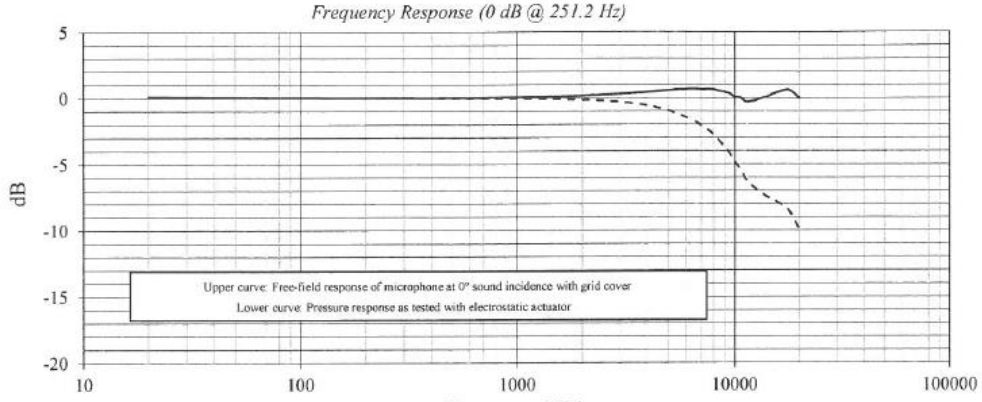

Freq (Hz)	Lower (dB)	Upper (dB)	Freq (Hz)	Lower (dB)	Upper (dB)	Freq (Hz)	Lower (dB)	Upper (dB)	Freq (Hz)	Lower (dB)	Upper (dB)
20.0	0.11	0.11	1679	-0.11	0.12	7499	-2.41	0.66	-	-	-
25.1	0.10	0.10	1778	-0.12	0.14	7943	-2.74	0.65	-	-	-
31.6	0.08	0.08	1884	-0.13	0.16	8414	-3.18	0.55	-	-	-
39.8	0.06	0.06	1995	-0.13	0.18	8913	-3.64	0.47	-	-	-
50.1	0.06	0.06	2114	-0.14	0.20	9441	-4.17	0.35	-	-	-
63.1	0.04	0.04	2239	-0.15	0.22	10000	-4.86	0.09	-	-	-
79.4	0.04	0.04	2371	-0.19	0.22	10593	-5.36	0.05	-	-	-
100.0	0.03	0.03	2512	-0.21	0.25	11220	-6.13	-0.27	-	-	-
125.9	0.02	0.02	2661	-0.26	0.25	11885	-6.57	-0.25	-	-	-
158.5	0.01	0.01	2818	-0.27	0.29	12589	-6.92	-0.15	-	-	-
199.5	0.01	0.01	2985	-0.30	0.32	13335	-7.20	-0.01	-	-	-
251.2	0.00	0.00	3162	-0.35	0.33	14125	-7.48	0.11	-	-	-
316.2	-0.01	0.00	3350	-0.38	0.36	14962	-7.67	0.30	-	-	-
398.1	-0.01	-0.01	3548	-0.44	0.39	15849	-7.90	0.45	-	-	-
501.2	-0.02	0.02	3758	-0.50	0.40	16788	-8.15	0.57	-	-	-
631.0	-0.03	0.01	3981	-0.56	0.44	17783	-8.49	0.62	-	-	-
794.3	-0.04	0.05	4217	-0.65	0.47	18837	-9.14	0.37	-	-	-
1000.0	-0.05	0.07	4467	-0.73	0.50	19953	-9.94	-0.01	-	-	-
1059.3	-0.06	0.07	4732	-0.83	0.54	-	-	-	-	-	-
1122.0	-0.06	0.08	5012	-0.95	0.58	-	-	-	-	-	-
1188.5	-0.07	0.08	5309	-1.10	0.60	-	-	-	-	-	-
1258.9	-0.07	0.09	5623	-1.25	0.64	-	-	-	-	-	-
1333.5	-0.08	0.10	5957	-1.43	0.64	-	-	-	-	-	-
1412.5	-0.08	0.11	6310	-1.61	0.69	-	-	-	-	-	-
1496.2	-0.09	0.11	6683	-1.85	0.67	-	-	-	-	-	-
1584.9	-0.10	0.12	7080	-2.14	0.65	-	-	-	-	-	-

Technician: Mike N. O'connor Date: November 15, 2017

ilac-MRA ACCREDITED
CALIBRATION CERT #1002.01

PCB PIEZOTRONICS VIBRATION DIVISION
3425 Walden Avenue, Depew, New York, 14043
TEL: 888-684-0013 FAX: 716-685-3886 www.pcb.com

Page 2 of 2

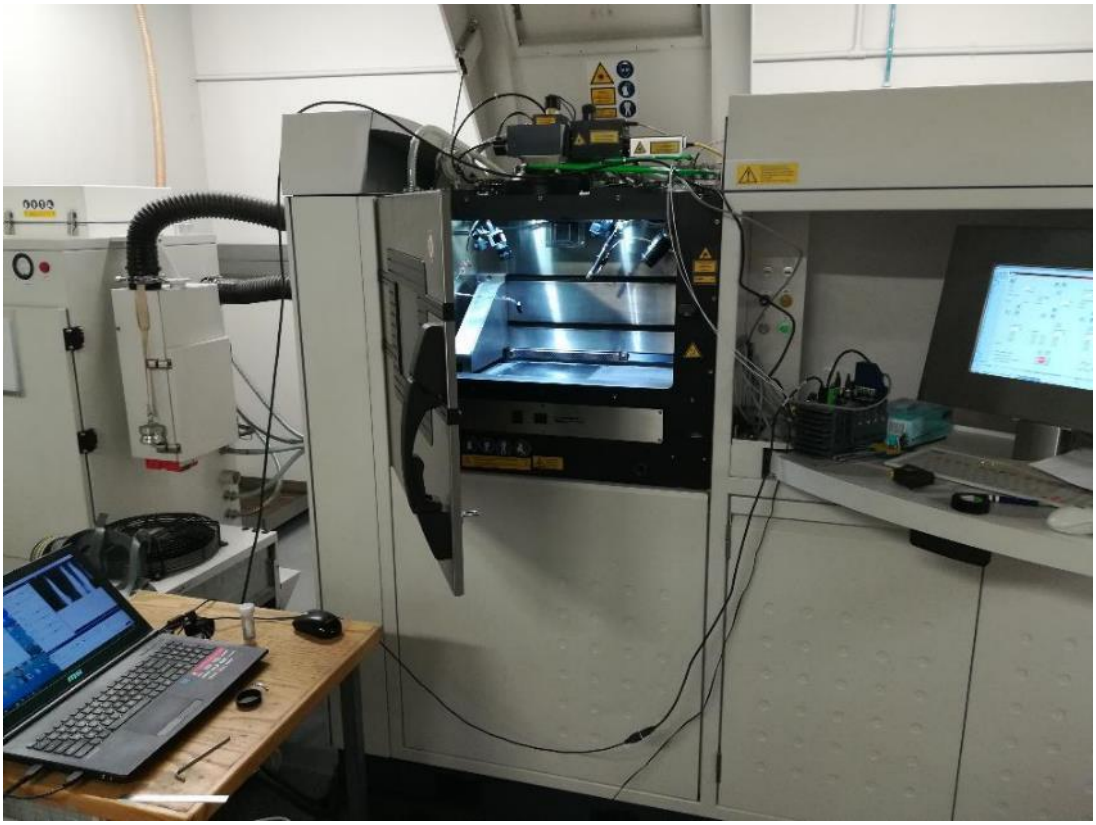

Figure 76: Photo of M280 while setting up for an experiment

Table 16: Summary of key process parameters in LPBF (Adapted from Spears and Gold, 2016)

Laser and scanning parameters		
1. Average power	Measure of total energy output of a laser	Controlled
2. Mode	Continuous wave or pulsed	Predefined
3. Peak power	Maximum power in a laser pulse	Predefined
4. Pulse width	Length of a laser pulse when operating in pulsed mode	Predefined
5. Frequency	Pulses per unit time	Predefined
6. Wavelength	Distance between crests in laser electromagnetic waves	Predefined
7. Polarization	Orientation of electromagnetic waves in laser beam	Predefined
8. Beam quality	Related to intensity profile and used to predict how well beam can be focused and determine minimum theoretical spot size (equal to 1 for a Gaussian) (Steen and Mazumder, 2010)	Predefined
9. Intensity profile	Determines how much energy added at a specific location	Predefined
10. Spot size	Length and width of elliptical spot (equal for circular spots)	Controlled
11. Scan velocity	Velocity at which laser moves across build surface	Controlled
12. Hatch distance	Distance between neighbouring laser passes	Controlled
13.[a] Scan strategy	Pattern in which the laser is scanned across the build surface (hatches, zig-	Controlled

	zags, spirals, etc.) and associated parameters	
Powder material properties		
14. Bulk density	Material density, limits maximum density of final component	Predefined
15. Thermal conductivity	Measure of material's ability to conduct heat	Predefined
16. Heat capacity	Measure of energy required to raise the temperature of the material	Predefined
17. Latent heat of fusion	Energy required for solid-liquid and liquid-solid phase change	Predefined
18. Melting temperature	Temperature at which material melts; for alloys the difference between the liquidus and solidus temperature is typically of greater interest	Predefined
19. Boiling temperature	Temperature at which material vaporizes; may only be important in certain process conditions	Predefined
20. Melt pool viscosity	Measure of resistance of melt to flow	Predefined
21. Coefficient of thermal expansion	Measure of volume change of material on heating or cooling	Predefined
22. Surface free energy	Free energy required to form new unit area of solid-liquid interfacial surface	Predefined
23. Vapour pressure	Measure of the tendency of material to vaporize	Predefined

24. Heat (enthalpy) of reaction	Energy associated with a chemical reaction of the material (e.g. oxide formation), not always relevant	Predefined
25. Material absorptivity	Measure of laser energy absorbed by the material, as opposed to that which is transmitted or reflected	Predefined
26. Diffusivity	Important for solid state sintering, not as critical for melting	Predefined
27. Solubility	Solubility of solid material in liquid melt, unlikely to be significant	Predefined
28.[a] Particle morphology	Measures of shape of individual particles and their distributions, e.g. aspect ratio, circularity, and elongation	Predefined
29. Surface roughness	Arithmetic mean of the surface profile	Predefined
30. Particle size distribution	Distribution of particle sizes, usually diameter, is a powder sample	Predefined
31.[a]Pollution	Ill-defined factor describing change in properties of powder due to reuse as dust and other particles added to powder	Predefined
Powder bed properties and recoat parameters		
32. Density	Measure of packing density of powder particles, influences heat balance	Predefined
33. Thermal conductivity	Measure of powder bed's ability to conduct heat	Predefined
34. Heat capacity	Measure of energy required to raise the temperature of the powder bed	Predefined

35. Absorptivity	Measure of laser energy absorbed, dependent on material absorptivity and state of powder bed	Predefined
36. Emissivity	Ratio of energy radiated to that of black body	Predefined
37.[a] Deposition system parameters	Recoater velocity, pressure, recoater type, dosing (Van der Schueren and Kruth, 1995)	Controlled
38. Layer thickness	Height of a single powder layer, limiting resolution and impacting process speed	Controlled
39. Powder bed temperature	Bulk temperature of the powder bed	Controlled
Build environment parameters		
40. Shield Gas	Usually Ar or N2, but may also be He, or something else	Predefined
41. Oxygen level	Probably most important environmental parameter; oxygen can lead to oxide formation in metal, changes wettability, energy required for welding	Controlled
42. Shield gas molecular weight	Influences heat balance, diffusivity into and out of part	Predefined
43. Shield gas viscosity	May influence free surface activity of melt pool, convective heat balance	Predefined
44. Thermal conductivity	Term in heat balance	Predefined

45. Heat capacity of gas	Term in heat balance	Predefined
46. Pressure	Influences vaporization of metal as well as oxygen content	Controlled
47. Gas flow velocity	Influences convective cooling, removal of condensate	Controlled
48. Convective heat transfer coefficient	Convective cooling of just-melted part by gas flowing over the surface	Predefined
49. Ambient temperature	Appears in heat balance, may impact powder preheat and residual stress	Controlled
50. Surface free energy	Between liquid and surrounding gas, influences melt pool shape	Predefined